processes

Review

Advances and Challenges in WO_3 Nanostructures' Synthesis

Odeilson Morais Pinto [1], Rosimara Passos Toledo [1], Herick Ematne da Silva Barros [1], Rosana Alves Gonçalves [2,*], Ronaldo Spezia Nunes [1,3] Nirav Joshi [4,5] and Olivia Maria Berengue [1]

[1] Department of Physics, School of Engineering, São Paulo State University (UNESP), Guaratinguetá 12516-410, SP, Brazil; ronaldo.spezia@unesp.br (R.S.N.); olivia.berengue@unesp.br (O.M.B.)
[2] Instituto Federal do Norte de Minas Gerais (IFNMG), Januária 39480-000, MG, Brazil
[3] Department of Chemistry and Energy, School of Engineering and Science, São Paulo State University (UNESP), Guaratinguetá 12516-410, SP, Brazil
[4] São Carlos Institute of Physics, University of São Paulo, P.O. Box 369, São Carlos 13560-970, SP, Brazil
[5] Luxembourg Institute of Science and Technology (LIST), 4362 Esch-sur-Alzette, Luxembourg
* Correspondence: rosana.goncalves@ifnmg.edu.br

Abstract: In recent decades, nanoscience has experienced rapid global advancements due to its focus on materials and compounds at the nanoscale with high efficiency across diverse applications. WO_3 nanostructures have proven to be a unique material in the development of new technologies due to their electrical, optical, and catalytic properties. They have been used as raw materials for the fabrication of electrochromic devices, optoelectronic devices, hydrogenation catalysts, gas sensors, adsorbents, lithium-ion batteries, solar driven-catalysts, and phototherapy. One of the most striking characteristics of WO_3 is its morphological diversity, spanning from 0D to 2D, encompassing nanoparticles, nanowires, nanofibers, nanorods, nanosheets, and nanoplates. This review discusses common synthesis methods for WO_3 nanostructures, including hydrothermal and solvothermal methods, microwave-assisted synthesis, sol-gel, electrospinning, co-precipitation, and solution combustion, with emphasis on the advantages and challenges of each of them. The processes involved, the obtained morphologies, and the resulting applications are also presented. As evidenced here, the fine control of the synthesis parameters allows the production of nanostructures with controlled phase, morphology, and size, essential aspects for the production of high-performance WO_3-based devices.

Keywords: tungsten oxide; synthesis methods; morphology; tailored applications

Citation: Pinto, O.M.; Toledo, R.P.; Barros, H.E.d.S.; Gonçalves, R.A.; Nunes, R.S.; Joshi, N.; Berengue, O.M. Advances and Challenges in WO_3 Nanostructures' Synthesis. *Processes* **2024**, *12*, 2605. https://doi.org/10.3390/pr12112605

Received: 17 September 2024
Revised: 12 October 2024
Accepted: 31 October 2024
Published: 20 November 2024

1. Introduction

In the past few decades, there has been a remarkable and rapid global advancement in the field of nanoscience. This domain has attracted multiple disciplines due to its primary focus on seeking materials or compounds at the nanoscale capable of demonstrating high efficiency across various applications. In other words, nanotechnology aims to apply scientific discoveries to create products that benefit society and the environment [1], transforming these breakthroughs into new electronic, pharmaceutical, and cosmetic products, while also offering the potential to design products that mitigate or even eliminate environmental impacts caused by human activity.

Tungsten, as a transition metal element with atomic number 74 and electronic configuration [Xe] $4f^{14}$ $5d^4$ $6s^2$, exhibits oxidation states ranging from −2 to +6 in its compounds, with +6 being the most common. The interaction between tungsten and oxygen is highly intricate, resulting in stable binary oxides, tungstates, acids, and a diverse array of non-stoichiometric compounds [2,3]. Among these compounds, WO_3 stands out, possessing a structure composed of perovskite-like units, specifically of the ReO_3 type [4]. Generally, seven distinct structural types exist: cubic (c-WO_3) [4,5], monoclinic I (γ-WO_3) [4,6], orthorhombic (β-WO_3) [7,8], tetragonal (α-WO_3) [4,8], triclinic (δ-WO_3) [4,9], monoclinic II (ε-WO_3) [10,11], and hexagonal (h-WO_3) [8,9]—which can be obtained through temperature

control. Concerning non-stoichiometric compounds, tungsten oxide can exhibit variable stoichiometry between WO_2 and WO_3, represented as WO_x, where x is less than 3 (e.g., $WO_{2.98}$, $WO_{2.96}$, $WO_{2.9}$, $WO_{2.83}$, and $WO_{2.72}$) [12,13].

The favorable electrical, optical, and magnetic properties of semiconductor oxides have gained increased research attention. Among these oxides, WO_3 and its nanostructures have substantial potential for countless applications, including adsorption [14,15], electrochromic devices [16,17], substrates for Raman scattering [18,19], solar-driven catalysts [20,21], phototherapy [22,23], gas sensors [24,25], hydrogenation catalysts [26,27], and lithium-ion batteries [6,28].

Numerous synthesis methods for tungsten oxides exist, ranging from well-established to less conventional approaches. These methods encompass both physical and chemical procedures. Examples of physical methods include ball milling, sputtering, laser ablation, and electron beam evaporation. Chemical methods include sol-gel, polyol method, hydrothermal method, co-precipitation method, microemulsion technique, solution combustion synthesis, and chemical vapor deposition [29].

Among the various synthesis methods for obtaining WO_3, we herein present and critically analyze some of the most widely used methods for obtaining WO_3 nanostructures, focusing on hydrothermal and solvothermal, microwave-assisted, co-precipitation, solution combustion, sol-gel, and electrospinning methods. These methods offer advantages such as simplicity, convenience, low cost, uniform material composition, and high purity. The distinct methods and fine control over experimental parameters allow for the generation of diverse morphologies, including nanorods, nanoplates, nanosheets, hierarchical structures, nanowires, nanotubes, nanoflowers, and hollow microspheres with differentiated physical–chemical properties which make them suitable for a variety of technological applications.

2. Methods

2.1. Co-Precipitation Method

Co-precipitation is one of the most popular and efficient methods to produce metal oxides because of its simplicity, homogeneity on the atomic scale, easy control of the size and composition of NPs, and the possibility of scalability. In addition, the use of aqueous solutions instead of organic solvents and the low reaction temperatures reduce energy consumption and make this synthesis more environmentally friendly [30,31].

This synthesis route involves the precipitation of metallic cations in the form of hydroxides, carbonates, oxalates, or citrates from chemical reactions between precursor salts and precipitation agents (acid or base) in a solvent. Drying and calcination processes are necessary to obtain the target material. During the co-precipitation process, nucleation, growth, coarsening, and/or agglomeration processes occur simultaneously. Nucleation is the most important step in the process as it marks the beginning of particle formation; their size is inversely proportional to the nucleation rate. Secondary processes such as Ostwald ripening and aggregation control the size, morphology, and properties of the nanostructures [32–34].

The control of parameters such as the temperature, pH, concentration of precursors and their counter ions in solution, stirring rate, mixing method, rate of reactant feed, and use of additives is fundamental for obtaining nanostructures with controlled morphology and phase. Failure to adjust these parameters can compromise the reproducibility of the synthesis, the purity, and the size of the NPs. However, it is precisely because of this variety of co-precipitation chemistry and reaction conditions that this technique can produce different materials (metals, oxides, metal chalcogenides, etc.) with very distinct morphologies [35–37].

Such factors have been increasing the interest in the use of this method for the synthesis of WO_3 nanostructures. This is because the physicochemical properties of this oxide are very sensitive to the morphology, size, and concentration of dopants in its structure, and the co-precipitation method offers good control of these parameters, being used successfully to produce diverse WO_3 nanostructures with tailored properties [38,39]. Figure 1

presents examples of some of the various morphologies that can be obtained for WO_3 from the co-precipitation method: nanoplates [40] (Figure 1a), nanoflowers [41] (Figure 1b), nanosheets [42] (Figure 1c), polyhedral NPs [43] (Figure 1d), quasi-spherical NPs [44] (Figure 1e), and nanorods [45] (Figure 1f), demonstrating the versatility of this technique.

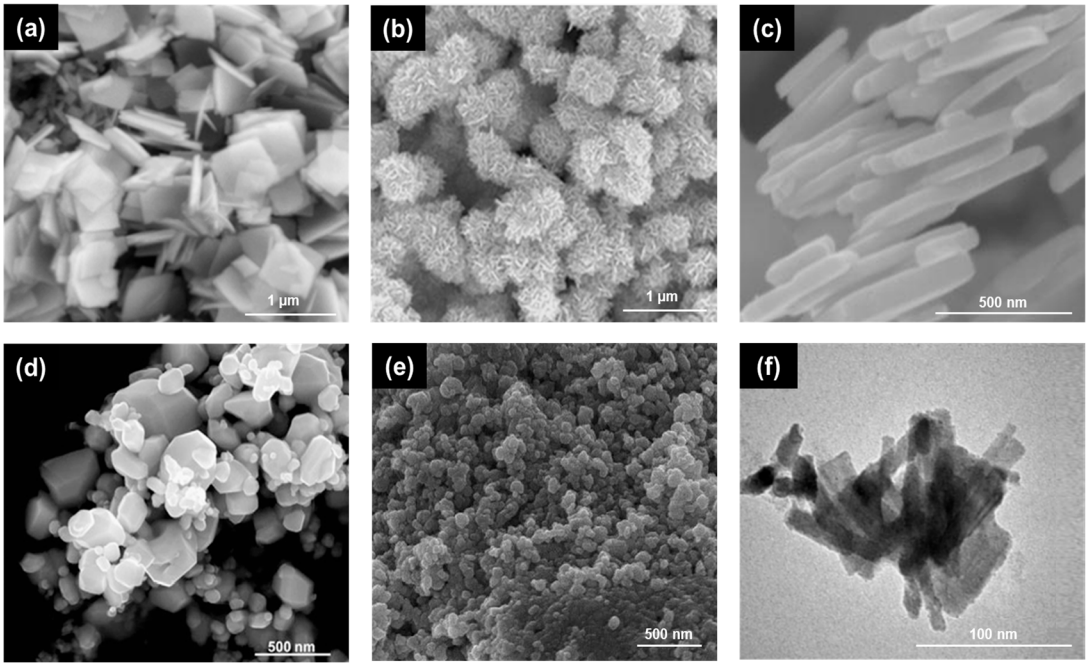

Figure 1. WO_3 structures with (**a**) nanoplates [40], (**b**) nanoflowers [41], (**c**) nanosheets [42], (**d**) polyhedral NPs [43], (**e**) quasi-spherical NPs [44], and (**f**) nanorods [45] morphology obtained from the co-precipitation method. Figure adapted with permission from References [40–45]. Copyright Elsevier.

2.1.1. Nanoparticles

WO_3 NPs of small size, high homogeneity, and stoichiometric composition with good performance as catalysts for chemical reactions and photocatalysts in the wastewater decolorization process have been produced by the co-precipitation method. Wasmi et al. [46], for example, showed that quasi-spherical NPs of monoclinic WO_3 synthesized using ammonium paratungstate hydrate as a precursor and HCl as a precipitating agent act as catalysts in the presence of ethanol for the synthesis of malonic acid ester via high-pressure ozonolysis with a good yield in a short time and with recyclability. Adhikari et al. [47] showed that monoclinic WO_3 quasi-spherical NPs with a size of ~55 nm and high crystalline quality (Figure 2a,b) synthesized by the co-precipitation method using solid tungstic acid and hydrogen peroxide are excellent nanoadsorbents for the methylene blue (MB) dye. In addition to the good physical properties, the NPs were found to have opposite surface charges to the MB dye, which promotes a strong electrostatic attraction between them (Figure 2c) and increases the process efficiency with a maximum adsorption of 99.7% being achieved for an adsorbent dose of 1 g/L in 90 min. Other authors have also been successful in the photodegradation of MB dye using monoclinic WO_3 NPs synthesized from APH and HNO_3 [48], sodium tungstate hydrate (STH) and HNO_3 [49], and STH and NaCl [50], STH, HCl, and NaCl [51] as reagents and in the photodegradation of the Congo red dye by spherical NPs of orthorhombic WO_3 [52] and the dye rhodamine B (RhB) by monoclinic WO_3 NPs [53].

The high surface area and good physicochemical properties of the WO_3 NPs produced by this method have also been shown to be beneficial for chemical and gas sensing. A high photocatalytic activity for the oxidation reaction of nitric oxide under UV irradiation, with an efficiency of up to 80% (at 10% relative humidity), was observed for monoclinic WO_3 polyhedral NPs produced using PEG as a template and steric stabilizer (Figure 1d) [43].

Ammonia gas sensing with orthorhombic WO_3 NPs [54], photocatalytic reduction of CO_2 under visible light irradiation [55], the degradation of the antibiotic gentamicin under ultraviolet irradiation [44], and the degradation of n-pentane under visible light irradiation [56] using monoclinic WO_3 NPs have also been reported.

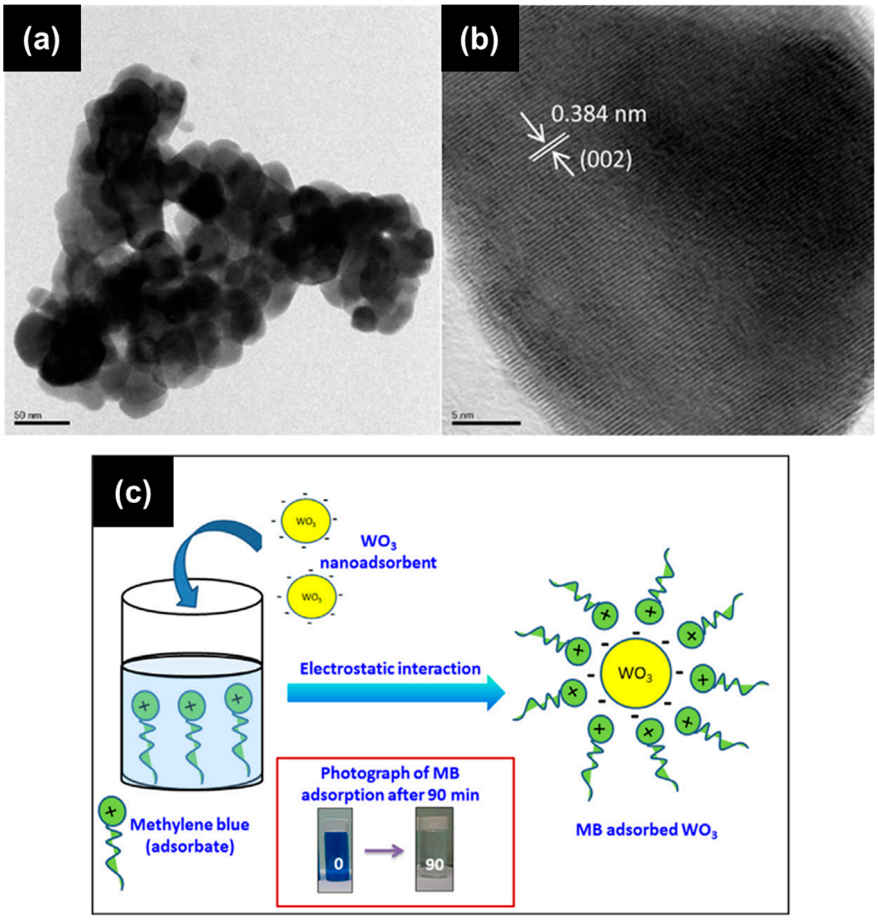

Figure 2. (**a**) TEM, (**b**) HRTEM, and (**c**) adsorption scheme for MB adsorption of the WO_3 nanoadsorbent. Figure adapted with permission from Reference [47]. Copyright 2017 Elsevier.

2.1.2. Nanorods

Thus far, the synthesis of 1D tungsten oxide nanostructures by the co-precipitation method has been little explored; however, the nanostructures obtained in this way have shown to be very promising for applications in some areas. Recently, Banic et al. [45] showed that hexagonal WO_3 nanorods produced through this technique present a good response for the degradation of the pesticide thiacloprid. The nanostructures were obtained by adding HCl to a sodium tungstate solution under agitation and adjusting its pH to 1.4. After keeping the solution at 60 °C for 48 h, the material was filtered, rinsed several times with distilled water, and dried for 48 h to obtain the final product. WO_3 nanorods achieved ~50% and ~75% removal efficiency of the pesticide thiacloprid under simulated sunlight and ultraviolet light irradiation, respectively. The photodegradation of the pesticide was shown to be improved with the formation of WO_3/Fe_3O_4 heterojunctions, reaching a maximum efficiency of 91.3% for a 0.4% content of WO_3 in the composite.

Kabcun et al. [57] synthesized monoclinic WO_3 nanorods from the same method using an aqueous solution of STH, citric acid, and ethylene glycol heated to 70 °C and HCl as a precipitating agent. The precipitate was collected by centrifugation, rinsed with water and ethanol, dried at 60 °C for 24 h, and calcined for 1 h at 450 °C to obtain the nanostructures. Nanorods with high crystalline quality and length and diameter in the ranges of 50–200 nm and 5–20 nm (Figure 3a,b) proved to be adequate to support PdO NPs. The formation of a

p-n junction at the interface between them and spillover effects in the vicinity resulted in an excellent response of the PdO-WO_3 catalyst (Figure 3c,d) for the detection of hydrogen gas in the temperature range of 25 to 350 °C, exhibiting the highest response of 3.14×10^6 with a short response time of 1.8 s to 3 vol% H_2 at the ideal operating temperature of 150 °C and very high H_2 selectivity against C_2H_5OH, CO, NO_2, NH_3, and H_2S.

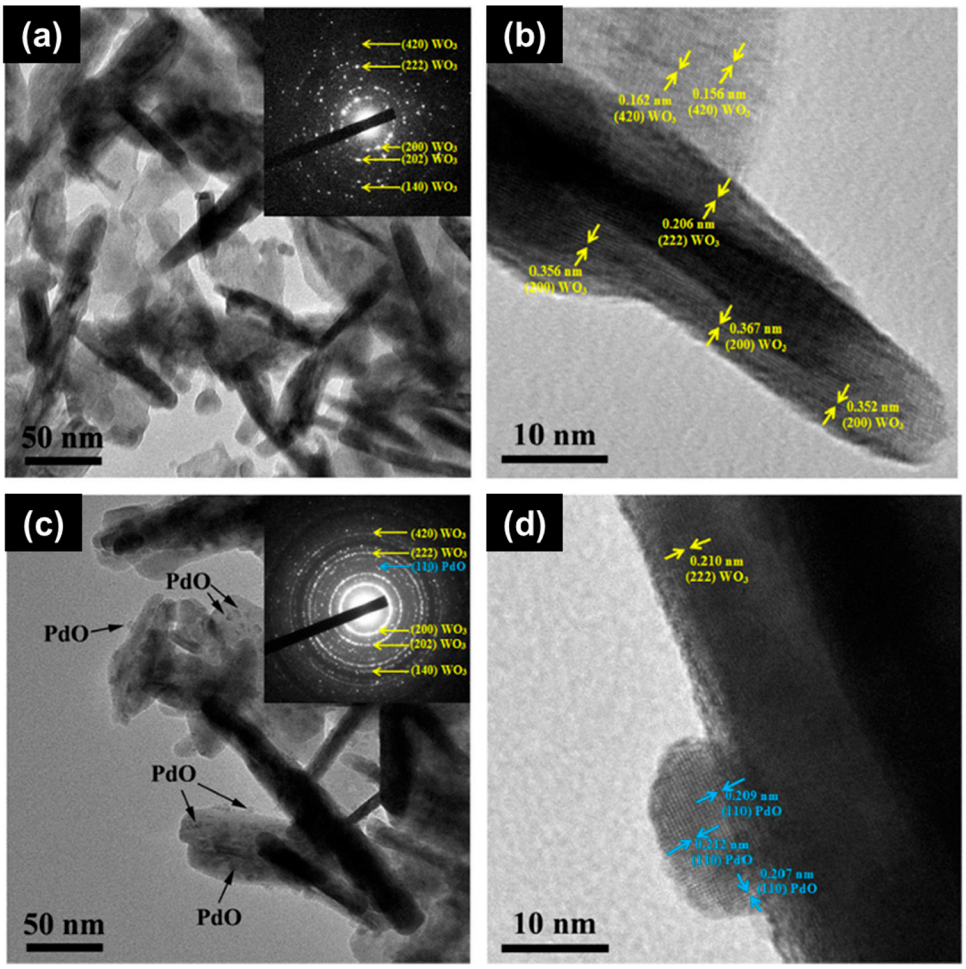

Figure 3. TEM and HR-TEM images of (**a**,**b**) WO_3 nanorods and (**c**,**d**) 2 wt% Pd-loaded WO_3 nanorods and their corresponding SAED patterns in the inserts. Figure printed with permission from Reference [57]. Copyright 2016 Elsevier.

Monoclinic WO_3 nanorods synthesized by the acidification of a STH solution and cetyltrimethyl ammonium bromide (CTAB) aided by a freeze-drying process and flash heating of the precipitate (500 °C, 5 min) have been shown to be a good electrode material for observing electrochromic behavior during the intercalation and deintercalation of electrons and ions in electrochemical reactions [58]. Zn- and Ag-doped WO_3 nanorods have also been produced by the co-precipitation method and presented good antibacterial activity (*Escherichia coli*, *Pasturellamu ltocida*, *Bacillus subtilis*, *Staphylococcus aureus*) [59] and high photocatalytic degradation (MB dye) [60].

2.1.3. Nanoplates and Nanosheets

Two-dimensional nanostructures such as nanoplates and nanosheets are morphologies often found for WO_3, especially in syntheses using the co-precipitation technique. In addition to the usual characteristics of nano-sized materials, WO_3 2D nanostructures have optical and electronic properties and a surface atomic structure dependent on their specific

structural anisotropy, which can be used as an advantage to tune their properties according to their applications [61,62].

Recently, Mehmood et al. developed a simple co-precipitation synthesis method to produce pure monoclinic WO_3 nanoplates (Figure 1a) and doped with Fe [39], Ni [63], Co [38], Cu [40], and Sn [64]. For synthesis, a 0.1 M aqueous solution of STH and NaCl was acidified (pH = 1) using a 3 M solution of HCl and kept under constant magnetic stirring for 1 h. After that, the solution was centrifuged to collect the precipitate, which was further rinsed several times with water, dried in a furnace for 12 h, and calcined at 300 °C for 2 h to obtain the final product. For doping the WO_3 nanostructures, different molar percentages of precursor salts were also introduced into the solution. The morphology, optical, electrical, and photocatalytic properties of the nanostructures were shown to be affected by the type and concentration of dopant in the structure. In addition, a study of the cytotoxic activity against MCF-7 and Hep-2 cancer cells indicates that the anti-cancer response of WO_3 nanostructures improves with higher dopant content (for all dopants), with the best result being obtained for 5% Ni-doped WO_3 (70 and 65% efficiency for MCF-7 and Hep-2 cancer cells, respectively) [63]. This result was associated with the greater generation of reactive oxygen species (responsible for attacking cancer cells) in the doped samples, resulting from the reduction in the bandgap and the greater efficiency of conversion of visible light in them.

Upadhyay et al. also produced nanosheets of pure monoclinic WO_3 (Figure 1c) and doped with Sn [65], In [66], Fe [67], and Cr [42] with excellent responses as gas sensors from a procedure similar to the previous one. The 2D nanostructures were prepared by adding STH to diluted nitric acid and keeping the obtained solution under magnetic stirring for 48 h and aging for 20 h at rest, after which the precipitate was filtered, washed abundantly with distilled water, dried at 6 °C, and calcined at 500 °C for 2 h in air. Suitable salt precursors were introduced into the solution at the initial stage to produce doped nanostructures. WO_3 nanosheets showed good responses as sensors for the alcohols propanol, methanol, and ethanol [65]; formaldehyde [42,67]; and acetone [66], with improved responses when doped with Sn, Cr, Fe, and In, respectively. Doping changes the morphology of nanosheets, increasing the surface area exposed to air for oxygen adsorption, which leads to the creation of more active sensing sites and, therefore, an increase in response. Yu et al. [68] also reported a good response from Ag-doped monoclinic WO_3 nanosheets synthesized by co-precipitation for acetone sensing; however, the increase in gas-sensitive properties was attributed more to the active regions of spatial charge around the metal–semiconductor junctions (interface between Ag and WO_3) than to changes in surface area.

Photocatalytic degradation of MB dye under visible irradiation was achieved using pure and Ag-doped WO_3 nanoplates produced by the co-precipitation method [60]. Doping is aimed at reducing charge recombination, which leads to an increase in degradation efficiency from 64% for pure WO_3 to 97% for Ag-doped WO_3. Good photocatalytic activity was also identified for the degradation of RhB, indigo carmine (IC), methyl orange (MO), and Congo red (CR) in aqueous solution under UV and UV–Vis radiation using rectangular plates of WO_3 obtained by the co-precipitation method [69].

Two-dimensional nanostructures of tungsten oxide have also shown promise for applications in energy storage devices. Mitchell et al. [70] produced hydrated WO_3 nanosheets ($WO_3 \cdot 2H_2O$) from a co-precipitation process using STH as a precursor and HCl as a precipitating agent, with anhydrous WO_3 obtained from the dehydration of $WO_3 \cdot 2H_2O$ at 350 °C. The presence of structural water in this material leads to ideally pseudo-capacitive behavior in $WO_3 \cdot 2H_2O$ nanoplates, improving their charge retention and energy efficiency for proton storage compared to anhydrous WO_3 nanoplates, with charge/discharge times of just a few seconds and 99% energy storage—much higher than the 77% found for anhydrous WO_3. As both materials have the same morphology, the improvement in charge retention was attributed to the structural hydration of the material, which can constitute a general strategy for use in other transition metal oxides. Wang et al. [61] produced nanosheets of $WO_3 \cdot H_2O$ from the same co-precipitation method with an abundance of W = O and

O–H groups on their surface and facets {101} exposed as active adsorption facets. The optimized structure and morphology of the nanostructures result in a high adsorption capacity of the MB dye (450 mg g^{-1}), fast adsorption rate, and regeneration capacity via photodegradation under ultraviolet light irradiation, making it an excellent candidate for wastewater discoloration.

2.1.4. Hierarchical WO_3 Structures

Hierarchical structures obtained from wet chemical approaches such as co-precipitation exhibit unique properties such as a large surface area, increased light harvesting capacity, good electron transportation, and more channels for the diffusion, adsorption, and exchange of free radicals and molecules, making them very useful for photocatalytic and sensing applications [71,72].

In this sense, Wang et al. [41] synthesized three-dimensional monoclinic WO_3 nanoflowers using the co-precipitation method with STH as a precursor and HCl as a precipitating agent for application as a NO_2 sensor. As shown in Figure 1b, the nanoflowers obtained by this method have a structure assembled from dozens of nanosheets with a smooth surface and irregular edges that connect to each other through the center to form 3D hierarchical structures. Figure 4a,b show TEM images of a bunch of nanoflowers and an individual nanoflower, highlighted in the region within the red square in Figure 4a, confirming the self-assembled structure. The HRTEM image taked from nanosheet circled in Figure 4b shows the adjacent planes (022) of the monoclinic WO_3 lattice (Figure 4c). The corresponding SAED pattern (Figure 4d) confirms the monocrystalline character of the WO_3 nanosheets. According to the authors, the fundamental step to obtain this morphology is a pre-treatment of the precipitate with HCl for 24 h at 40 °C under stirring, followed by the addition of water and stirring for another 9 h. After this treatment, the material is rinsed several times with water and ethanol, dried at 80 °C for 10 h, and calcined at 500 °C to form the nanoflowers. Without the pre-treatment step, the synthesis only results in the formation of irregular nanosheets. Sensors based on WO_3 nanoflowers showed a high NO_2 detection response with a detection limit of ~40 ppb at 120 °C. The good sensing activity was attributed to the morphology of the WO_3 nanoflowers, consisting of well-aligned and spaced nanosheets that provide more active sites for reactions, and the high proportion of the electron-depleted layer in the nanostructure provided by the thin nanosheets. Acetone sensing has also been successfully reported for hierarchical WO_3 spheres synthesized by a similar method combining co-precipitation and pre-treatment with nitric acid [73].

Zhang and Yang [74] showed that the use of surfactants in co-precipitation synthesis is also beneficial for the formation of WO_3 hierarchical structures. In a typical synthesis, STH and CTAB were ultrasonically dispersed in water, nitric acid was introduced to initiate precipitation, and the solution was kept under magnetic stirring for 24 h. The precipitate was then filtered, rinsed with water and ethanol three times, dried at 80 °C overnight, and sintered at 200 °C for 12 h to obtain flowery cubic WO_3 nanostructures with an average diameter of 50–100 nm, high surface area (87 m^2/g), and excellent performance for the adsorption of MB dye (35.95 mg/g at 45 °C). The distinct morphology and phase of WO_3 flowers provide more adsorption sites, promoting greater interaction between adsorbent and adsorbate and thus improving its performance in dye adsorption. Li et al. [75] also used a surfactant-assisted co-precipitation synthesis method to produce hierarchical hexagonal WO_3 nanostructures. Sphere-like architectures were obtained by adding small amounts of polyvinyl pyrrolidone (PVP) (1, 3, and 5 wt.%) to an aqueous solution of STH and using HCl as a precipitating agent. After the reaction, the precipitate was washed with water and ethanol and dried at 60 °C for 3 h in air. The reaction time (90, 120, 180, and 300 min) and the molar ratio of WO_4^{2-}/H^+ in the solution are determining factors in the morphology and size of the architectures. Sphere-like structures were found to be assembled from 1D nanorods. PVP in solution facilitates the rapid formation of metastable phase h-WO_3 nuclei and acts as a soft template for the assembly of WO_3 crystallites. The hexagonal WO_3 sphere-like architectures showed excellent visible light photochromic properties with

good reversibility and were highlighted as good candidates for applications in optical signal processing and smart windows. Priya et al. [76] also reported the use of CTAB and PEG-6000 as surfactants in an acidified STH solution to obtain sponge-like nanostructures of monoclinic WO_3. Kavitha et al. [77] adopted a different strategy, a green co-precipitation route for producing monoclinic WO_3 nanoflakes. The hierarchical structures were obtained by adding tungstic acid (H_2WO_4) to a solution containing biomass from the *F. solani fungus*, which was kept under stirring for 5 h and then calcined at 700 °C for 2 h. The binding habit of fungus biomolecules on the growing WO_3 particles was thought to be responsible for the nanoflakes' morphology.

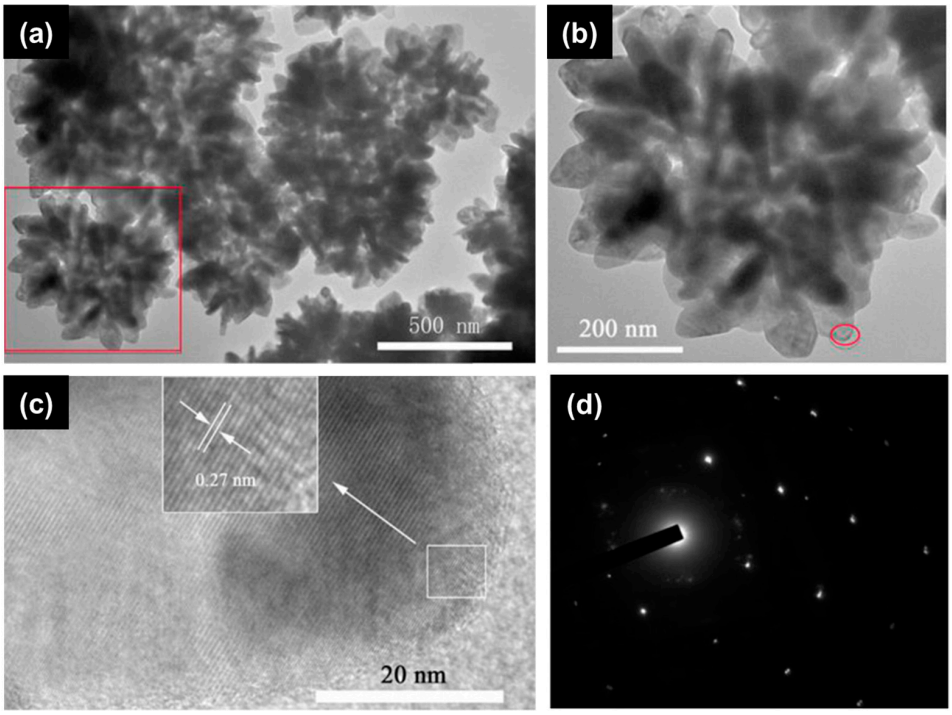

Figure 4. (**a**) TEM image of the hierarchical nanoflowers WO_3, (**b**) the image of an individual nanoflower, (**c**) HRTEM image of a nanosheet of the nanoflower, and (**d**) the SAED pattern of an individual WO_3 nanosheet. Figure adapted with permission from Reference [41]. Copyright 2015 Elsevier.

Huang et al. [78] synthesized hollow sphere-like and flower-like 3D architectures of $WO_3 \cdot H_2O$ from a simpler co-precipitation procedure using STH as the tungsten source, HCl as the precipitating agent, and a mixture of water and ethylene glycol as the solvent. The amount of STH in solution and the aging time determined the morphology of the structures. Corresponding monoclinic WO_3 structures were obtained after calcination at 450 °C for 2 h in air. Photocatalytic experiments showed a good performance of the 3D architectures of WO_3 for the degradation of the RhB dye, with the WO_3 nanostructures similar to hollow spheres promoting the total degradation of the dye under UV and visible light irradiation. The improved response of this architecture was attributed to the hollow structure, which allows a faster diffusion of RhB molecules and greater absorption of incident light.

2.2. Solution Combustion Method

Solution combustion synthesis (SCS) has gained prominence in recent years as a simple, fast, efficient, and versatile method for preparing oxide materials with controlled properties and diverse morphologies [79]. This technique, derived from sol-gel chemistry, offers the advantage of producing high-quality structures in a shorter time [80].

SCS involves a self-sustained redox reaction between a fuel and an oxidizer in a homogeneous aqueous solution. It typically involves one or more thermally coupled

exothermic reactions that provide sufficient energy (heat released during the combustion reaction) to produce at least one solid product and a large amount of gas. Ignition can occur naturally (depending on the exothermicity of the reaction) or be initiated by additional energy sources, such as heat. The gaseous byproducts play a crucial role in SCS, as they generally cause significant expansion of the solid product and rapid cooling upon reaction completion, which can lead to the formation of porous materials—a highly desirable characteristic at the nanoscale [81,82].

The stoichiometric proportion between oxidizer and fuel allows the calculation of the valences of the oxidizers/reducers, facilitating the prediction of the material produced based on propellant chemistry [83]. However, the final product in SCS results from a combination of parameters such as the type of fuel, metal cation precursors, pH, oxidizer/fuel ratio (Φ), atmosphere, and initiation type (heat, electricity, radiation, etc.). Carlos et al. [84] provide a detailed overview of how these parameters influence SCS.

Despite its advantages, SCS has limitations, including the agglomeration of nanostructures, difficulty in controlling morphology, and potential contamination with organic combustion residues [85]. Incomplete combustion reactions can also produce harmful gases like NO_x and CO, leading to safety and environmental issues [86]. Nevertheless, solutions are being developed to address these challenges, and SCS has evolved to reliably produce versatile and efficient metal oxides at low processing temperatures. It has become especially prominent in the production of nanoparticles (for sensors, catalysis, and biomedical applications) and thin films (for devices such as memories, solar cells, and thin film transistors) [87].

In recent years, the number of studies focusing on obtaining WO_3 with tailored designs through SCS has increased, driven by the efficiency, time, and cost savings provided by this technique. Although it remains a less conventional route, SCS has successfully produced WO_3 in various phases—orthorhombic, hexagonal, or monoclinic—with morphologies including nanorods [88], nanoparticles [89], porous structures [85], and NP films [90], among others.

2.2.1. Nanoparticles

WO_3 nanoparticles are the most common morphology obtained in solution combustion synthesis. By adjusting control parameters, it is possible to produce NPs with different phases, shapes, and sizes using this method. For instance, Kaplan et al. [89] demonstrated that the fuel/oxidizer ratio (Φ) is crucial in determining the crystallite size of hexagonal WO_3 NPs synthesized by SCS. In their study, nanostructures were produced by adding ammonium tungsten oxide hydrate to an aqueous solution of oxalic acid (Φ = 1 or Φ = 5), followed by stirring to homogenize the solution, combustion in a muffle furnace at 400 °C, washing with ethanol to remove residues, and finally, calcination at 500 °C for 8 h.

The experimental data showed that increasing the fuel/oxidizer ratio from Φ = 1 to Φ = 5 results in partial particle melting and coarsening of the WO_3 powder, causing the laminar-like structures to disappear and increasing the crystallite size from 7.96 nm to 42.27 nm. Additionally, NPs produced with a higher fuel/oxidizer ratio demonstrated greater efficiency in the photocatalytic degradation of MB dye under sunlight. The authors noted that although these NPs (Φ = 5) have a smaller surface area and higher bandgap energy compared to those with Φ = 1, their catalytic performance is superior. This improvement is attributed to the higher amount of carbon on their surface (3.90% vs. 2.70% for Φ = 1), which provides additional adsorption sites and accelerates photocatalytic reactions. Moreover, the larger crystallite size of these NPs reduces electron–hole recombination, which is more prevalent in smaller crystals.

Chen et al. [91] highlighted another interesting aspect of WO_3 nanostructure production using solution combustion synthesis (SCS): different fuels produce samples with varying morphologies and phases. They demonstrated that nanometric, non-stoichiometric oxides rich in oxygen vacancies exhibit good photocatalytic activity for MB dye degradation under visible and UV light. This was achieved by controlling the ratios between the

precursor paratungstate and fuels such as glycine, urea, and urea–citric acid. According to the authors, the key to producing non-stoichiometric tungsten oxide (WO_{3-x}) is the network structures formed by the organic fuel during synthesis, through dehydration polymerization between amine and carboxyl groups. The morphology, phase, and dispersibility of the nanostructures were strongly dependent on the type and proportion of fuel used. For example, increasing the glycine fuel in the synthesis led to a transition in morphology. In the absence of glycine, urchin-like structures were formed, consisting of a mixture of $WO_3 \cdot 0.33H_2O$ and hydrotungstite, whereas with glycine, quasi-spherical orthorhombic WO_3 NPs were produced.

Aliasghari et al. [92] found similar results in their synthesis of WO_3 NPs. They produced amorphous quasi-spherical nanoparticles (~50 nm), rock-like amorphous irregular particles, and spherical nanoparticles of monoclinic WO_3 (~300 nm) using tungstic acid as the metal source and oxalic acid, citric acid, and glycine as fuels, respectively. The changes in the morphology and structure of the NPs were attributed to the different reaction energies of the fuels and the formation of amine groups during the reaction. Furthermore, these authors demonstrated that the heat source also plays a significant role in SCS [83]. They showed that heating on a hot plate (200 °C) resulted in orthorhombic WO_3 nanostructures, while heating in a muffle furnace (550 °C) produced tetragonal WO_3 nanostructures. These differences were linked to the heating characteristics: a hot plate allows rapid heating and cooling with a layer-by-layer ignition mechanism, resulting in metastable structures, whereas a muffle furnace provides gradual heating and cooling, leading to more stable structures.

Other studies have also explored the properties of SCS-produced WO_3 NPs for dye photodegradation. Singh et al. [93] showed that triclinic WO_3 faceted NPs (size 25–500 nm), produced using ammonium metatungstate hydrate as the oxidizer and glycine as the fuel, exhibited a good MB dye degradation activity under UV illumination (~68% efficiency). The performance improved when these NPs were used to create composites with commercial TiO_2 NPs. Composites with 15% triclinic WO_3 NPs demonstrated excellent performance for various anionic (orange G, amido black 10B, alizarin cyanin green, and indigo carmine) and cationic (MB, malachite green, rhodamine 6G, and pyronin Y) dyes under both visible and UV irradiation. Pudukudy et al. [94] also achieved excellent results with monoclinic WO_3 nanospheres synthesized using ammonium tungsten oxide pentahydrate as the oxidizer and urea as the fuel. These nanospheres showed 99% adsorption in 5 min and 100% photodegradation of MB dye in 4 h under visible light, which was attributed to their increased surface area and dangling-bond density.

Recently, Liu et al. [95,96] demonstrated that monoclinic WO_3, hexagonal $WO_3 \cdot 0.33\ H_2O$, and hexagonal $WO_3 \cdot 0.33\ H_2O@C$ NPs, synthesized by SCS using ammonium tungstate as the tungsten source, urea as the fuel, and nitric acid as the oxidant, are promising candidates for lithium-ion battery electrodes. The $WO_3 \cdot 0.33\ H_2O@C$ electrode showed a superior performance due to the high electronic conductivity of the amorphous carbon layer and the unique hexagonal structure of the NPs, which provides efficient channels and more active sites for electronic transport. This electrode exhibited long cycle stability and excellent rate capability (816 mAh g^{-1}, 200 cycles, 100 mA g^{-1}).

2.2.2. Nanorods

Nanorods represent another significant morphology produced by solution combustion synthesis. The high surface area of these nanostructures, combined with the physicochemical properties of WO_3, makes them attractive for a range of applications. Vidya et al. [88] demonstrated that monoclinic WO_3 nanorods synthesized by SCS have potential uses in UV sensors and filters, warming coatings, solar control, antireflection coatings, low-temperature cofired ceramics, and electronic substrates. For their synthesis, they used an aqueous solution of ammonium paratungstate as the precursor, citric acid as a complexing agent, nitric acid as an oxidizer, and ammonium hydroxide solution as the fuel ($\Phi = 1$). The solution was kept at neutral pH and stirred for homogenization. It was

then heated to 250 °C on a hot plate, resulting in a voluminous fluffy powder composed of polycrystalline WO_3 nanorods with widths of 40 nm and lengths ranging from 40 to 100 nm. The potential applications of these nanostructures were evaluated using Raman, FTIR, UV–Vis, PL spectroscopy, and low-frequency dielectric measurements.

Kaplan and Sönmez [97] synthesized hexagonal WO_3 nanorods using a simplified SCS procedure. They used ammonium tungsten oxide hydrate as the oxidizer, citric acid as the fuel, and ammonium nitrate as an additional oxidizer. The reagents were dissolved in water and then ignited in a muffle furnace at 400 °C. After combustion, the powder was washed with ethanol and calcined at 500 °C to obtain the desired nanostructures. They explored the effects of ignition temperature, fuel/oxidizer ratio, and ammonium nitrate amount on the morphology and phase of the structures. Evecan et al. [90] also achieved hexagonal WO_3 nanoneedles using tungsten ammonium oxide hydrate as the oxidizer and oxalic acid as the fuel ($\Phi = 1$), without a subsequent calcination step. The nanoneedles were synthesized from a mixture of aqueous solutions of the oxidizer and fuel, followed by magnetic stirring for 15 min, combustion at 300 °C, and rinsing with ethanol. The resulting powder was dried at 80 °C overnight. Thin films of these nanoneedles, deposited using an e-beam technique, exhibited a high coloration efficiency, optical transmittance modulation, and rapid coloration and bleaching during ±1 V switching, making them promising for electrochromic devices such as smart windows.

Salkar et al. [98,99] produced WO_3 nanorods using a soft SCS method with urea as the fuel. They acidified an aqueous solution of sodium tungstate dihydrate with HCl (2M) to form a colloidal tungstic acid gel, which was then washed to remove Na^+ and Cl^- ions by centrifugal filtration. An aqueous solution of pure urea or NH- or CH-substituted urea was prepared and added dropwise to the gel under constant stirring, adjusting the pH to 2 with HCl. The hybrid gel was digested in a water bath at 90 °C for 3 h and then calcined in air at 550 °C for 2 h in a muffle furnace. Solutions containing pure urea and NH- or CH-substituted urea produced WO_3 nanorods and WO_{3-x}, respectively. NH substitution induced one-dimensional growth of nanorods along the (002) plane and facilitated the creation of oxygen vacancies on the surface, resulting in WO_{3-x} nanorods with W^{5+}/W^{6+} redox surface states. These WO_{3-x} nanorods synthesized using carbohydrazide showed the highest area-specific capacitance (132 mF cm^{-2}) and excellent capacitance retention compared to other nanorods produced with CH-substituted urea and pure urea.

2.2.3. Hierarchical WO_3 Nanostructures

The gases released during the combustion reaction in SCS greatly facilitate the formation of hierarchical structures. These interconnected pores and channels enhance the material's surface area and create more active sites, which is particularly desirable for electrochemical and sensing applications. Dong et al. [100], for example, designed a straightforward SCS process to produce hierarchically porous WO_3 microstructures using fresh peroxotungstic acid as the tungsten source and a mixture of glycine and hydrazine hydrate as the fuel (reaction at 400 °C for 30 min). These WO_3 microstructures were tested as acetone sensors and demonstrated an excellent performance at 300 °C for concentrations ranging from 5 to 1000 ppm. They showed a high gas response and rapid response and recovery times, comparable to sensors based on pure WO_3 and WO_3 composites produced using other techniques. The superior sensing performance was attributed to the increased number of active sites provided by the porous WO_3 microstructure, which enhances interaction with gas molecules adsorbed on the surface.

Aliasghari et al. [83] produced sponge-like structures using SCS with tungstic acid as the metal source and glycine as the fuel. They employed either a hot plate or a muffle furnace to initiate the combustion reaction. Combustion on a hot plate resulted in amorphous sponge-like structures, whereas combustion in a muffle furnace produced tetragonal-phase sponge-like structures with a crystallite size of 16.7 nm. The electrochromic performance and photodegradation efficiency of reactive blue dye were evaluated, showing that the heat

source significantly influenced the results. The sample produced using the muffle furnace exhibited a superior performance in both applications due to its crystalline structure.

Salkar et al. [98] applied a similar method to produce 3D WO_3 nanoporous structures. By maintaining the temperature at 550 °C and increasing the calcination time, the nanorods self-assembled into complex 3D structures featuring numerous edges, kink sites, and porous channels. These structures provide a high surface area and specific capacitance (148 F g^{-1}) compared to smaller nanostructures. The enhanced electrocapacitive performance was attributed to the 3D surface heterostructure, easy diffusion of H^+ ions through the porous channels, and a greater number of active sites due to the increased electroactive area.

Recently, the same authors developed a simple SCS route to synthesize a DNA-like double helical WO_{3-x}/C microfiber superstructure via the self-assembly of in situ carbon fiber-encapsulated WO_{3-x} nanorods (Figure 5). The synthesis involved acidifying an aqueous solution of STH with HCl and continuously stirring (1200 rpm) to form a colloidal tungstic acid sol. Na^+ and Cl^- ions were removed by centrifugal filtration. An aqueous citric acid solution with pH = 2 was then added dropwise to the solution under vigorous stirring (1200 rpm), forming a precursor gel. This gel was refluxed in an oil bath at 100 °C for 6 h and then calcined at 450 °C in a muffle furnace to produce the DNA-like double helix WO_{3-x}/C microfiber superstructures. It is believed that carbon fibers were formed in situ during the incomplete combustion of citric acid, with the dominant surface plane (002) of the growing WO_{3-x} nanorods catalyzing their growth similarly to reduced graphene oxide (rGO) in the 200–450 °C temperature range. The size heterogeneity of the WO_{3-x} nanorods suggests that the carbon encapsulation rate competes with the growth kinetics of the WO_{3-x} nanorods. Hydrogen bonds or van der Waals interactions are thought to induce the helicity of the structures, with WO_{3-x} nanorods integrating between the growing helical filaments, leading to the formation of a DNA-like double helical superstructure. Electrocapacitive measurements indicated that these 3D WO_3 nanoporous structures are excellent candidates for supercapacitor fabrication, with fast electrode–electrolyte interfacial kinetics, good electrical conductivity, and cycle stability resulting in a high area-specific capacitance (401 mF cm^{-2} at 2 mA cm^{-2}), capacitance retention of over 94% after 5000 cycles, and a power density of 498 W kg^{-1}.

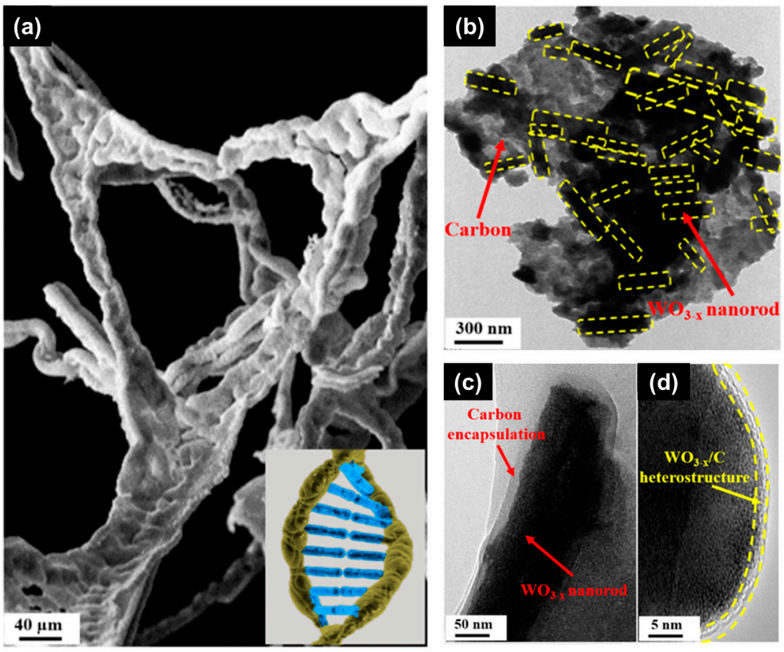

Figure 5. (**a**) SEM image depicting DNA-like double helical tripodal microfiber superstructure along with a representative DNA image shown in the inset for comparison. (**b**–**d**) represents HRTEM and SAED analysis of this structure. (**b**) The yellow dashed lines indicate the position of WO_{3-x} nanorods. (**c**) Carbon encapsulation around WO_{3-x} nanorods. (**d**) The yellow dashed line indicates the WO_{3-x}/C heterostructure. Figure reprinted with permission from Reference [101]. Copyright 2021 ACS.

2.3. Sol-Gel Method

Sol-gel synthesis is a versatile and widely used method in materials science and chemistry for creating various materials with controlled properties. It involves transforming a sol, which is a stable colloidal suspension of nanoscale particles in a liquid medium, into a gel-like network through controlled chemical reactions [102]. The process of sol-gel synthesis can be summarized in several key steps. The aqueous sol-gel process typically includes five main stages: sol formation; hydrolysis; condensation; gelation; and aging, drying, and calcination, as illustrated in Figure 6 [103].

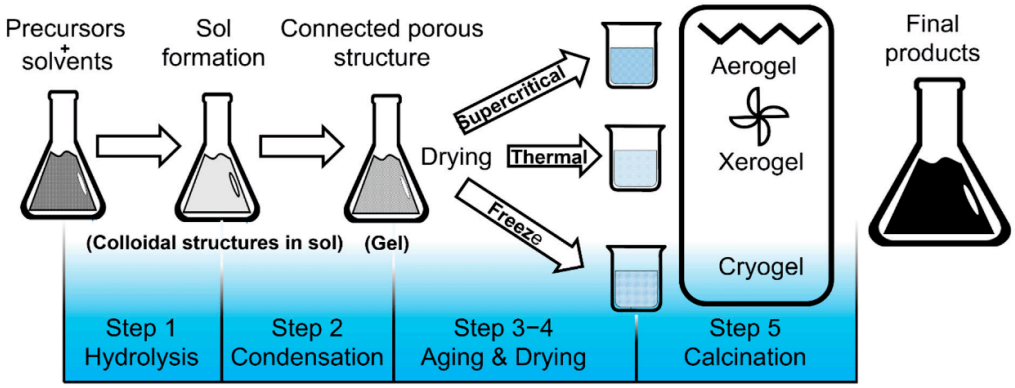

Figure 6. Schematic illustration of step-by-step sol-gel method. Adapted with permission from Reference [103].

1. **Sol Formation**: The process begins with preparing a sol, which consists of a precursor material dissolved in a suitable solvent. The precursor can be a metal alkoxide, a metal salt, or other chemical species capable of undergoing hydrolysis and condensation reactions.

2. **Hydrolysis**: Water molecules from the solvent react with the precursor, breaking down chemical bonds and usually forming metal hydroxide groups. This hydrolysis step generates smaller molecular fragments that are more reactive and capable of interacting with each other.
3. **Condensation**: The hydrolyzed species undergo condensation reactions, where they react with each other to form covalent bonds. This leads to the formation of a three-dimensional network of interconnected nanoparticles. The extent of condensation determines the final structure and properties of the gel.
4. **Gelation**: As the condensation reactions progress, the sol gradually transforms into a gel, a semi-solid material with a three-dimensional network structure. The gelation process can be controlled by adjusting parameters such as precursor concentration, solvent composition, pH, and temperature.
5. **Aging, Drying, and Calcination**: The gel undergoes an aging process to further enhance its structural integrity and properties. Following aging, the gel is carefully dried to remove the solvent, which is critical to prevent cracking and shrinkage. Depending on the desired properties and applications of the final material, additional heat treatments, such as annealing or calcination, may be performed to promote crystallization and improve material properties.

The sol-gel synthesis method offers several advantages, including the ability to create materials with controlled porosity, composition, and structure at the nanoscale. It has applications in a variety of fields, such as ceramics, glass, coatings, catalysts, sensors, and biomedical materials. The precise control over synthesis parameters enables researchers to tailor the properties of the resulting materials for specific applications, making sol-gel synthesis a valuable tool in modern materials science.

However, the method also has its drawbacks. One significant challenge is the difficulty in maintaining consistent synthetic control, as variations in synthesis parameters can lead to products with different morphologies. Additionally, the process requires strict control of hydrolysis and condensation reactions, making it technically demanding [103,104].

The sol-gel method has been extensively explored for fabricating metal oxide nanostructures, particularly in engineering and technical applications, due to the precise control over shape and size that this technique offers [105–108]. Sol-gel materials are valued for their exceptional thermal, optical, magnetic, mechanical, and electrical properties, making them suitable for a wide range of applications. The technique allows for the cost-effective production of various materials, including thin films, nanoparticles, glass, and ceramics.

Further advantages of the sol-gel process include a high surface-to-volume ratio, the ability to synthesize at low temperatures, and consistent reproducibility [29,109]. Unlike solid-state reactions, sol-gel synthesis can achieve metal oxides at reduced temperatures.

The role of WO_3 nanostructures in chemical reactions is crucial, as their specific design significantly impacts their applicability across various fields. Tailoring WO_3 nanostructures is essential for optimizing process efficiency and enabling effective recovery of the photocatalyst during subsequent treatment stages. A substantial body of research has focused on developing WO_3 nanostructures with distinct attributes [110,111]. These nanostructures can be classified into zero-dimensional (0D), one-dimensional (1D), two-dimensional (2D), and three-dimensional (3D) configurations. Within these categories, there are further distinctions, such as quantum dot arrays, elongated arrays, planar arrays, and ordered structures. For example, Figure 7 illustrates diverse morphologies of tungsten oxides across different dimensions. In the 1D category, notable examples include nanorods, nanofibers, nanowires, nanotubes, and nanoneedles [112–115]. In contrast, 2D and 3D arrays include nanosheets and nanoflowers, respectively.

WO_3-based nanomaterials have become increasingly significant in emerging fields such as photovoltaics, electronics, and photocatalysis due to their remarkable stability, mechanical robustness, and high electron mobility. For instance, nanosized WO_3 quantum dots are effectively used as sensing receptors in fluorescent probes for detecting copper (II) ions in water, owing to their high quantum yield and enduring stability [116]. Additionally,

the extensive potential of 1D WO_3 is evident in electronics, optoelectronics, and gas sensing. A study by Debsai et al. [117] explored the mechanical strength of WO_3 nanowires, revealing their exceptional fracture strain and positioning them as promising candidates for nanoscale sensors and actuators.

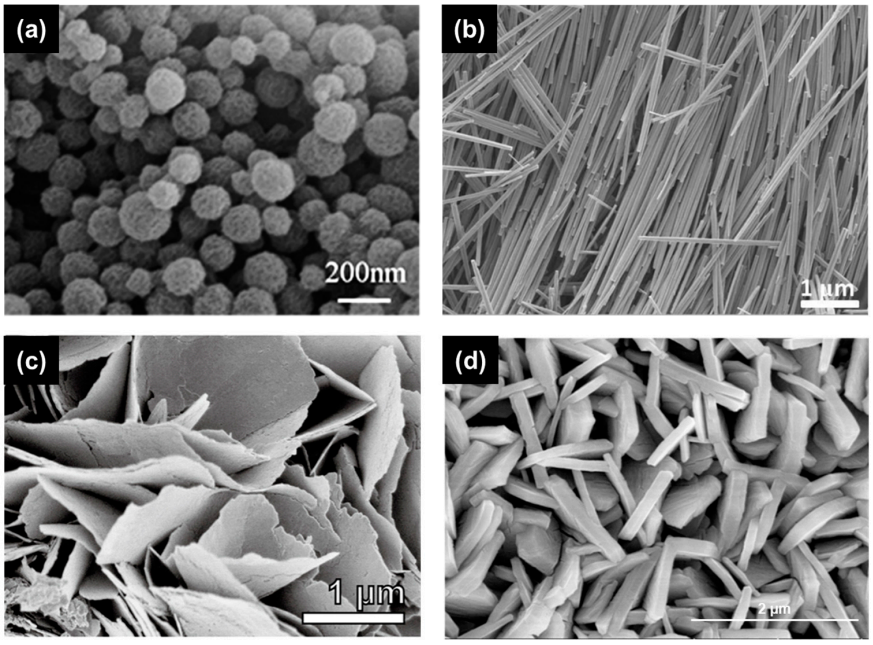

Figure 7. FESEM and SEM images for (**a**) 0D, (**b**) 1D, (**c**) 2D, and (**d**) 3D WO_3 nanostructures. Adapted with permission from References [118–121].

2.3.1. Nanoparticles

Abbaspoor et al. [7,122] produced WO_3 nanoparticles using the sol-gel method for photocatalysis applications. For synthesis, 3 g of sodium tungstate dihydrate (STD) was dissolved in 100 mL of deionized water. Then, 2 M HCl was added to the solution to reach the desired pH levels (1, 1.5, and 2). The solution was stirred for 15 h at 50 °C to obtain the gel. The gel was then washed four times with deionized water and once with ethanol to remove all impurities. The washed material was transferred to an oven at 80 °C for 24 h to evaporate the solvents and subsequently calcined at 500 °C for 90 min. The results showed that the solution pH significantly influenced the average particle size, with particles synthesized at pH 2 resulting in larger average sizes than those synthesized at pH 1. Additionally, the energy bandgap and absorption spectrum of the nanoparticles were also affected by the synthesis pH. Specifically, the nanoparticles synthesized at pH 1 exhibited high absorption in the UV region and an indirect bandgap of 2.74 eV, making them promising candidates for photocatalytic applications due to their efficiency in light absorption and potential in the decomposition of organic pollutants. WO_3 NPs synthesized under the same conditions also demonstrated an excellent performance in the treatment of acidic wastewater [123].

Susanti et al. [124] synthesized WO_3 NPs with grainy shapes and a size range of 25–550 nm using a tungsten alkoxide as a precursor, ammonium hydroxide as a precipitating agent, and Triton X-100 as a surfactant. The size, morphology, and crystallinity of the NPs were highly dependent on the calcination temperature. Further studies also showed that WO_3 NPs have a good response as CO sensors, with samples calcined at 500 °C showing a better performance due to their greater gas adsorption capacity [125].

Luxmi and Kumar [126] synthesized pure-WO_3 and Fe-doped WO_3 NPs using egg albumen as a solvent. From the process, monoclinic phase NPs with a cuboid-like shape, nano-pores on the surface, and catalytic activity in the degradation of MB dye were obtained. WO_3, WO_3-TiO_2, and NiO-WO_3 NPs synthesized via sol-gel have also shown a good

catalytic activity for the reduction of Cr(VI) [127], HC, NO_x, and CO gases [128] and CO_2 gas [129], respectively. The results were attributed to WO_3 which acts by increasing the generation rate of electron–hole pairs and suppressing the recombination of photo-generated charges.

2.3.2. Nanorods and Nanofibers

Brahimi et al. [130] synthesized WO_3 nanofibers via the sol-gel method as follows. Initially, 5 g WO_3 powder (commercial) was dissolved in 400 mL of ammonia solution under stirring at a temperature of 80 °C. Then, the solution was cooled naturally and agar gelling agent (10^{-2} mL^{-1}) was added to it. The solution was heated to 100 °C and a black gel was obtained. The wet gel was dried at room temperature, ground in a mortar and pestle, and calcined at 500 °C for 8 h (heating rate 5 °C min^{-1}). The optical properties of orthorhombic WO_3 nanofibers were investigated, and direct and indirect bandgaps of 2.82 eV and 2.54 eV, respectively, were detected for the material.

Ghasemi and Jafari [131] synthesized WO_3 nanorods using sodium tungstate as a precursor and oxalic acid and PEG as chelating and resin agents, respectively. First, sodium tungstate was dissolved in water and the solution was acidified (pH 1–2) with a solution of HCl and HNO_3 (molar ratio of 1:1). Over time, a yellowish precipitate was formed and converted into a soft gel. Then, the gel was rinsed several times with hot distilled water and allowed to age at the same temperature. Oxalic acid and PEG, in appropriate proportions, were introduced into the synthesis. The samples were then dried at 150 °C and calcined at 550 °C for 90 min to yield WO_3 nanorods. The analyses performed indicate that the morphology of the sample is dependent on the content of oxalic acid and PEG in the synthesis; larger amounts of these agents result in a transition from the morphology of nanorods to granular and spherical particles.

WO_3 nanorods were also synthesized by Ahmed et al. [132] without the use of capping agents from the aging of an acidic aqueous solution of sodium tungstate at a suitable temperature. SEM analysis showed that the morphology of the samples changed from nanorods to nanosheets as the calcination temperature increased from 400 to 500 °C. The effect was associated with the high Gibbs free energy value at higher temperatures that favors the agglomeration of WO_3 seeds in all directions leading to the formation of 2D structures. Due to the high surface area, an increased photocatalytic activity was observed for nanosheets compared to WO_3 nanorods.

2.3.3. Thin Films

The sol-gel method is widely used in the production of WO_3 thin films due to its cost-effectiveness and the ease of depositing uniform films over large areas. In addition, the technique offers the possibility of controlling the film structure early in the process.

Thin films of WO_3/WO_{3-x} were developed by Ramanavičius et al. [133] using a deposition mechanism on glass substrates via the sol-gel method. Initially, 1 × 2 cm glass slides were cleaned in an ultrasonic bath with acetone, ethanol, and deionized water for 15 min in each solution. STD and ammonium oxalate were dissolved in distilled water, and hydrochloric acid was added under stirring at 40 °C, followed by H_2O_2 to form peroxotungstic acid (PTA). EtOH was added as a reducing agent. The glass slides were dipped into the PTA + ethanol solution and incubated for 140 min at 85 °C. After forming the coating, the slides were rinsed with distilled water, dried at 40 °C for 10 h, and annealed at 500 °C for 2 h with a gradual heating rate of 1 °C/min. The results showed that a non-stoichiometric monoclinic phase WO_3/WO_{3-x} film was formed. SEM analysis revealed a dense layer composed of randomly oriented sub-micrometric particles forming a network with a high surface area. The material also demonstrated variable sensitivity to different volatile organic compounds and ammonia, depending on the film's operating temperature as a sensor.

Zeng et al. [134] synthesized amorphous WO_3/ordered porous crystalline WO_3 stacked films (a-WO_3/OP-c-WO_3) by the electrodeposition-assisted sol–gel method using

polystyrene (PS) spheres as templates. Initially, an ordered porous crystalline WO_3 film (OP-c-WO_3) was obtained from the following procedure. In an ice bath, a solution containing 20 mL of H_2O_2, 5 mL of deionized water and 5 g of tungsten was prepared. The solution was filtered and the obtained clear yellow liquid was mixed with an aqueous ethanol solution and kept under stirring at 45–50 °C for 2 h to obtain a tungsten sol. ITO substrates coated with polystyrene (PS) spheres were dipped in the tungsten sol for 15 min and then allowed to dry at room temperature. After, the substrates were dried at 60 °C for 48 h, soaked in toluene for 48 h, dried at room temperature, and then calcined at 400 °C for h. Afterwards, an amorphous WO_3 layer was electrodeposited on the film obtained using the film itself (OP-c-WO_3/ITO) as the working electrode and the diluted tungsten sol as the electrodeposition solution. The amorphous WO_3/ordered porous crystalline stacked WO_3 films (a-WO_3/OP-c-WO_3) for different electrodeposition times are shown in Figure 8. As the deposition time increases, the pore diameter gradually decreases until they are completely covered by the amorphous film. Films electrodeposited with 250 s showed a porous structure, high surface area, high roughness, and superior electrochromic properties compared to the others.

Ge et al. [135] synthesized WO_3 films fabricated from the dip-coating deposition of a peroxotungstic acid sol on a glass substrate and studied the effect of the crystallinity on their properties. The crystallinity and morphology were significantly altered by the annealing temperature of the films (150–400 °C). At 150 °C, only the presence of peroxotungstic acid was observed, at 200–300 °C the formation of an amorphous WO_3 disk-like film was observed, and from 350 °C onwards there was the formation of monoclinic WO_3. Further studies revealed that the electrochromic process is controlled by electron diffusion and that crystalline films are more susceptible to electrochromism, presenting greater optical modulation after electrocoloration, which suggests that electron transport is more effective in these materials.

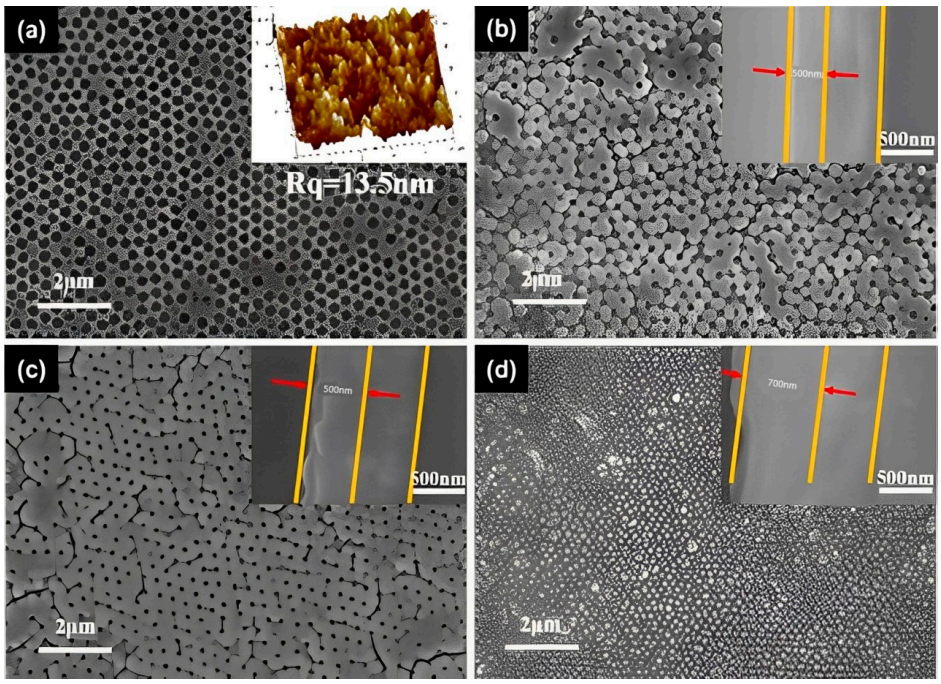

Figure 8. SEM images of a-WO_3/OP-c-WO_3 films obtained with electrodeposition times of (**a**) 150 s, (**b**) 200 s, (**c**) 250 s, and (**d**) 300 s. The insets are AFM and SEM images of the cross-section of the samples. Figure reprinted with permission from Reference [134]. Copyright 2024 Elsevier.

WO_3 composite films synthesized via sol-gel have also been widely explored in recent years. Multilayer porous Pd-WO_3 composite thin films [136], WO_3/RGO nanocomposite film [137], polyacrylic acid/tungsten oxide (PAA/WO_3) films [138], SiO_2/WO_3/ZnO

films [139], WO_3-TiO_2 films [140], and g-C_3N_4/WO_3 thin films [141] have been successfully synthesized and have been employed in hydrogen sensing, electrochromic applications, solar cells, anticorrosion, and photocatalytic water purification, respectively.

2.3.4. Other Structures

Zhuiykov et al. [142] report in their work the synthesis of quasi-two-dimensional WO_3 nanoflakes using a two-step process called sol-gel-exfoliation using STD and nitric acid as precursor and precipitating agents, respectively. Higher calcination temperatures resulted in the production of larger nanoflakes; the increase in temperature appears to promote the agglomeration of nanoparticles during the process, which leads to the formation of larger crystallites. Orthorhombic WO_3 nanoflakes produced by this method proved to be an excellent catalytic material for HER with high activity and stability in water, in addition to being potential candidates for the production of semiconductor-based devices.

Saasa et al. [143] synthesized hierarchical flower-like pure WO_3 and Co-doped WO_3 by a simple sol-gel method using carbon spheres as a template. The hierarchical flower-like pure WO_3 obtained in the process was shown to be self-assembled by nanorods with a monoclinic phase and crystallite size of 8.73 nm. Due to the small crystallite size, high surface area, and defects of WO_3, the nanostructures showed a good response in acetone sensing, especially when doped with 0.6% Co.

The synthesis by the sol-gel method of orthorhombic and monoclinic WO_3 microspheres for the catalytic removal of DEET [144], porous sphere en-WO_3/g-C_3N_4 composite photocatalyst for H_2 production [145], and TiO_2/WO_3 nanospheres for MB degradation [146], among other structures have also been reported in the literature.

2.4. Electrospinning Method

Electrospinning is a cost-effective and efficient technique for producing nanofibers, with its origins dating back to the 1930s but gaining significant attention only after its rediscovery in the 1990s. The term "electrostatic spinning" aptly describes the process, which involves applying electrostatic force and rotational motion to an extruded polymer solution [147,148]. The setup includes four main components: a high-voltage power source, a needle electrode connected to the polymer solution, a capillary for delivering the precursor solution, and an earthed collector, where the final material will be formed (as shown in Figure 9). Applying a high voltage between the ejection point and the grounded collector starts the process. The polymer solution, fed through a syringe, becomes charged under the applied voltage, forming a Taylor cone. The interaction between electrostatic forces and surface tension drives the spinning motion. As the polymer jet reaches the collector, the solvent evaporates and electrostatic repulsion stretches the jet. The characteristics of the final product depend on various factors, including the properties of the polymer solution, operational parameters, and environmental conditions such as temperature and humidity [149,150].

Recently, electrospinning has garnered significant interest due to its low cost, high efficiency, and reproducibility. The technique is being explored across various research fields for its potential benefits. In environmental applications, nanofibers play a crucial role, particularly in oil spill remediation, where porous membranes made of nanofibers are utilized for their exceptional absorption and multifunctionality. Colloidal nanofibers, noted for their unique surface roughness and enhanced properties from colloidal particles, show promise in filtration, adsorption, and sensing applications. Their high aspect ratio provides excellent charge transport properties, reducing interfacial electron interactions at grain boundaries. This feature is beneficial for improving the performance of light-harvesting devices such as dye-sensitized solar cells (DSSCs) and photocatalytic systems [151,152].

In the realm of optoelectronics, a specialized type of electrospun nanofibers known as conjugated polymer filaments has the potential to revolutionize future devices, enabling the creation of lightweight and flexible products. Additionally, the field of medical research has shown considerable interest in electrospinning, particularly for developing effective

drug delivery systems, where high encapsulation and loading efficiency are crucial for various pharmaceutical agents.

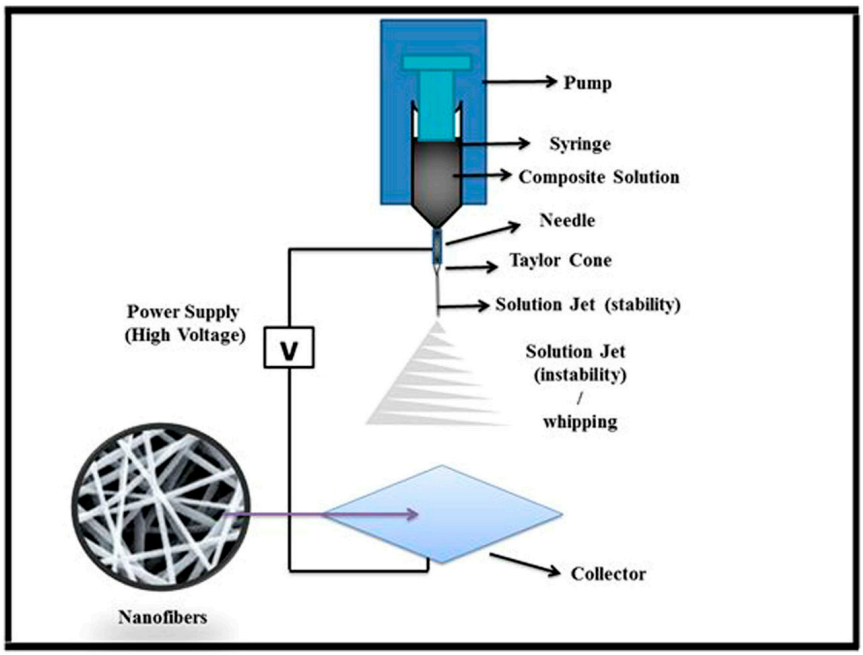

Figure 9. Schematic illustration of a typical electrospinning setup. A composite solution is ejected under high voltage, forming a stable Taylor cone that transitions to an unstable whipping jet, resulting in the deposition of nanofibers on the collector, indicated by the purple arrow. Adapted with permission from Reference [153].

Recently, the electrospinning technique has gained significant attention for the production of one-dimensional (1D) WO_3 nanofibers (NFs). This process involves electrospinning a solution of metal salts and a polymer template, followed by calcination at high temperatures [154–156]. Despite its promise, electrospinning WO_3 NFs has encountered challenges, including the limited availability of suitable solvents and the difficulty in achieving the necessary viscosity for stable electrospinning. Additionally, the inherent brittleness of WO_3 NFs impedes their flexibility, which complicates their handling and use in membrane applications. Consequently, there is an ongoing need for the development of flexible nanofiber membranes or textiles.

The fabrication process of WO_3 NFs typically involves three main stages:

1. **Formulation of the Electrospinning Solution**: A solution is prepared containing a polymer and a sol-gel precursor for WO_3.
2. **Electrospinning**: The solution is electrospun under optimal conditions to create nanofibers that include both the inorganic precursor and the polymer.
3. **Calcination**: The temperature is raised to perform calcination or chemical conversion on the precursor, resulting in WO_3 nanofibers and the removal of all organic components from the fibers.

Researchers have used various metal precursors in electrospinning to synthesize 1D WO_3 NFs. Typical electrospinning solutions include a salt precursor, a polymer matrix, and a volatile solvent such as ethanol, water, chloroform, isopropanol, or dimethylformamide (DMF). The choice of polymer—such as poly(vinyl alcohol) (PVA), poly(vinyl pyrrolidone) (PVP), poly(vinyl acetate) (PVAc), poly-acrylonitrile (PAN), poly(methyl methacrylate) (PMMA), or poly(acrylic acid) (PAA)—depends on its solubility in the solvents and compatibility with metal salts like zinc acetate and copper nitrate [157].

Despite some limitations, electrospinning offers a key advantage: it allows precise control over the morphology of the resulting fibers during both the electrospinning and calcination processes. Studies have demonstrated that the diameter of the precursor fibers

can be tuned by adjusting the concentration of the metal precursor. For instance, a study by Paulo V. Morais et al. [158] involved the fabrication of ultra-thin WO_3 NFs through electrospinning and calcination of PVP and tungsten salt. Characterization via X-ray diffraction (XRD) and scanning electron microscopy (SEM) revealed smooth fiber surfaces and continuous structures post-calcination (see Figure 10a,b). Additionally, these WO_3 NFs exhibited exceptional selectivity for NO_2 gas in sensing applications (Figure 10c).

Electrospun WO_3 nanostructures hold promise for various applications, including gas sensors, energy storage devices, electrochromic devices, and catalysis. However, several challenges need to be addressed to maximize their potential:

1. Morphology Control

Challenge: Achieving uniform and controllable morphologies, such as nanofibers or nanowires.

Solution: Optimize electrospinning parameters, including solution concentration, solvent properties, applied voltage, and distance between the needle and collector.

2. Crystallinity and Purity

Challenge: Ensuring high crystallinity and purity for optimal functionality.
Solution: Control the calcination process, precursor materials, and annealing conditions.

3. Size and Distribution Control

Challenge: Maintaining a narrow size distribution and specific size range.
Solution: Adjust electrospinning parameters such as solution viscosity and flow rate.

4. Material Degradation

Challenge: Preventing chemical or thermal degradation during the electrospinning process.

Solution: Select appropriate precursor materials and solvents, and optimize electrospinning conditions.

5. Reproducibility and Scalability

Challenge: Ensuring consistent and reproducible results on a large scale.

Solution: Develop standardized protocols, conduct thorough characterization, and scale up processes while maintaining control over parameters.

6. Device Integration

Challenge: Integrating nanostructures into devices while preserving their properties.

Solution: Foster collaboration between materials scientists and device engineers to optimize integration and performance.

7. Stability and Durability

Challenge: Ensuring long-term stability and durability under operational conditions.
Solution: Investigate degradation mechanisms and perform accelerated aging tests.

8. Toxicity and Environmental Impact

Challenge: Addressing concerns about the toxicity and environmental impact of solvents and chemicals.

Solution: Explore environmentally friendly solvents and sustainable synthesis routes.

In summary, electrospun WO_3 nanostructures offer exciting opportunities, but overcoming challenges related to morphology control, crystallinity, size distribution, reproducibility, stability, and environmental impact is crucial for their practical application.

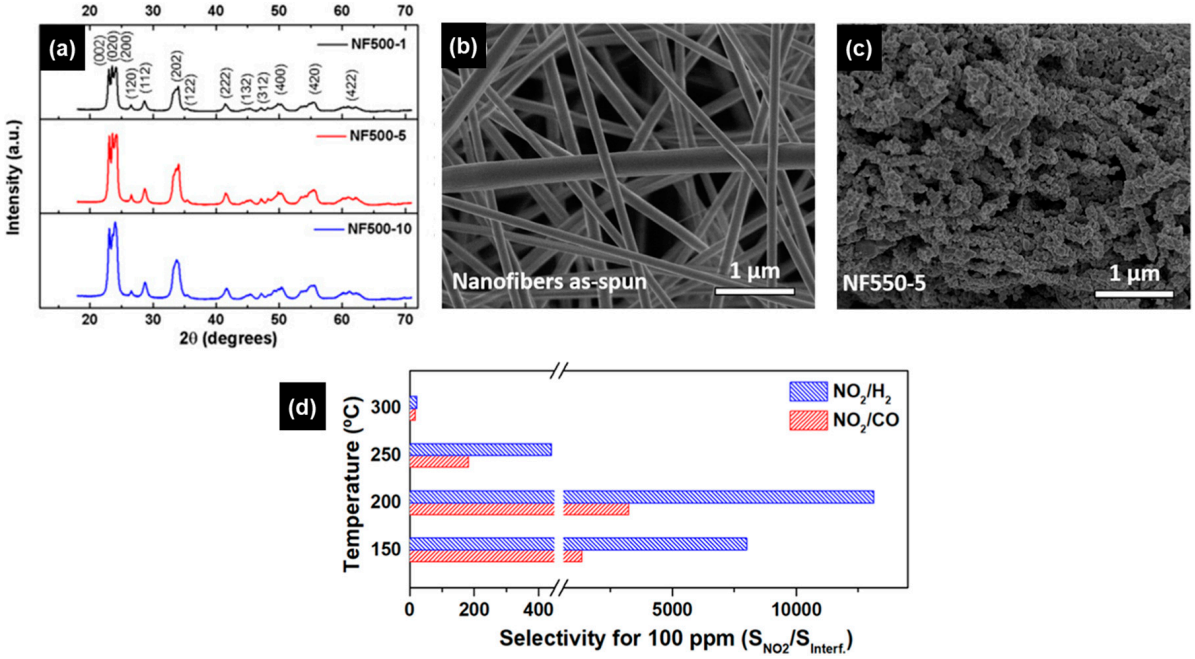

Figure 10. (**a**) XRD spectra of the WO_3 NFs calcined at different heating rates SEM images of the (**b**) as-prepared nanofibers before the calcination and (**c**) calcined NF550 with heating rates (5 °C/min). (**d**) Relative selectivity for 100 ppm of NO_2, H_2, and CO. Reprinted with permission from Reference [158].

2.5. Microwave Method

In general, the method involves applying microwaves (λ = 1–100 cm electromagnetic radiation) to heat a solution. Microwave radiation excites and aligns the dipoles of the material, resulting in ultra-fast, homogeneous, and selective heating that is not achievable with conventional methods. This homogeneous heating enhances the controllability and reproducibility of the synthesis. In addition to saving energy and time, microwave-assisted synthesis offers advantages such as higher yields, rapid and uniform nucleation, and increased reaction rates [159,160].

Despite these advantages, challenges such as overheating due to particle heat generation and the concentration of thermal energy at particle interfaces pose significant issues in microwave-assisted synthesis. While localized heating or hot spots can accelerate nanoparticle growth, excessive overheating may lead to aggregation and structural degradation through sintering or melting. Additionally, in heterogeneous systems, different components interact variably with electromagnetic fields, causing temperature gradients that can alter reaction rates and products [160,161].

Efforts have been made to address these challenges, and various nanostructures have been successfully produced using microwave-assisted methods.

This method has been employed to synthesize a range of materials. For example, Lemos et al. [162] synthesized Ni- and Fe-doped ZnO using a household microwave. Manikandan et al. [163] grew Zr-FeOOH and Zr-$ZnFe_3O_4$ through successive microwave and wet impregnation processes. Ju and co-workers [164] produced $ZnFe_2O_4$ via a microwave-assisted combustion method. Etminan and Sadrnezhaad synthesized $MiMgAl_2O_4$ by combining microwave and combustion processes. Xiongjin et al. [165] achieved metallic Sb through the direct microwave carbothermal reduction of Sb_2O_3 concentrate. The following sections will focus on the main WO_3 morphologies obtained from microwave-mediated syntheses.

2.5.1. Nanoparticles

WO_3 nanoparticles synthesized using microwave methods are valued for their low cost, ease of operation, and the ability to produce monodisperse nanoparticles.

Kowsalya et al. [166] produced WO_3 nanoparticles through a two-step synthesis process. First, 2.49 g of tungstic acid was dissolved in 10 mL of NaOH solution and stirred for 30 min, forming a STH solution. The pH of the solution was then adjusted to 1 by adding HCl, after which it was subjected to microwave irradiation at 240 W for 7 min. Post microwave treatment, the material was centrifuged several times at 5000 rpm with distilled water and ethanol. The sample was subsequently dried at 60 °C for 12 h and annealed at 500 °C for 5 h to obtain monoclinic WO_3. A CTAB-mediated synthesis was also performed using a similar process. In this route, 0.5 g of CTAB was added after the formation of STH and stirred for 30 min. The pure and CTAB-mediated syntheses produced monoclinic WO_3 with heterogeneous and homogeneous nanoparticle forms, respectively. The WO_3 sample obtained with CTAB had a larger size, greater surface area, and smaller bandgap. The reduced bandgap improves the charge transfer, specific capacitance, and energy density, making CTAB-treated WO_3 promising for pseudocapacitance applications.

Aliasghari et al. [92] synthesized monoclinic WO_3 nanoparticles using microwave-assisted solution combustion synthesis. Initially, 4.0 g of tungsten powder was dissolved in a certain amount of hydrogen peroxide, then 9.0 mL of nitric acid and 7.5 g of glycine were added to the solution. After heating the solution on a hotplate at 80 °C, the resulting viscous gel was transferred to a microwave oven (rotating sample at 900 W) to complete the combustion in 60 s. The synthesis yielded spherical particles with a navy-blue color and an average size of 300 nm. UV measurements indicated a bandgap of 3.5 eV, which is 1 eV higher than the bulk WO_3 bandgap.

Other studies have reported the microwave-assisted synthesis of WO_3 nanoparticles using hydrothermal [167], solvothermal [168], and evaporation [169] methods.

2.5.2. Nanowires

Xiao and co-workers [170] developed a WO_3/rGO composite using WCl_6 and graphene oxide (GO) as precursors (Figure 11). Initially, 85 mg of WCl_6 and 10 mg of GO were dissolved in 60 mL of absolute ethanol in a quartz tube. After 20 min of ultrasonication, the tube was placed in a microwave reactor under an Ar atmosphere with the pressure set to 35 bar. The reactor was heated to 200 °C and maintained at this temperature for 30 min. The system was then cooled to room temperature, and the mixture was washed with ethanol three times. Finally, the sample was dried under vacuum at 30 °C. Microwave irradiation induces super hot spots on the GO surfaces in the liquid phase, which ensures localized crystallization of WO_3 and promotes the growth of nanowires. The authors also synthesized WO_{3-x}/rGO by subjecting the initial composite to varying times of microwave exposure. The WO_3/rGO composite was placed in the center of a quartz flask, sealed with a vacuum pump, and irradiated with microwaves (2.45 GHz, 800 W). The defect ratio was controlled by varying the microwave exposure time (5 s, 10 s, 20 s, 30 s, and 40 s). The best results were observed with 20 s of exposure, yielding nanowires with a rough surface and porous structure. Prolonged microwave heating led to crystal aggregation and pore cracking. The photocatalytic efficiency of WO_3/rGO, in combination with a Fenton reagent (H_2O_2 + $FeSO_4$), demonstrated a good performance in degrading Bisphenol A (BPA). Other studies have also shown that WO_3 nanowires synthesized via microwave-assisted methods exhibit a strong photocatalytic and photoelectrochemical performance [171].

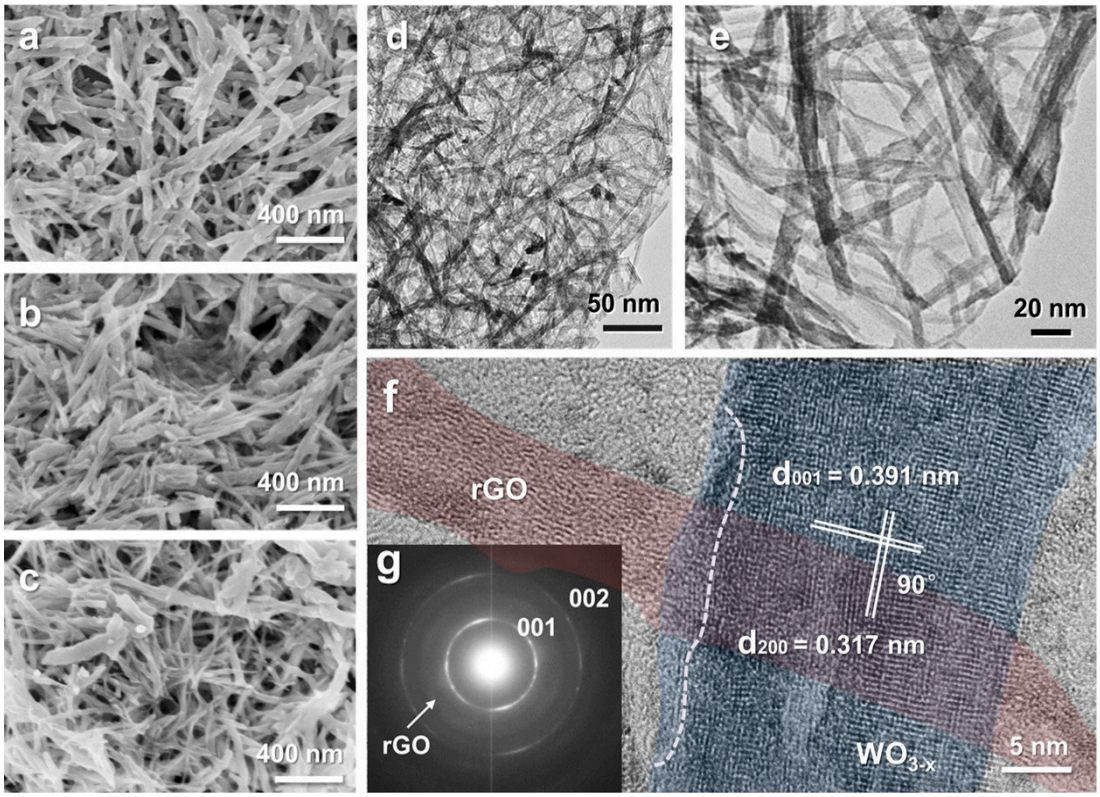

Figure 11. (**a**–**c**) SEM images of WO_3, WO_3/rGO and WO_{3-x}/rGO, respectively. (**d**,**e**) TEM images, (**f**) HRTEM image, and (**g**) SAED pattern of WO_{3-x}/rGO sample. Reprinted with permission from Reference [170]. Copyright 2020 ACS.

2.5.3. Nanorods

WO_3 nanorods are recognized for their excellent photocatalytic properties. The synthesis of this morphology using microwave methods offers significant time and cost advantages.

Periasamy et al. [172] synthesized WO_3 nanorods using a straightforward microwave route with a household microwave. Initially, a 0.1 M Na_2WO_4 solution was prepared, and the pH was adjusted to 1–2 by adding 6 mL of HCl dropwise, followed by stirring for 1 h. During this process, the solution changed color from colorless to pale yellow. After settling, the slurry was subjected to microwave irradiation for three different durations (10 min, 20 min, and 30 min). The resulting samples comprised nanorods with a combination of monoclinic $WO_{2.90}$ and orthorhombic β-WO_3 crystal structures. Electrochemical investigations revealed a decrease in capacitance with increased microwave irradiation time, attributed to the growth of nanorod size. The best capacitance was observed in the sample irradiated for 10 min (44 Fg^{-1} at 0.5 Ag^{-1}), indicating its potential as a promising electrode material for supercapacitor applications.

Ryu and Nam [173] employed a microwave-assisted hydrothermal method (MH) to synthesize WO_3 nanorods. In this procedure, 0.2 M citric acid was dissolved in a 1.0 M Na_2WO_4 aqueous solution, and the pH was adjusted to 2.0 by adding HCl. After stirring for 1 h, the solution was irradiated with microwaves (200 W) for 5 min in a CEM Discover LabMate. The MH process was carried out at three different temperatures (150 °C, 180 °C, and 210 °C) with mild stirring. The product was allowed to cool naturally to room temperature, washed three times with deionized water and ethanol, and dried at 60 °C for 12 h. The nanostructures WO_3 nanorods were found to exhibit a hexagonal phase, with sizes ranging between 80 nm and 600 nm, depending on the synthesis temperature. At 150 °C, the length of the nanorods was approximately 80–150 nm, while longer rod bundles were observed at higher temperatures. The sample was evaluated for MB degradation,

with the best results observed for WO_3 synthesized at 150 °C due to its higher surface area (52.05 m^2g^{-1}).

2.5.4. Nanoplates

WO_3 nanoplates are excellent materials for photocatalytic and sensor applications. However, many synthesis routes often require post-synthesis processes that can increase the size and alter the morphology of the nanoplates. To address this issue, McDonald and Bartlett [174] synthesized WO_3 nanoplates using a single-step microwave method. In their approach, 0.5 mmol of tungsten hexachloride was dissolved in 10 mL of stirring benzyl alcohol. The solution was prepared in a microwave glass vial within an N_2-filled glovebox. The mixture initially produced a red solution that turned blue with continued stirring. The vessel was then sealed and removed from the glovebox. The solution was heated at 200 °C in a microwave reactor while stirring. After 30 min, the solution was quenched with a compressed air gun and allowed to cool to room temperature. The precipitate was collected by centrifugation, washed twice with ethanol and chloroform, and dried in a vacuum at 60 °C overnight. Morphological and structural characterization revealed that the samples consisted of monoclinic WO_3 nanoplates with an average size of 20 nm and a thickness of 5–10 nm, exhibiting high photocatalytic activity for the oxidation of benzyl alcohol.

Tu et al. [175] employed a microwave intercalation synthesis to produce WO_3 nanoplates. In their method, a $Bi_2H_2O_9$ precursor was added to 400 mL of 6M HCl, and the solution was heated in a microwave oven for 30 min. This process generated an intermediate product, $H_2W_2O_7$, which was then calcined at 700 °C to obtain monoclinic WO_3 nanoplates. The nanoplates-based NO sensor demonstrated a high sensitivity to NOx at elevated temperatures.

2.5.5. Nanoflowers

WO_3 nanoflowers can be created by assembling various structures such as nanorods, nanowires, and nanoplates.

Gui and co-workers [176] developed a WO_3 nanoflower using a microwave-assisted gas–liquid interface method. They dissolved 1.49 g of Na_2WO_4:$2H_2O$ in a 40 mL solution of deionized water and ethylene glycol under vigorous stirring for 20 min. This solution was then transferred to a Teflon-lined autoclave with 15 mL of HCl, heated to 120 °C via microwave, and maintained at this temperature for 60 min. After centrifugation and washing with deionized water and ethanol, the sample was dried at 100 °C for 8 h. The dried powder was calcined at 550 °C for 2 h, resulting in nanosheet-assembled nanoflowers with a thickness of approximately 85 nm. These nanoflowers showed a good performance in detecting triethylamine (TEA) at room temperature, and also demonstrated effectiveness for detecting NO_2 and acetone [177].

Nunes et al. [178] synthesized WO_3 nanoflower films on an FTO substrate for solar catalysis applications. They first covered the FTO with a WO_3 seed layer through a seeding process. To grow the flower-like structures, they dissolved 0.829 g of Na_2WO_4 in 20 mL of deionized water, added 5 mL of HCl, stirred for 5 min, and then added 0.5 g of oxalic acid, stirring for an additional 30 min. After adding 0.3 g of NaCl and stirring for another 5 min, the solution was transferred to a Pyrex vessel, with the FTO substrate placed inside for the microwave process. WO_3 nanoflowers formed at 150 °C and 180 °C displayed flower-like structures assembled from nanoplates and nanorods, respectively.

2.6. Hydrothermal/Solvothermal

Crystal growth processes via hydrothermal and solvothermal routes are widely used in the production of nanostructures with controlled morphology and high crystallinity, with both being conducted in sealed environments under high-temperature and high-pressure conditions. The main difference between these techniques lies in the type of solvent used: hydrothermal synthesis employs water as the solvent, while solvothermal synthesis uses organic solvents [179]. Both approaches offer flexibility in synthesizing

various nanostructured materials, allowing the modulation of parameters such as reagent concentration, temperature, pressure, and reaction time, which results in a wide range of structures.

These synthesis methods are highly regarded crystal growth techniques, known for their ability to produce a variety of nanostructures such as nanorods, nanosheets, nanotubes, nanoneedles, nanoparticles, microspheres, nanoflowers, and nanobelts [180–195]. They are widely used for the production of metal oxides, including MnO_2, SnO, Fe_2O_3, TiO_2, Co_3O_4, ZnO, and WO_3 [167,196–201], as well as heterostructures such as ZnO/CQDs/AgNPs, SnO2/α-Fe_2O_3, α-Fe_2O_3/ZnTe, CuO/ZnO, and MoS2/$Ni_2V_3O_8$ [202–206].

In this method, a chemical reaction occurs within a sealed environment where high temperatures and pressures are applied, allowing the solvent to remain in a liquid state even above its boiling point, thus increasing the solubility of the precursor [207]. The main advantages include its one-step synthesis process, cost-effectiveness, low contamination risk, and flexibility in adjusting synthesis parameters (solvent, reagent concentration, reaction time, pressure, temperature, and pH), as well as its suitability for large-scale production [208]. However, a disadvantage is that, for some compounds, the process can take several days to complete [167]. Nonetheless, due to its simplicity and efficiency, hydrothermal synthesis continues to be preferred for producing materials such as WO_3.

Solvothermal synthesis also involves the growth of nanostructures in a sealed environment under high-temperature conditions, but unlike the hydrothermal method, it employs organic solvents such as methanol, ethanol, and toluene [209]. Although the use of non-aqueous solvents makes the process less eco-friendly due to the toxicity of the precursors, which raises environmental concerns [210,211], solvothermal synthesis is known for producing highly crystalline structures that generally do not require post-annealing treatment.

2.6.1. Nanowires

Both hydrothermal and solvothermal methods are highly effective techniques for the synthesis of WO_3 nanowires, offering distinct advantages and differences based on the reagents, solvents, and conditions used.

In the hydrothermal route, WO_3 nanowires are synthesized using water as the solvent under high-temperature and high-pressure conditions. This technique is known for producing nanostructures with various phases, such as monoclinic, hexagonal, and cubic WO_3. Typical precursors include tungstic acid and sodium tungstate, with acids like oxalic acid, citric acid, or HCl acting as initiators. Common solvents include deionized water, hydrogen peroxide, and ethanol. Control over parameters such as the pH, precursor concentration, temperature, and reaction time is crucial for achieving the desired morphologies and optimizing material performance. For instance, Liu et al. [212] obtained hexagonal WO_3 nanowires with excellent NO_2 sensing properties by tuning the concentration of thiourea in the precursor solution. Similarly, WO_3 nanowires combined with reduced graphene oxide (rGO) have been developed for gas-sensing applications, such as NH_3 monitoring [213], and studies have shown that the concentration of the tungsten precursor directly influences the nanowire morphology (Figure 12) and sensor performance [214].

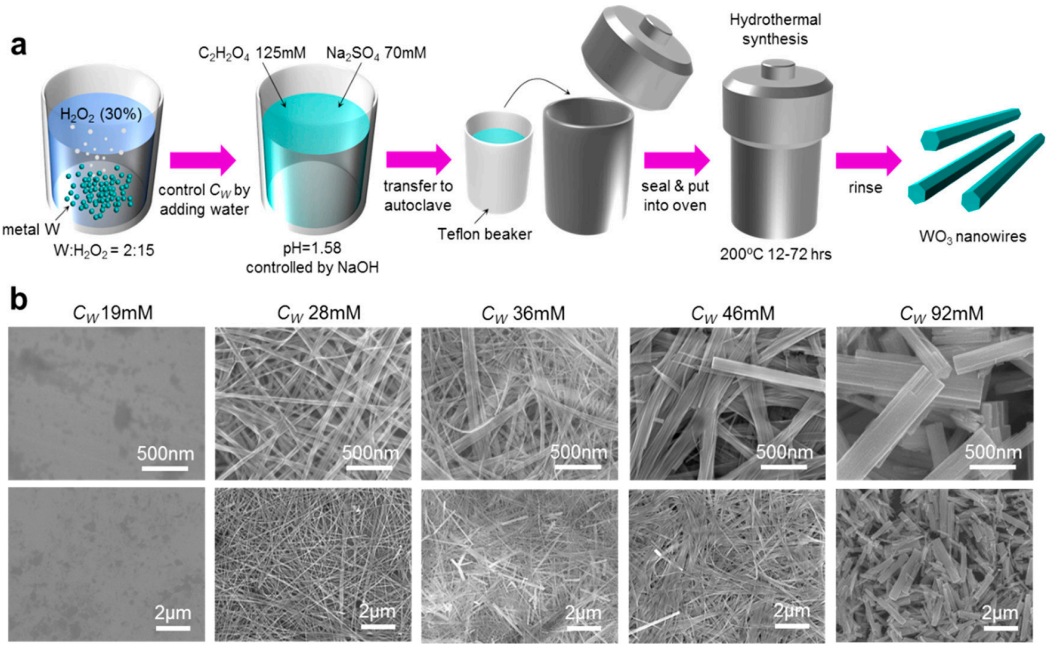

Figure 12. (**a**) Schematic diagram of WO_3 nanowire synthesis processing. (**b**) SEM images of WO_3 nanowires synthesized with different C_W with different magnifications. Reprinted with permission from Reference [214]. Copyright 2020 ACS.

On the other hand, the solvothermal method employs organic solvents, such as methanol or ethanol, in a similar high-temperature and high-pressure environment. This method allows for the growth of WO_3 nanowires with well-defined diameters and lengths, often without the need for post-synthesis annealing. For example, Tang et al. [215] synthesized crystalline WO_3 nanowires using a combination of solvothermal synthesis and RF magnetron sputtering, resulting in nanowires with diameters ranging from 33 nm to 71 nm (Figure 13) and excellent electrochromic properties including high transmittance modulation and good cycling stability in a 1.0 M $LiClO_4$/PC (propylene carbonate) solution. The combination of WO_3 with an amorphous layer further enhanced the nanowires performance in electrochromic applications, as seen in their high transmittance modulation and cycling stability [216,217]. Solvothermal-synthesized nanowires have also demonstrated superior photocurrent densities compared to nanoplates, showing enhanced photoelectrochemical activity due to their increased surface area [218].

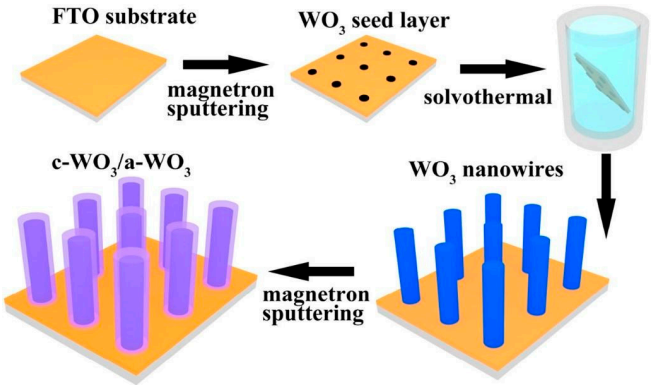

Figure 13. Illustration of the growth of WO_3 nanowires by the solvothermal method. Reprinted with permission from Reference [215]. Copyright 2019 Elsevier.

2.6.2. Nanorods

The synthesis of WO_3 nanorods via hydrothermal and solvothermal methods offers distinct advantages and yields materials with promising applications in fields such as gas sensing and photocatalysis. Both methods are efficient in controlling morphology, phase composition, and enhancing the material's performance in various applications.

In hydrothermal synthesis, Yao et al. [219] used sodium sulfate and oxalic acid to produce hexagonal WO_3 nanorods with an average diameter of 60 nm. These nanorods exhibited excellent photocatalytic degradation of organic dyes and high specific capacitance in supercapacitor applications. Lu et al. [220] further demonstrated that varying the concentration of sodium sulfate during synthesis could control the morphology of WO_3 nanorods, influencing their gas-sensing properties. Specifically, nanorod bundles produced with higher concentrations of sodium sulfate showed an enhanced sensitivity to formic acid due to the increased surface area and active sites provided by their structure. Similarly, Van Tong et al. [221] synthesized monoclinic WO_3 nanorods (~160 nm) and enhanced their gas-detection capability by decorating them with palladium (Pd) nanoparticles, increasing the sensor response by up to 24% when Pd concentration was optimized.

On the other hand, solvothermal methods have also been widely used for WO_3 nanorods' synthesis, often incorporating surfactants to control structure. Mohamed et al. [222] employed a dual surfactant-assisted solvothermal route, using polyvinyl alcohol (PVA) and Pluronic F-127 to prevent agglomeration and promote mesoporosity. The resulting WO_3 nanorods, further modified with nickel sulfide (NiS), demonstrated an improved photocatalytic oxidation performance. The 9% NiS/WO_3 composite, for instance, achieved a photocatalytic oxidation rate of 1.38 μmol min^{-1} and maintained stability over five cycles.

Both methods, however, demonstrate versatility in adapting WO_3 nanorods for various sensing and catalytic applications. Studies also highlight the use of WO_3 nanorods synthesized hydrothermally for sensing ethanol [223], NH_3 [224], and triethylamine [225], as well as for dye photodegradation [226,227], showcasing the broad applicability of WO_3 nanostructures across different fields.

2.6.3. Nanosheets

The synthesis of WO_3 nanosheets via the hydrothermal route has gained popularity in recent years due to the method's simplicity and efficiency. These nanosheets offer numerous advantages due to their large surface area, making them particularly useful in gas-detection applications.

Wang et al. [228] reported the synthesis of WO_3 nanosheets using a solution containing 0.1 g of P123 surfactant dissolved in 13 g of ethanol and 0.45 g of water. After stirring for 15 min, 0.4 g of tungsten hexachloride (WCl_6) was added. The solution was stirred for an additional 10 min and then transferred to an autoclave, where it was heated at 150 °C for 4 h. The resulting WO_3 nanosheets were obtained after washing, drying for 5 to 10 h, and annealing at 300 °C for 3 h. Field emission scanning electron microscopy (FESEM) images revealed that the nanosheets had lengths and widths of approximately 100 nm and thicknesses of about 10 nm. X-ray diffraction (XRD) confirmed the monoclinic phase of WO_3 with high crystallinity. These nanosheets demonstrated the highest response to 50 ppb NO_2 compared to other gases (ethanol, CO, H_2, and NH_3 at 100 ppm) with a recovery time of around 75 s.

Song et al. [229] synthesized monoclinic (M-WO_3), triclinic (T-WO_3), and hexagonal (H-WO_3) WO_3 nanosheets through a hydrothermal route using the treatment temperature and precursors as adjust parameters. Structural analysis showed thicknesses of around 30–40 nm for M-WO_3 and T-WO_3, and 50–60 nm for H-WO_3 with NO_2 detection depends on the WO_3 phase. Similarly, Owen et al. [230] found that hexagonal WO_3 nanoplatelets obtained by the hydrothermal route have good activity in detecting gases such as acetone and isoprene.

Ji et al. [231] investigated NH_3 sensing using WO_3 nanosheets arranged in flower-like structures with both loose (WO_3L) and tight arrangements (WO_3T). SEM images (Figure 14)

indicated that both samples had flower-like morphologies with sizes around 3 µm, with nanosheets having an average thickness of 10–15 nm for WO_3L and 25–50 nm for WO_3T. Both samples were tested as NH_3 gas sensors, with WO_3L showing a 40% higher response compared to WO_3T due to its loose distribution, which provides a larger surface area. Other studies have also explored WO_3 nanosheets for sensing gases such as NO_2 [232], xylene [233], BTEX vapors [234], and C_2H_2 [235].

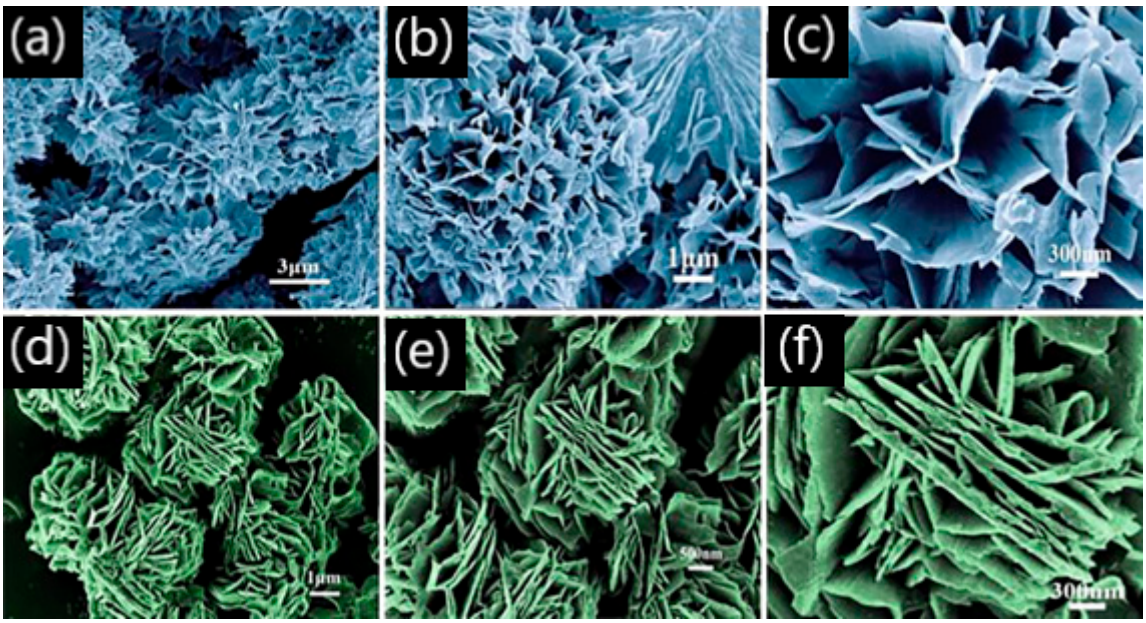

Figure 14. SEM image of WO_3 nanosheets with loosely (**a**–**c**) and tightly (**d**–**f**) arranged. The image was artificially colored to differentiate between the loosely and tightly arranged nanosheets. Reprinted with permission from Reference [231]. Copyright 2019 Elsevier.

In contrast, solvothermal methods offer an alternative approach to synthesize WO_3 nanosheets with distinct properties. For instance, Yang et al. [236] synthesized WO_{3-x} nanosheets using a solvothermal method, starting with $WO_3 \cdot 0.33H_2O$ and adding acetic acid to ethanol. The resulting WO_{3-x} nanosheets exhibited excellent photocatalytic activity under visible light, with high ammonia generation rates due to oxygen vacancies (OVs) introduced during the synthesis. These OVs served as active sites for chemisorption, facilitating the photocatalytic nitrogen fixation process. This method demonstrates how solvothermal synthesis can be tailored to improve photocatalytic applications by introducing non-stoichiometry and oxygen vacancies.

2.6.4. Nanotubes

The synthesis of WO_3 nanotubes using the hydrothermal method is relatively new, with only a few papers reporting this technique. The first successful synthesis of WO_3 nanotubes without the aid of additional sources was reported by Zeb et al. [13]. For their synthesis, 1.65 g of STD was dissolved in 40 mL of deionized water (DW). The solution's pH was adjusted to 1.5 with HCl while stirring. Fractions of potassium sulfate (K_2SO_4) ranging from 2.5 to 20 mmol and either citric acid or oxalic acid ranging from 1.25 to 5 mmol were added as surface directing agents. The mixture was then transferred to an autoclave and heated at 180 °C for 24 h. Afterward, the samples were washed with ethanol and water and dried at 60 °C. The resulting WO_3 nanotubes exhibited ultrafine walls with a thickness of 2 nm and a diameter of approximately 10–15 nm, showing a hexagonal phase with high crystallinity. The nanotubes demonstrated excellent sensitivity to ethanol and acetone due to their high surface area, porosity, and tunnel structure.

Similarly, Wu et al. [237] synthesized WO_3 nanotubes using carbon cloth (CC) as a substrate. X-ray diffraction (XRD) results indicated that the WO_3 had a hexagonal phase with

preferential growth directions along (001) and (200), and good crystallinity. Transmission electron microscopy images revealed the formation of nanotube bundles. These samples were tested as supercapacitor electrodes, showing high capacitance, excellent cycling stability, and high reversible capacity for Li-ion batteries. This outstanding performance was attributed to the tunnel structure of the nanotubes.

In a solvothermal approach, Song et al. [238] synthesized WO_3 using WCl_6 and urea dissolved in ethanol, followed by heating at 180 °C for 12 h. After centrifugation, the precipitate was dried and calcined at 450 °C for 3 h. The resulting WO_3 exhibited a similar hexagonal phase and showed an excellent response to ethanol when tested as a sensor. The response to ethanol increased with temperature, reaching a peak at 340 °C, after which the response declined, indicating a dynamic equilibrium between adsorption and desorption. The sensor demonstrated ultra-fast response times (1 s for 100–500 ppm ethanol) and recovery times between 9 and 19 s, outperforming previous WO_3 sensors. Its selectivity for ethanol was notably higher than that for other gases such as methanol, benzene, and hexane.

2.6.5. Nanoflowers

The synthesis of nanoflowers has gained popularity in recent years due to their high surface area, which enhances charge transfer and broadens their technological applications [239]. Bhosale et al. [240] reported the growth of monoclinic and hexagonal WO_3 nanoflowers on an indium tin oxide (ITO) substrate. They used an aqueous solution of $Na_2WO_4{\cdot}2H_2O$ as the precursor, added HCl dropwise to adjust the pH, and incorporated oxalic acid into the solution, which was stirred for 15 min. This solution, along with the ITO substrates, was placed in an autoclave at 100 °C for 1 h. The resulting material was then calcined at 400 °C for 2 h to obtain WO_3 nanoflowers. These nanostructures demonstrated excellent performance in energy-saving applications due to their rapid charge transfer and high electrochromic stability.

Fang et al. [241] synthesized hexagonal WO_3 nanoflowers for gas sensing. The nanoflowers, self-assembled from nanorods with a thickness of around 14–20 nm, showed excellent sensitivity as NO_x gas sensors, with a response time of 4.5 s to 97 ppm NO_x at room temperature. The flower-like structure facilitated easier gas diffusion between the sheets.

Wei et al. [235] synthesized high crystalline WO_3 nanoflowers via a hydrothermal route, which were used for acetylene (C_2H_2) gas detection, demonstrating a response time of 12 s and a recovery time of 17 s for 200 ppm C_2H_2 at 275 °C. This performance was attributed to the additional active sites provided by their high surface area. WO_3 nanoflowers have also been successfully applied in sensing other gases such as aniline [242], NO_2 [41], and xylene [243], as well as in photoelectrochemical [244] and photocatalytic applications [245].

In addition, Dutta et al. [246] introduced a novel application for WO_3 nanoflowers by incorporating them into polymer nanocomposites through a chemical oxidative polymerization reaction. The WO_3 nanoflowers were synthesized via solvothermal reaction using tungsten hexachloride in methanol at 180 °C, forming nanocomposites with different WO_3 concentrations. The results showed that the nanocomposite with 15% WO_3 (PW 15) exhibited superior capacitive performance, with a specific capacitance of 133.16 F/g and 74% capacitance retention after 5000 cycles. An asymmetric supercapacitor was developed using this material, showing an capacitance per unit area of 730 $\mu F/cm^2$, energy density of 370 mWh/kg, and a color change from blue to transparent green, indicating the charge level of the device. This advancement positions the PMOANI-WO_3 nanocomposite as a promising candidate for multifunctional supercapacitors with an additional color-indicating feature.

2.6.6. Nanoparticles

In the hydrothermal method, Santos et al. [247] dissolved 0.4 g of STD in deionized water containing 0.15 g of NaCl and adjusted the pH using HCl at different concentrations

(2.7 M, 1.5 M, and 0.3 M). The mixture was treated at 180 °C for 2 h, followed by washing and drying. The resulting nanoparticles showed monoclinic and hydrated orthorhombic phases, with different morphologies depending on the HCl concentration used. The nanoparticles synthesized with 1.5 M and 0.3 M HCl exhibited higher conductivity and performance in nitrite biosensors, attributed to the material's morphology. Similarly, Santhosh et al. [248] synthesized WO_3 using a hydrothermal route with WCl_6 and thiourea as precursors. The solution was autoclaved at 245 °C for 18 h, yielding monoclinic nanoparticles around 100 nm in diameter, which showed good visible light absorption and a 62% efficiency in degrading methylene blue dye. These studies demonstrate that controlling the precursor concentration and reaction temperature is crucial in defining the phase and morphology of the nanoparticles, directly impacting their functional properties such as stability and pollutant degradation efficiency.

In comparison, the solvothermal method is also effective in controlling the morphology and phase of WO_3 nanoparticles, offering greater versatility in the use of organic solvents and controlling nanomaterial formation. Jeevitha et al. [249] synthesized WO_3 using WCl_6 and urea in ethanol, treating the solution at 180 °C for 12 h. The resulting material, with an orthorhombic phase and irregular spherical morphology, was tested for ammonia detection, showing a good performance with response and recovery times of 60 and 150 s, respectively. Similarly, Wang et al. [250] varied the concentration of hexamethylenetetramine (HMT) to control the morphology of WO_3 nanoparticles obtained via solvothermal synthesis, achieving structures ranging from flower-like to spherical nanoparticles (Figure 15), with the best performance in toluene detection at high temperatures. This method offers precise control over the formation and growth of the nanoparticles, allowing their properties to be tuned for specific applications.

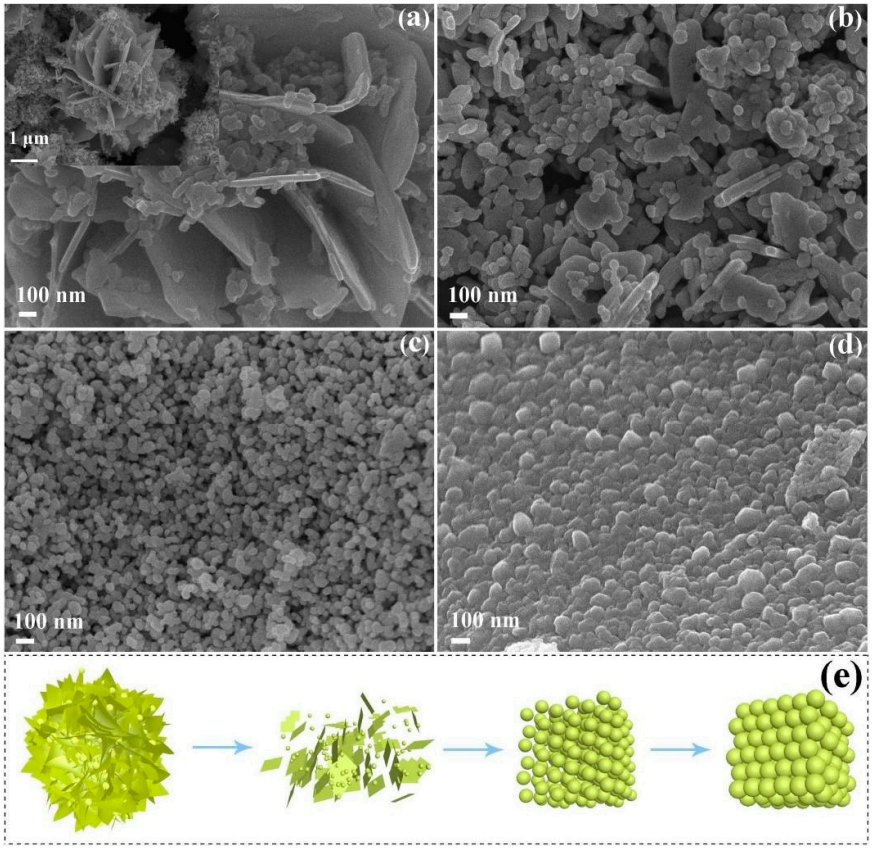

Figure 15. SEM images of HMT_x/WCl_6 with different molar ratios, from 0 to 2, and annealing at 500 °C: (**a**) HMT_0-WO_3, (**b**) $HMT_{0.5}-WO_3$, (**c**) HMT_1-WO_3, and (**d**) HMT_2-WO_3. (**e**) Illustration of the morphology-controlled process. Reprinted with permission from Reference [250]. Copyright 2019 Elsevier.

Both hydrothermal and solvothermal synthesis highlight the importance of parameters such as precursor concentration, reaction time, and temperature in controlling the nanoparticle morphology and phase. In terms of applications, WO_3 nanoparticles obtained through these methods have shown an excellent performance in gas sensors, such as NO_2 [251], toluene [250], and ammonia [249] detection, as well as in photocatalytic pollutant degradation [247,248] and antimicrobial activity [168]. While the hydrothermal method is widely used for its simplicity and energy efficiency, the solvothermal method offers greater versatility in controlling nanoparticle morphological characteristics, favoring the development of nanomaterials with optimized properties for specific applications.

2.6.7. Hollow Microspheres

Hollow microsphere structures synthesized via solvothermal or hydrothermal methods are of significant interest due to their unique morphology, which offers a large surface area and straightforward synthesis, either with or without a template.

Tong et al. [251] utilized the solvothermal route to produce hierarchical monoclinic WO_3 hollow microspheres (~900 nm in diameter) with good crystallinity and a wall thickness of about 200 nm. These microspheres were employed as anode electrodes in a battery, using an electrolyte composed of 1 mol/L LiPF6 in a 1:1 volume mixture of ethylene carbonate (EC) and dimethyl carbonate (DMC). The electrode exhibited a high reversible capacity, excellent capacity retention, and impressive high-rate cycling performance, maintaining 213 $mA{\cdot}h{\cdot}g^{-1}$ after 500 cycles.

Jin et al. [252] also synthesized hollow WO_3 microspheres using a solvothermal method. The WO_3 microspheres, which were decorated with Pd/PdO (with atomic ratios of 0, 1 at%, 2 at%, and 5 at%), were characterized as monoclinic WO_3 microspheres with surfaces consisting of irregular nanosheets. There was no significant morphological change following Pd/PdO deposition. The 2 at% Pd/PdO-WO_3 sample showed an excellent performance in H_2S detection, with a rapid response time of 1 s for 25 ppm H_2S, indicating its high potential for use in gas-detection applications. Additionally, other studies have explored WO_3 microspheres for sensing gases such as NO [253], toluene, and xylene [254].

On the other hand, hydrothermal methods have also been employed to synthesize WO_3 hollow microspheres, often utilizing organic precursors. For instance, Lee et al. [255] synthesized WO_3 microspheres using glucose monohydrate as a carbon precursor and sodium tungstate ($Na_2WO_4{\cdot}2H_2O$) as the tungsten source. The reactants were dissolved in distilled water and transferred to a Teflon-lined autoclave, where they were treated at 200 °C for 24 h. After cooling, the products were washed, dried at 60 °C, and then subjected to thermal decomposition at 450 °C, converting the carbon core into WO_3. The study explored various molar ratios (R) between glucose and $Na_2WO_4{\cdot}2H_2O$, affecting the final morphology of the microspheres. The hydrothermally synthesized WO_3 hollow microspheres exhibited a notable performance in gas detection, particularly for NO_2. As the thermal energy during calcination increased, the hollow microspheres gradually transformed into solid microspheres. Nevertheless, the hollow microspheres consistently demonstrated a higher response to NO_2 detection, with a 2.2 to 2.9-fold improvement compared to the solid structures. This enhanced performance was attributed to their larger surface area, which facilitated more efficient gas diffusion through the porous and thin shells of the hollow microspheres.

2.6.8. Hierarchical Structures

The rapid advancement of new technologies has spurred a continuous quest for innovative materials. Among these, hierarchical structures have gained prominence due to their ability to integrate multiple morphologies, enhancing the performance of devices by combining various properties.

Wang et al. [256] synthesized WO_3 nanorods using a solvothermal method. They dissolved 0.5 mmol of $Na_2WO_4{\cdot}2H_2O$ in varying volumes of ethanol (0, 2, 3, 4, 5, 6, 8, 11, 15, and 17 mL), then added 12 mL of NaCl solution and stirred for 10 min. HCl

was then added until the pH reached 1. The resulting solution was transferred to an autoclave and treated at 100 °C for 4 h. The precipitate was washed with distilled water and ethanol, then dried at 60 °C. The volume of ethanol significantly influenced the phase, crystallinity, and morphology of the nanostructures. With ethanol volumes from 0 to 3 mL, orthorhombic WO_3 flower-like structures with diameters around 4 to 5 µm were formed, showing good crystallinity. For volumes between 4 and 8 mL, hexagonal WO_3 microflowers with high crystallinity and diameters of around 3 µm were observed, along with nanosheets composed of ultrafine nanorods with lengths of 300 nm and thicknesses of 5 to 10 nm. With ethanol volumes up to 11 mL, the formation of hierarchical WO_3 flowers was disrupted, resulting in irregular blocks. The photocatalytic activity was assessed by decolorizing methyl orange (MO), and the WO_3 synthesized with 5 mL of ethanol showed the best performance, decolorizing MO in 30 min.

Wang et al. [257] synthesized WO_3 nanosheets and nanorods using WCl_6, distilled water, and 1-propanol as precursors. Figure 16a shows monoclinic WO_3 nanosheets with sizes ranging from 300 to 1500 nm and a thickness of about 20 nm obtained in the process. Figure 16b displays monoclinic WO_3 nanorods with diameters between 20 and 80 nm in some regions of the sample. Figure 16c,d present TEM and HRTEM images, revealing a lattice spacing of 0.384 nm and a growth plane of (002) for the nanorods. The sensing properties of the WO_3 nanocrystals were evaluated for NO_2 gas using a computer-controlled gas-sensing system. The WO_3 nanorods exhibited a high response time (24 s), recovery time (137 s), and sensitivity to 1 ppm NO_2 gas at 100 °C. Other researchers have also explored WO_3 hierarchical structures for sensing gases such as ethanol [258], chlorine [259], and trimethylamine [260].

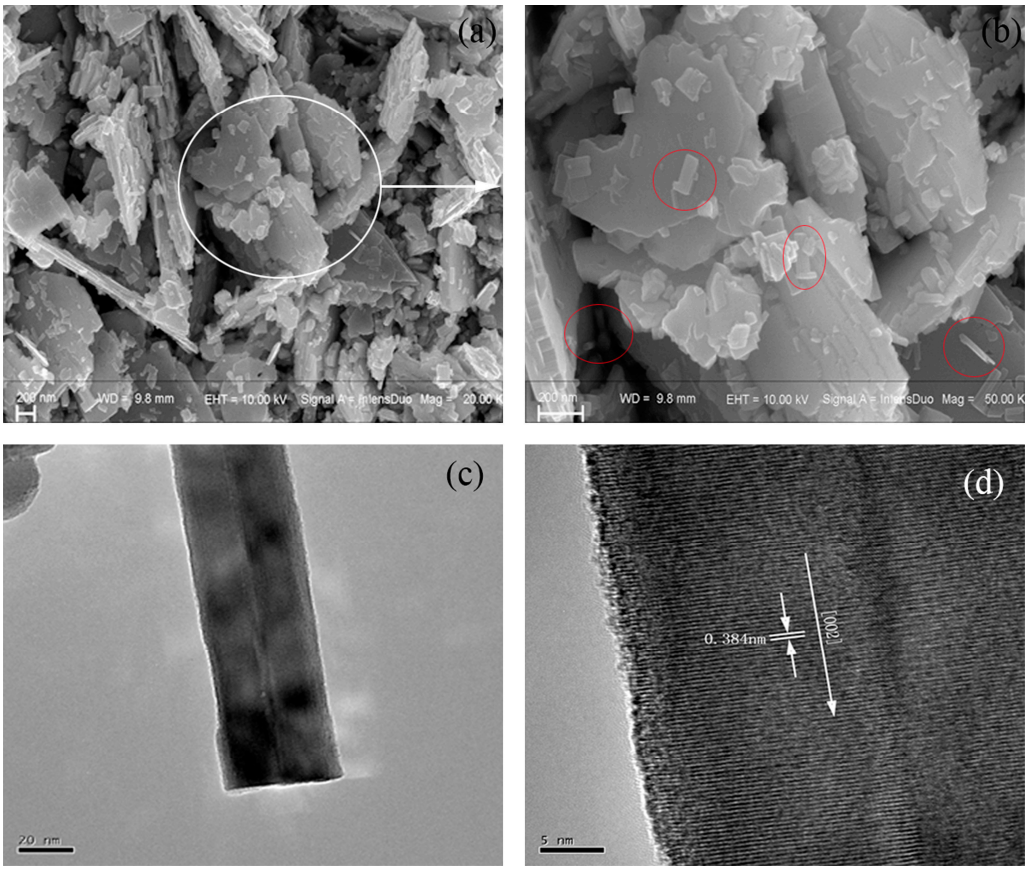

Figure 16. (**a**) SEM images of WO_3 nanosheets, (**b**) enlargement of the white-circled area in (**a**), revealing nanorods dispersed among the nanosheets, circled in red, (**c**) TEM, and (**d**) HARTEM images of WO_3 nanorods. Reprinted with permission from Reference [257]. Copyright 2016 Elsevier.

2.7. Colloidal Synthesis

The colloidal method is widely used in the synthesis of nanomaterials because it allows fine control over the size, shape, and composition of nanoparticles. Advances in colloidal approaches have allowed the synthesis of high-quality monodisperse crystals with various shapes such as spherical, cubic, ellipsoidal, rod-like, need-like, plate, and others. Currently, it has been presented as one of the most promising methods for designing highly complex and stable nanocatalysts [261].

It is one of the oldest methods for the synthesis of metallic nanoparticles, especially gold and silver. Currently, there is a renewed interest in the synthesis of noble metal colloids due to the surface plasmon resonance (SPR) observed in these materials. SPR can also be detected in semiconductor materials such as metal oxides, metal chalcogenides, metal nitrides, and silicon, among others. A comprehensive discussion of the electromagnetic dynamics governing the interaction of light matter in plasmonic semiconductors and their distinct physical properties due to the advances in colloidal synthesis routes is presented in Agrawal et al. [262].

Tungsten oxide is a narrow bandgap semiconductor with well-known (photo)catalytic properties. The synthesis of uniform and stable colloids of WO_3 nanoparticles by this method has enabled the production of increasingly powerful nanocatalysts and contributed to the processing of new nanocomposites. WO_3 nanoparticles with diverse morphologies have been fabricated by both "bottom-up" (chemical routes) and "top-down" (physical approaches) colloidal methods. The "bottom-up" methods are more cost-effective, more reproducible, and allow greater control of morphology when compared to the former [263].

Among the "top-down" approaches, pulsed-laser ablation is one of the most widely employed although electric spark discharge, chemical etching, and mechanical milling methods are also used. In this regard, Salim et al. [264] synthesized colloidal WO_3 nanoparticles using a Q-switched Nd:YAG laser with wavelengths of 1064 nm and 532 nm (repetition rate of 1 Hz; pulse width of 15 ns) and a tungsten target in aqueous medium. Spherical and crystalline nanoparticles were obtained at both wavelengths. The average size of the generated WO_3 nanoparticles decreased from 15 nm to 8 nm and the particle concentration increased when the wavelength was changed from 1064 to 532 nm, indicating that wavelength tuning is an important tool to control these parameters. Fakhari et al. [265] also found that the size, crystallinity, and antibacterial activity of colloidal WO_3 nanoparticle material are also affected by laser fluence (Q-switched Nd:YAG laser with λ = 1064 nm, repetition rate de 2 kHz, pulse width of 220 ns). Higher laser fluence results in the production of larger, more crystalline nanoparticles with greater antibacterial activity under both visible and UV light.

Recently, the synthesis of colloidal Ag@WO_3 core–shell nanostructures from a two-step laser ablation process was reported for the first time [266]. The morphology and structural, electrical, and optical characteristics of the Ag@WO_3 core–shell nanostructures were found to be dependent on the core concentration. Colloidal Pd/WO_3 nanostructures generated by the pulsed-laser ablation method were also reported [267]. The aging of the WO_3 NPs was shown to be fundamental in defining the morphology of the structures; with increasing aging time, the nanostructures change from a core–shell structure to a simple spherical structure. Gasochromic response of the colloids towards hydrogen gas was also shown to be dependent on the material structure. The synthesis of this novel and tailored nanostructure represents an advancement in the use of "top-down" approaches for colloidal materials' synthesis and may provide the development of novel nanostructures with highly flexible shapes and characteristics.

Regarding the "bottom-up" approach, several wet chemistry routes have been employed for the synthesis of colloidal WO_3 nanoparticles. WO_3 nanoparticles [268,269], WO_3-based polymer films [270], Au–SiO_2–WO_3 core–shell composite [271], colloidal WO_{3-x} nanowires [272], and WO_3 nanorods [273], among other structures, have been successfully produced from these routes. Recently, studies have explored the chromic behavior of WO_3 and the surface plasmon resonance properties for the development of composites with

possible theranostic applications. When tuned correctly, materials with this combination of properties can be used for optical imaging, magnetic resonance imaging, ultrasound, computed tomography, and nuclear imaging [274].

Given the similarity of the "bottom-up" colloidal method with others described in this work, we will not discuss the WO_3 morphologies obtained through it one by one; only an overview of the method is presented below.

In general terms, a colloid (or "sol") is a suspension of nanoparticles, typically in the range of 1–1000 nm, in a liquid medium. The size, shape, and surface properties of nanoparticles, as well as the optical properties of the system and particle–solvent and particle–particle interactions determine the nature of the colloid. The intramolecular forces and interfacial free energy of the system determine the stability of the colloid [275].

Traditionally, colloidal nanoparticles are synthesized by the reduction or decomposition of metal precursors (Figure 17). In a typical chemical reduction (Figure 17a), the metal precursor is dissolved in a solvent in the presence of a capping agent, then the temperature is raised and a reducing agent is introduced to initiate the formation of NPs. Thermal decomposition can involve two distinct approaches. In the first, thermal decomposition occurs in a manner similar to reduction except that the process occurs at higher temperatures and no reducing agent is used (Figure 17b). In the second approach, the solvent and precursor agent are initially mixed, after the system is heated, the precursor is then injected into the synthesis vessel (Figure 17c). Cooling the system stops the growth of the NPs.

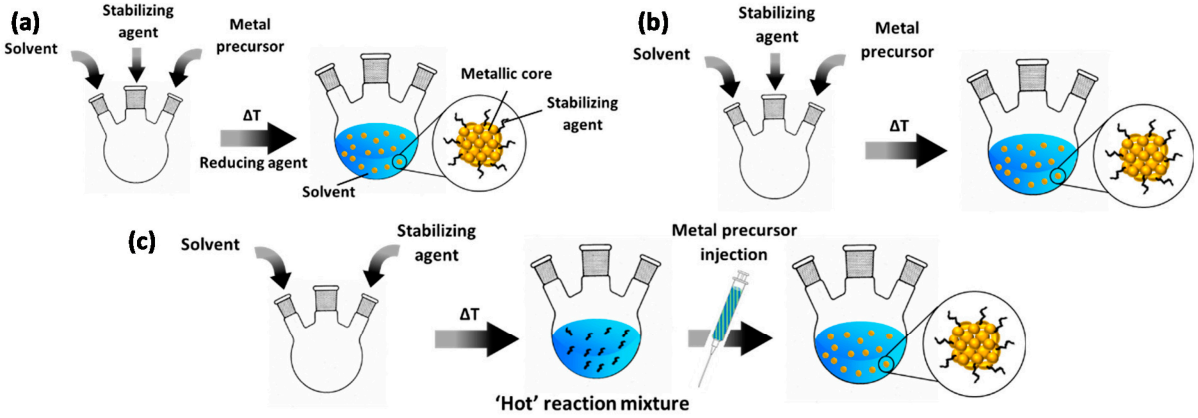

Figure 17. Colloidal synthesis of NPs via (**a**) chemical reduction, (**b**) traditional thermal decomposition, and (**c**) thermal decomposition via hot injection. Reprinted with permission from Reference [276]. Copyright 2020 MDPI.

In both processes, the capping agent plays a key role: it surrounds the colloid cores and limits the diffusion of the precursor from the liquid phase to the core, helping to control the growth of the nanoparticles, and it also acts as a stabilizing agent, preventing the coalescence and agglomeration of the NPs. Furthermore, protective agents can shape the NPs as they can induce growth in a given direction. Surfactants, linear, and dendritic polymers and binders are the most commonly used reagents for this purpose [276]. However, the size, shape, and composition of colloidal NPs is defined by the combination of parameters involved: temperature, time, type of precursor, solvent and capping agent, concentration of reagents, use of extra precursors, among others. This diversity of parameters allows the design of nanostructures with specific and varied characteristics.

Despite recent progress, the colloidal method still has challenges that limit its application area. The synthesis of thin films and heterostructures in solution or at their interfaces, yield, and large-scale production are critical points for the use of this method in some fields. In addition, further studies are still needed to fully understand the surface properties of colloidal nanoparticles as well as the nucleation and growth process in this approach, since these processes have a great impact on the material properties.

3. Conclusions and Future Perspectives

The advancement of nanoscience and nanotechnology has significantly improved the performance of WO_3 morphologies across various applications, including microelectronics, photoelectronics, catalysis, sustainable energy generation, transformation, conversion, storage, and environmental technologies. The core objective driving progress in nanoscience and nanotechnology is the strategic design of nanostructures with specific attributes to meet distinct functionalities.

Currently, a variety of methodologies and techniques are used to engineer WO_3 nanostructures with different dimensions, providing a broad perspective for those interested in nanomaterials (Table 1). However, achieving the desired characteristics in nanomaterials presents considerable challenges. The evolution of new technologies has increased the demand for nanostructures with precisely defined morphologies and sizes, as well as controlled crystallinity, exposed surfaces, multiscale arrangements, and optimized coupling states.

Table 1. Synthesis methods for WO_3 nanostructures and their main characteristics.

Synthesis Method	Advantages	Disadvantages	Promising Applications
Co-precipitation	Simple and rapid preparation; Various possibilities to control the particle size, composition and surface; Low temperature; Scalability;	Not applicable to uncharged species; Possibility of precipitation of trace impurities;	Catalysts; Photodegradation; Gas sensing; Antibacterial activity;
Solution Combustion	Simplicity and low cost; Time- and energy-saving; Well-developed porosity;	Agglomeration; Difficulty in controlling morphology; Potential contamination by combustion residues;	Photocatalytic degradation; Lithium-ion battery; Electrochromic devices;
Sol-gel	In situ construction of heterojunctions; Versatility; In situ doping; Controllable structure, composition and porosity; High surface-to-volume ratio; Consistent reproducibility;	Relatively longer reaction time; Harmful organic solvents; Expensive chemicals;	Supercapacitors; Gas sensors; Photocatalytic applications; Hydrogen sensing; Electrochromic devices; Water purification;
Electrospinning	Simplicity and low cost; High reproducibility; High porosity;	Limited availability of suitable solvents; Toxic solvents; Achieving uniform and controllable morphologies;	Gas sensors; Drug delivery systems; Filtration, adsorption, and sensing applications;
Microwave	Controllability and reproducibility; Time- and energy-saving; High yield; Rapid and uniform nucleation;	Overheating; Expensive equipment; Unsuitable for scale-up; Reaction monitoring is not viable;	Pseudocapacitance applications; Photocatalytic degradation; Gas sensors;
Hydrothermal/Solvothermal	Controllable size, shape, and crystallinity; Thermal and chemical stability;	Expensive autoclaves; Unfeasible reaction monitoring; Toxic solvents (solvothermal);	Gas sensors; Electro(photo)chromic applications; Photocatalysts;
Colloidal	Control over the size, shape, and composition; Production of very small particles	Cost; Yield; Harmful solvents; Oxidation and thermal degradation of ligands	Chromic devices; Theranostic applications

Therefore, developing innovative synthetic strategies and theories is crucial to meet these evolving needs. Efforts should focus on refining existing synthesis methods, advancing current synthetic paradigms, and exploring alternative fabrication processes. These initiatives are expected to significantly enhance the field and contribute to its future growth.

Author Contributions: Conceptualization: O.M.B.; Investigation: O.M.P., R.P.T., H.E.d.S.B., R.A.G., R.S.N., N.J., and O.M.B.; Writing—original draft preparation: O.M.P., R.P.T., H.E.d.S.B., R.A.G., R.S.N., N.J., and O.M.B.; Writing—review and editing: O.M.B. and R.A.G.; Supervision: O.M.B. and R.A.G.; Funding acquisition: O.M.B. All authors have read and agreed to the published version of the manuscript.

Funding: This work was supported by Conselho Nacional de Desenvolvimento Científico e Tecnológico (CNPq) and Coordenação de Aperfeiçoamento de Pessoal de Nível Superior (CAPES)—Finance Code 001.

Data Availability Statement: Data are contained within the article.

Acknowledgments: We are grateful for the valuable discussions and suggestions from Roberto Zenhei Nakazato.

Conflicts of Interest: The authors declare no conflicts of interest.

References

1. Yao, Y.; Sang, D.; Zou, L.; Wang, Q.; Liu, C. A Review on the Properties and Applications of WO_3 Nanostructure−Based Optical and Electronic Devices. *Nanomaterials* **2021**, *11*, 2136. [CrossRef]
2. Lassner, E.; Schubert, W.-D. *Tungsten*; Springer: Boston, MA, USA, 1999; ISBN 978-1-4613-7225-7.
3. Modak, M.; Rane, S.; Jagtap, S. WO_3: A Review of Synthesis Techniques, Nanocomposite Materials and Their Morphological Effects for Gas Sensing Application. *Bull. Mater. Sci.* **2023**, *46*, 28. [CrossRef]
4. Zhang, M.; Yang, C.; Zhang, Z.; Tian, W.; Hui, B.; Zhang, J.; Zhang, K. Tungsten Oxide Polymorphs and Their Multifunctional Applications. *Adv. Colloid. Interface Sci.* **2022**, *300*, 102596. [CrossRef]
5. Lalik, E.; Parker, S.F.; Irvine, G.; da Silva, I.; Gutmann, M.J.; Romanelli, G.; Drużbicki, K.; Kosydar, R.; Krzystyniak, M. Hydrogen Spillover in Tungsten Oxide Bronzes as Observed by Broadband Neutron Spectroscopy. *Energies* **2023**, *16*, 5496. [CrossRef]
6. Shreya; Phogat, P.; Jha, R.; Singh, S. Microwave-Synthesized γ-WO_3 Nanorods Exhibiting High Current Density and Diffusion Characteristics. *Transit. Met. Chem.* **2023**, *48*, 167–183. [CrossRef]
7. Abbaspoor, M.; Aliannezhadi, M.; Tehrani, F.S. Effect of Solution PH on As-Synthesized and Calcined WO_3 Nanoparticles Synthesized Using Sol-Gel Method. *Opt. Mater.* **2021**, *121*, 111552. [CrossRef]
8. Karmakar, R.; Sinha, S.; Das, A.K.; Dey, S.; Dutta, B.; Pramanik, S.; Kuiri, P.K.; Basu, S.; Meikap, A.K. Observation of Synergistic Effects in Multiphase Tungsten Oxide (WO_3) Nanocomposite and Its Role in Enhanced Supercapacitive and Photoluminescence Properties. *Mater. Chem. Phys.* **2023**, *305*, 127915. [CrossRef]
9. Ito, K.; Uchida, R.; Noda, K. Visible Light-Assisted Hydrogen Generation over Platinum-Loaded Tungsten Trioxide Nanorods with the Hexagonal and Triclinic Phases. *J. Photochem. Photobiol. A Chem.* **2023**, *443*, 114824. [CrossRef]
10. Abe, O.O.; Qiu, Z.; Chen, Z.; Jinschek, J.R.; Gouma, P.-I. Effect of Crystallite Size on the Low-Temperature Solid-Solid Phase Transformations in the WO_3 System. *Ceram. Int.* **2021**, *47*, 33476–33482. [CrossRef]
11. Choi, H.J.; Chung, J.-H.; Yoon, J.-W.; Lee, J.-H. Highly Selective, Sensitive, and Rapidly Responding Acetone Sensor Using Ferroelectric ε-WO_3 Spheres Doped with Nb for Monitoring Ketogenic Diet Efficiency. *Sens. Actuators B Chem.* **2021**, *338*, 129823. [CrossRef]
12. Zhang, D.; Liu, R.; Ji, S.; Cai, Y.; Liang, C.; Li, Z. Hierarchical WO_3-x Ultrabroadband Absorbers and Photothermal Converters Grown from Femtosecond Laser-Induced Periodic Surface Structures. *ACS Appl. Mater. Interfaces* **2022**, *14*, 24046–24058. [CrossRef] [PubMed]
13. Zeb, S.; Peng, X.; Yuan, G.; Zhao, X.; Qin, C.; Sun, G.; Nie, Y.; Cui, Y.; Jiang, X. Controllable Synthesis of Ultrathin WO_3 Nanotubes and Nanowires with Excellent Gas Sensing Performance. *Sens. Actuators B Chem.* **2020**, *305*, 127435. [CrossRef]
14. Wang, J.; Liu, Y.; Xi, X.; Nie, Z. Microwave-Assisted Synthesis of Hierarchical $WO_3 \cdot H_2O$ and Its Selective Adsorption: Kinetics, Isotherm and Mechanism. *J. Mater. Sci.* **2022**, *57*, 6881–6899. [CrossRef]
15. Nguyen, H.S.; Luu, T.L.A.; Bui, H.T.; Nguyen, T.T.; Nguyen, H.L.; Nguyen, C.T. Facile Synthesis of in Situ CNT/$WO_3 \cdot H_2O$ Nanoplate Composites for Adsorption and Photocatalytic Applications under Visible Light Irradiation. *Semicond. Sci. Technol.* **2021**, *36*, 095010. [CrossRef]
16. Li, P.; Hao, C.; Wang, H.; He, T.; Shu, T.; Li, C.; Yu, L.; Yan, N. Eco-Friendly Recyclable High Performance Ramie Yarn Reinforced Polyimine Vitrimer Composites. *Chem. Eng. J.* **2023**, *457*, 141341. [CrossRef]
17. Mandlekar, B.K.; Jadhav, A.L.; Jadhav, S.L.; Khan, A.; Kadam, A.V. Binder-Free Room-Temperature Synthesis of Amorphous-WO_3 Thin Film on FTO, ITO, and Stainless Steel by Electrodeposition for Electrochromic Application. *Opt. Mater.* **2023**, *136*, 113460. [CrossRef]
18. Cong, S.; Wang, Z.; Gong, W.; Chen, Z.; Lu, W.; Lombardi, J.R.; Zhao, Z. Electrochromic Semiconductors as Colorimetric SERS Substrates with High Reproducibility and Renewability. *Nat. Commun.* **2019**, *10*, 678. [CrossRef]
19. Thirumalairajan, S.; Girija, K. Tailored Construction of Ag/WO_3 Nanospindles Modified SERS Substrates: An Efficient Analytical Assay for Identification of Neonicotinoids on the Surface of Fruits. *Opt. Mater.* **2022**, *132*, 112861. [CrossRef]

20. Li, J.; Chen, G.; Yan, J.; Huang, B.; Cheng, H.; Lou, Z.; Li, B. Solar-Driven Plasmonic Tungsten Oxides as Catalyst Enhancing Ethanol Dehydration for Highly Selective Ethylene Production. *Appl. Catal. B* **2020**, *264*, 118517. [CrossRef]
21. Tran, V.A.; Nguyen, T.P.; Le, V.T.; Kim, I.T.; Lee, S.-W.; Nguyen, C.T. Excellent Photocatalytic Activity of Ternary Ag@WO_3@rGO Nanocomposites under Solar Simulation Irradiation. *J. Sci. Adv. Mater. Devices* **2021**, *6*, 108–117. [CrossRef]
22. Lv, Q.; Tan, J.; Wang, Z.; Gu, P.; Liu, H.; Yu, L.; Wei, Y.; Gan, L.; Liu, B.; Li, J.; et al. Ultrafast Charge Transfer in Mixed-Dimensional WO_3-x Nanowire/WSe2 Heterostructures for Attomolar-Level Molecular Sensing. *Nat. Commun.* **2023**, *14*, 2717. [CrossRef] [PubMed]
23. Bigham, A.; Raucci, M.G.; Zheng, K.; Boccaccini, A.R.; Ambrosio, L. Oxygen-Deficient Bioceramics: Combination of Diagnosis, Therapy, and Regeneration. *Adv. Mater.* **2023**, *35*, 2302858. [CrossRef] [PubMed]
24. Duong, V.T.; Nguyen, C.T.; Luong, H.B.; Nguyen, D.C.; Nguyen, H.L. Ultralow-Detection Limit Ammonia Gas Sensors at Room Temperature Based on MWCNT/WO_3 Nanocomposite and Effect of Humidity. *Solid State Sci.* **2021**, *113*, 106534. [CrossRef]
25. Esencan Türkaslan, B.; Çelik, A.K.; Dalbeyler, A.; Fantuzzi, N. The Effect of Different Morphologies of WO_3/GO Nanocomposite on Photocatalytic Performance. *Materials* **2022**, *15*, 8019. [CrossRef]
26. Li, Y.-H.; Qi, M.-Y.; Tang, Z.-R.; Xu, Y.-J. Coupling Organic Synthesis and Hydrogen Evolution over Composite WO_3/$ZnIn_2S_4$ Z-Scheme Photocatalyst. *J. Phys. Chem. C* **2022**, *126*, 1872–1880. [CrossRef]
27. Zhao, M.; Liu, S.; Chen, D.; Zhang, S.; Carabineiro, S.A.C.; Lv, K. A Novel S-Scheme 3D $ZnIn_2S_4$/WO_3 Heterostructure for Improved Hydrogen Production under Visible Light Irradiation. *Chin. J. Catal.* **2022**, *43*, 2615–2624. [CrossRef]
28. Roselló-Márquez, G.; García-García, D.M.; Cifre-Herrando, M.; Blasco-Tamarit, E.; García-Antón, J. Facile Preparation of Electrodes Based on WO_3 Nanostructures Modified with C and S Used as Anode Materials for Li-ion Batteries. *J. Am. Ceram. Soc.* **2023**, *106*, 2550–2566. [CrossRef]
29. Parashar, M.; Shukla, V.K.; Singh, R. Metal Oxides Nanoparticles via Sol–Gel Method: A Review on Synthesis, Characterization and Applications. *J. Mater. Sci. Mater. Electron.* **2020**, *31*, 3729–3749. [CrossRef]
30. Dembski, S.; Schneider, C.; Christ, B.; Retter, M. Core-Shell Nanoparticles and Their Use for In Vitro and In Vivo Diagnostics. In *Core-Shell Nanostructures for Drug Delivery and Theranostics*; Elsevier: Amsterdam, The Netherlands, 2018; pp. 119–141.
31. Macías-Martínez, B.I.; Cortés-Hernández, D.A.; Zugasti-Cruz, A.; Cruz-Ortíz, B.R.; Múzquiz-Ramos, E.M. Heating Ability and Hemolysis Test of Magnetite Nanoparticles Obtained by a Simple Co-Precipitation Method. *J. Appl. Res. Technol.* **2016**, *14*, 239–244. [CrossRef]
32. Liu, S.; Ma, C.; Ma, M.-G.; Xu, F. Magnetic Nanocomposite Adsorbents. In *Composite Nanoadsorbents*; Elsevier: Amsterdam, The Netherlands, 2019; pp. 295–316.
33. Khalid, H.; Chaudhry, A.A. Basics of Hydroxyapatite—Structure, Synthesis, Properties, and Clinical Applications. In *Handbook of Ionic Substituted Hydroxyapatites*; Elsevier: Amsterdam, The Netherlands, 2020; pp. 85–115.
34. Rafique, M.S.; Rafique, M.; Tahir, M.B.; Hajra, S.; Nawaz, T.; Shafiq, F. Synthesis Methods of Nanostructures. In *Nanotechnology and Photocatalysis for Environmental Applications*; Elsevier: Amsterdam, The Netherlands, 2020; pp. 45–56.
35. Dong, H.; Koenig, G.M. A Review on Synthesis and Engineering of Crystal Precursors Produced via Coprecipitation for Multicomponent Lithium-Ion Battery Cathode Materials. *CrystEngComm* **2020**, *22*, 1514–1530. [CrossRef]
36. Rane, A.V.; Kanny, K.; Abitha, V.K.; Thomas, S. Methods for Synthesis of Nanoparticles and Fabrication of Nanocomposites. In *Synthesis of Inorganic Nanomaterials*; Elsevier: Amsterdam, The Netherlands, 2018; pp. 121–139.
37. Lok, M. Coprecipitation. In *Synthesis of Solid Catalysts*; Wiley: Hoboken, NJ, USA, 2009; pp. 135–151.
38. Mehmood, F.; Iqbal, J.; Jan, T.; Gul, A.; Mansoor, Q.; Faryal, R. Structural, Photoluminescence, Electrical, Anti Cancer and Visible Light Driven Photocatalytic Characteristics of Co Doped WO_3 Nanoplates. *Vib. Spectrosc.* **2017**, *93*, 78–89. [CrossRef]
39. Mehmood, F.; Iqbal, J.; Jan, T.; Mansoor, Q. Structural, Raman and Photoluminescence Properties of Fe Doped WO_3 Nanoplates with Anti Cancer and Visible Light Driven Photocatalytic Activities. *J. Alloys Compd.* **2017**, *728*, 1329–1337. [CrossRef]
40. Mehmood, F.; Iqbal, J.; Gul, A.; Ahmed, W.; Ismail, M. Facile Synthesis of 2-D Cu Doped WO_3 Nanoplates with Structural, Optical and Differential Anti Cancer Characteristics. *Phys. E Low. Dimens. Syst. Nanostruct.* **2017**, *88*, 188–193. [CrossRef]
41. Wang, C.; Li, X.; Feng, C.; Sun, Y.; Lu, G. Nanosheets Assembled Hierarchical Flower-like WO_3 Nanostructures: Synthesis, Characterization, and Their Gas Sensing Properties. *Sens. Actuators B Chem.* **2015**, *210*, 75–81. [CrossRef]
42. Upadhyay, S.B.; Mishra, R.K.; Sahay, P.P. Cr-Doped WO_3 Nanosheets: Structural, Optical and Formaldehyde Sensing Properties. *Ceram. Int.* **2016**, *42*, 15301–15310. [CrossRef]
43. Luévano-Hipólito, E.; Martínez-de la Cruz, A.; Yu, Q.L.; Brouwers, H.J.H. Precipitation Synthesis of WO_3 for NO Removal Using PEG as Template. *Ceram. Int.* **2014**, *40*, 12123–12128. [CrossRef]
44. Mohammadi, S.; Sohrabi, M.; Golikand, A.N.; Fakhri, A. Preparation and Characterization of Zinc and Copper Co-Doped WO_3 Nanoparticles: Application in Photocatalysis and Photobiology. *J. Photochem. Photobiol. B* **2016**, *161*, 217–221. [CrossRef]
45. Banić, N.D.; Abramović, B.F.; Krstić, J.B.; Šojić Merkulov, D.V.; Finčur, N.L.; Mitrić, M.N. Novel WO_3/Fe_3O_4 Magnetic Photocatalysts: Preparation, Characterization and Thiacloprid Photodegradation. *J. Ind. Eng. Chem.* **2019**, *70*, 264–275. [CrossRef]
46. Wasmi, B.A.; Al-Amiery, A.A.; Kadhum, A.A.H.; Mohamad, A.B. Novel Approach: Tungsten Oxide Nanoparticle as a Catalyst for Malonic Acid Ester Synthesis via Ozonolysis. *J. Nanomater.* **2014**, *2014*, 715457. [CrossRef]
47. Adhikari, S.; Mandal, S.; Sarkar, D.; Kim, D.-H.; Madras, G. Kinetics and Mechanism of Dye Adsorption on WO_3 Nanoparticles. *Appl. Surf. Sci.* **2017**, *420*, 472–482. [CrossRef]

48. Luxmi, V.; Kumar, A. Dielectric and Photo-Catalytic Studies of Rapidly Synthesized m-WO_3 Nano-Particles. *Mater. Today Proc.* **2020**, *28*, 193–195. [CrossRef]
49. Rahimi, R.; Rabbani, M.; Mosaffa, M. Photocatalytic Degradation of Methylene Blue by WO_3 Prepared via a Very Simple Precipitation Method under Visible Light Irradiation. In Proceedings of the MDPI 2nd International Electronic Conference on Water Sciences (ECWS-2), Basel, Switzerland, 16 November 2017; p. 4964.
50. Thilagavathi, T.; Venugopal, D.; Marnadu, R.; Chandrasekaran, J.; Thangaraju, D.; Palanivel, B.; Hamdy, M.S.; Shkir, M.; Ali, H.E. WO_3/$CoWO_4$ Nanocomposite Synthesis Using a Facile Co-Precipitation Method for Enhanced Photocatalytic Applications. *J. Phys. Chem. Solids* **2021**, *154*, 110066. [CrossRef]
51. Azmat, S.; Jan, T.; Ilyas, S.Z.; Hassan, A.; Habib, I.; Mahmood, Q.; Mahmood, A. Solar Light Triggered Photocatalytic Performance of WO_3 Nanostructures; Waste Water Treatment. *Mater. Res. Express* **2018**, *5*, 115025. [CrossRef]
52. Firouzi, M.; Nouri, A. Facile Synthesis and Characterization of WO_3-Al_2O_3 Nanocomposites as an Effective Photocatalyst for Degradation of Congo Red under UV and Visible Light Irradiation. *Desalin. Water Treat.* **2017**, *84*, 244–254. [CrossRef]
53. Gómez-Solís, C.; Sánchez-Martínez, D.; Juárez-Ramírez, I.; Martínez-de la Cruz, A.; Torres-Martínez, L.M. Facile Synthesis of M-WO_3 Powders via Precipitation in Ethanol Solution and Evaluation of Their Photocatalytic Activities. *J. Photochem. Photobiol. A Chem.* **2013**, *262*, 28–33. [CrossRef]
54. Amarnath, M.; Heiner, A.; Gurunathan, K. Size Controlled V_2O_5-WO_3 Nano-Islands Coated Polypyrrole Matrix: A Unique Nanocomposite for Effective Room Temperature Ammonia Detection. *Sens. Actuators A Phys.* **2020**, *313*, 112211. [CrossRef]
55. Merejin, M.T.; Nasiri, M.; Abedini, E.; Sharifnia, S. Efficient Photocatalytic CO_2 Reduction by Visible-Light Responsive Fe-Doped WO_3 Nanostructures. *Indian J. Chem. Technol.* **2020**, *27*, 126–134.
56. Torabi Merajin, M.; Nasiri, M.; Abedini, E.; Sharifnia, S. Enhanced Gas-Phase Photocatalytic Oxidation of n-Pentane Using High Visible-Light-Driven Fe-Doped WO_3 Nanostructures. *J. Environ. Chem. Eng.* **2018**, *6*, 6741–6748. [CrossRef]
57. Kabcum, S.; Channei, D.; Tuantranont, A.; Wisitsoraat, A.; Liewhiran, C.; Phanichphant, S. Ultra-Responsive Hydrogen Gas Sensors Based on PdO Nanoparticle-Decorated WO_3 Nanorods Synthesized by Precipitation and Impregnation Methods. *Sens. Actuators B Chem.* **2016**, *226*, 76–89. [CrossRef]
58. Adhikari, S.; Sarkar, D. Confined Growth of WO_3 for High-Performance Electrochromic Device. *Key Eng. Mater.* **2015**, *659*, 583–587. [CrossRef]
59. Arshad, M.; Ehtisham-ul-Haque, S.; Bilal, M.; Ahmad, N.; Ahmad, A.; Abbas, M.; Nisar, J.; Khan, M.I.; Nazir, A.; Ghaffar, A.; et al. Synthesis and Characterization of Zn Doped WO_3 Nanoparticles: Photocatalytic, Antifungal and Antibacterial Activities Evaluation. *Mater. Res. Express* **2020**, *7*, 015407. [CrossRef]
60. Rajendran, V.; Deepa, B. Pronounced Effects of the Nominal Concentrations of WO_3 and Ag: WO_3 Nano-Plates (Obtained by a Co-Precipitation Method) on Their Structural, Morphological and Optical Properties. *Appl. Phys. A* **2018**, *124*, 230. [CrossRef]
61. Wang, J.; Liu, C. Preparation of 2D WO_3 Nanomaterials with Enhanced Catalytic Activities: Current Status and Perspective. *ChemBioEng Rev.* **2015**, *2*, 335–350. [CrossRef]
62. Xie, Y.P.; Liu, G.; Yin, L.; Cheng, H.-M. Crystal Facet-Dependent Photocatalytic Oxidation and Reduction Reactivity of Monoclinic WO_3 for Solar Energy Conversion. *J. Mater. Chem.* **2012**, *22*, 6746. [CrossRef]
63. Mehmood, F.; Iqbal, J.; Ismail, M.; Mehmood, A. Ni Doped WO_3 Nanoplates: An Excellent Photocatalyst and Novel Nanomaterial for Enhanced Anticancer Activities. *J. Alloys Compd.* **2018**, *746*, 729–738. [CrossRef]
64. Mehmood, F.; Iqbal, J.; Jan, T.; Ahmed, W.; Ahmed, W.; Arshad, A.; Mansoor, Q.; Ilyas, S.Z.; Ismail, M.; Ahmad, I. Effect of Sn Doping on the Structural, Optical, Electrical and Anticancer Properties of WO_3 Nanoplates. *Ceram. Int.* **2016**, *42*, 14334–14341. [CrossRef]
65. Upadhyay, S.B.; Mishra, R.K.; Sahay, P.P. Structural and Alcohol Response Characteristics of Sn-Doped WO_3 Nanosheets. *Sens. Actuators B Chem.* **2014**, *193*, 19–27. [CrossRef]
66. Upadhyay, S.B.; Mishra, R.K.; Sahay, P.P. Enhanced Acetone Response in Co-Precipitated WO_3 Nanostructures upon Indium Doping. *Sens. Actuators B Chem.* **2015**, *209*, 368–376. [CrossRef]
67. Upadhyay, S.B.; Sahay, P.P. Structure, Optical and Formaldehyde Sensing Properties of Co-Precipitated Fe-Doped WO_3 Nanomaterials. *Nano* **2015**, *10*, 1550113. [CrossRef]
68. Yu, H.; Li, J.; Li, Z.; Tian, Y.; Yang, Z. Enhanced Formaldehyde Sensing Performance Based on Ag@WO_3 2D Nanocomposite. *Powder Technol.* **2019**, *343*, 1–10. [CrossRef]
69. Sánchez-Martínez, D.; Martínez-de la Cruz, A.; López-Cuéllar, E. Synthesis of WO_3 Nanoparticles by Citric Acid-Assisted Precipitation and Evaluation of Their Photocatalytic Properties. *Mater. Res. Bull.* **2013**, *48*, 691–697. [CrossRef]
70. Mitchell, J.B.; Lo, W.C.; Genc, A.; LeBeau, J.; Augustyn, V. Transition from Battery to Pseudocapacitor Behavior via Structural Water in Tungsten Oxide. *Chem. Mater.* **2017**, *29*, 3928–3937. [CrossRef]
71. Park, C.Y.; Seo, J.M.; Jo, H.; Park, J.; Ok, K.M.; Park, T.J. Hexagonal Tungsten Oxide Nanoflowers as Enzymatic Mimetics and Electrocatalysts. *Sci. Rep.* **2017**, *7*, 40928. [CrossRef] [PubMed]
72. Girish Kumar, S.; Koteswara Rao, K.S.R. Tungsten-Based Nanomaterials ($WO_3Bi_2WO_6$): Modifications Related to Charge Carrier Transfer Mechanisms and Photocatalytic Applications. *Appl. Surf. Sci.* **2015**, *355*, 939–958. [CrossRef]
73. Esmaeili, M.; Kiani, G.; Nogorani, F.S.; Boroommand, S. Acetone Sensing Properties of Hierarchical WO_3 Core-Shell Microspheres in Comparison with Commercial Nanoparticles. *Int. J. Nano Dimens.* **2013**, *7*, 254–262.

74. Zhang, S.; Li, H.; Yang, Z. Controllable Synthesis of WO_3 with Different Crystalline Phases and Its Applications on Methylene Blue Removal from Aqueous Solution. *J. Alloys Compd.* **2017**, *722*, 555–563. [CrossRef]
75. Li, N.; Zhao, Y.; Wang, Y.; Lu, Y.; Song, Y.; Huang, Z.; Li, Y.; Zhao, J. Aqueous Synthesis and Visible-Light Photochromism of Metastable H-WO_3 Hierarchical Nanostructures. *Eur. J. Inorg. Chem.* **2015**, *2015*, 2804–2812. [CrossRef]
76. Priya, R.; Raman, M.S.; Senthilkumar, N.; Balan, R. Synthesis and Characterization of Tungsten Oxide Sponge like Sub-Microstructures in the Presence of Novel Surfactants. *Int. J. Sci. Res.* **2014**, *25*, 301–309.
77. Kavitha, N.S.; Venkatesh, K.S.; Palani, N.S.; Ilangovan, R. Fungus Mediated Biosynthesis of WO_3 Nanoparticles Using Fusarium Solani Extract. *AIP Conf. Proc.* **2017**, *1832*, 050130. [CrossRef]
78. Huang, J.; Xu, X.; Gu, C.; Fu, G.; Wang, W.; Liu, J. Flower-like and Hollow Sphere-like WO_3 Porous Nanostructures: Selective Synthesis and Their Photocatalysis Property. *Mater. Res. Bull.* **2012**, *47*, 3224–3232. [CrossRef]
79. Manukyan, K.V.; Cross, A.; Roslyakov, S.; Rouvimov, S.; Rogachev, A.S.; Wolf, E.E.; Mukasyan, A.S. Solution Combustion Synthesis of Nano-Crystalline Metallic Materials: Mechanistic Studies. *J. Phys. Chem. C* **2013**, *117*, 24417–24427. [CrossRef]
80. Danks, A.E.; Hall, S.R.; Schnepp, Z. The Evolution of 'Sol–Gel' Chemistry as a Technique for Materials Synthesis. *Mater. Horiz.* **2016**, *3*, 91–112. [CrossRef]
81. Varma, A.; Mukasyan, A.S.; Rogachev, A.S.; Manukyan, K.V. Solution Combustion Synthesis of Nanoscale Materials. *Chem. Rev.* **2016**, *116*, 14493–14586. [CrossRef] [PubMed]
82. Li, F.; Ran, J.; Jaroniec, M.; Qiao, S.Z. Solution Combustion Synthesis of Metal Oxide Nanomaterials for Energy Storage and Conversion. *Nanoscale* **2015**, *7*, 17590–17610. [CrossRef] [PubMed]
83. Aliasghari, H.; Arabi, A.M.; Haratizadeh, H. A Novel Approach for Solution Combustion Synthesis of Tungsten Oxide Nanoparticles for Photocatalytic and Electrochromic Applications. *Ceram. Int.* **2020**, *46*, 403–414. [CrossRef]
84. Carlos, E.; Martins, R.; Fortunato, E.; Branquinho, R. Solution Combustion Synthesis: Towards a Sustainable Approach for Metal Oxides. *Chem.—A Eur. J.* **2020**, *26*, 9099–9125. [CrossRef]
85. Novitskaya, E.; Kelly, J.P.; Bhaduri, S.; Graeve, O.A. A Review of Solution Combustion Synthesis: An Analysis of Parameters Controlling Powder Characteristics. *Int. Mater. Rev.* **2021**, *66*, 188–214. [CrossRef]
86. Deganello, F.; Tyagi, A.K. Solution Combustion Synthesis, Energy and Environment: Best Parameters for Better Materials. *Prog. Cryst. Growth Charact. Mater.* **2018**, *64*, 23–61. [CrossRef]
87. Branquinho, R.; Santa, A.; Carlos, E.; Salgueiro, D.; Barquinha, P.; Martins, R.; Fortunato, E. Solution Combustion Synthesis: Applications in Oxide Electronics. In *Developments in Combustion Technology*; InTech: Vienna, Austria, 2016.
88. Vidya, S.; Solomon, S.; Thomas, J.K. Synthesis and Characterisation of MoO_3 and WO_3 Nanorods for Low Temperature Co-Fired Ceramic and Optical Applications. *J. Mater. Sci. Mater. Electron.* **2015**, *26*, 3243–3255. [CrossRef]
89. Kaplan, S.S.; Sonmez, M.S. Single Step Solution Combustion Synthesis of Hexagonal WO_3 Powders as Visible Light Photocatalysts. *Mater. Chem. Phys.* **2020**, *240*, 122152. [CrossRef]
90. Evecan, D.; Kaplan, Ş.S.; Sönmez, M.Ş.; Yıldırım, S.; Okutan, M.; Deligöz, H.; Zayim, E. Smart Glass Electrochromic Device Fabrication of Uniform Tungsten Oxide Films from Its Powder Synthesized by Solution Combustion Method. *Microelectron. Eng.* **2019**, *215*, 110989. [CrossRef]
91. Chen, P.; Qin, M.; Chen, Z.; Jia, B.; Qu, X. Solution Combustion Synthesis of Nanosized WO_3: Characterization, Mechanism and Excellent Photocatalytic Properties. *RSC Adv.* **2016**, *6*, 83101–83109. [CrossRef]
92. Aliasghari, H.; Arabi, A.M.; Haratizadeh, H. Microwave-Assisted Solution Combustion Synthesis of WO_3 Nanoparticles: Optical and Colorimetric Characteristics. *Adv. Ceram. Prog.* **2019**, *5*, 36–46. [CrossRef]
93. Singh, S.A.; Madras, G. Photocatalytic Degradation with Combustion Synthesized WO_3 and WO_3TiO_2 Mixed Oxides under UV and Visible Light. *Sep. Purif. Technol.* **2013**, *105*, 79–89. [CrossRef]
94. Pudukudy, M.; Yaakob, Z.; Rejendran, R. Visible Light Active Novel WO_3 Nanospheres for Methylene Blue Degradation. *Pharma Chem.* **2013**, *5*, 208–212.
95. Liu, Z.; Li, P.; Dong, Y.; Wan, Q.; Zhai, F.; Volinsky, A.A.; Qu, X. Facile Preparation of Hexagonal $WO_3{\cdot}0.33H_2O$/C Nanostructures and Its Electrochemical Properties for Lithium-Ion Batteries. *Appl. Surf. Sci.* **2017**, *394*, 70–77. [CrossRef]
96. Liu, Z.; Li, P.; Wan, Q.; Zhang, D.; Volinsky, A.A.; Qu, X. Low-Temperature Combustion Synthesis of Hexagonal $WO_3{\cdot}0.33H_2O$@C as Anode Material for Lithium Ion Batteries. *J. Alloys Compd.* **2017**, *701*, 215–221. [CrossRef]
97. Kaplan, Ş.S.; Sönmez, M.Ş. Effect of Citric Acid Ratio on the Synthesis of Tungsten Trioxide by Solution Combustion Route. In Proceedings of the 19th International Metallurgy Materials Congress, Istanbul, Turkey, 25–27 October 2018; pp. 506–509.
98. Salkar, A.V.; Naik, A.P.; Joshi, V.S.; Haram, S.K.; Morajkar, P.P. Designing a 3D Nanoporous Network Self-Assembly of WO_3 Nanorods for Improved Electrocapacitive Performance. *CrystEngComm* **2018**, *20*, 6683–6694. [CrossRef]
99. Salkar, A.V.; Fernandes, R.X.; Bhosale, S.V.; Morajkar, P.P. NH- and CH-Substituted Ureas as Self-Assembly Directing Motifs for Facile Synthesis and Electrocapacitive Applications of Advanced WO_3 One-Dimensional Nanorods. *ACS Appl. Energy Mater.* **2019**, *2*, 8724–8736. [CrossRef]
100. Dong, C.; Liu, X.; Guan, H.; Chen, G.; Xiao, X.; Djerdj, I.; Wang, Y. Combustion Synthesized Hierarchically Porous WO_3 for Selective Acetone Sensing. *Mater. Chem. Phys.* **2016**, *184*, 155–161. [CrossRef]
101. Salkar, A.V.; Naik, A.P.; Bhosale, S.V.; Morajkar, P.P. Designing a Rare DNA-Like Double Helical Microfiber Superstructure via Self-Assembly of In Situ Carbon Fiber-Encapsulated WO_3-x Nanorods as an Advanced Supercapacitor Material. *ACS Appl. Mater. Interfaces* **2021**, *13*, 1288–1300. [CrossRef] [PubMed]

102. Yang, H.; Zhu, M.; Li, Y. Sol–Gel Research in China: A Brief History and Recent Research Trends in Synthesis of Sol–Gel Derived Materials and Their Applications. *J. Solgel Sci. Technol.* **2023**, *106*, 406–421. [CrossRef] [PubMed]
103. Navas, D.; Fuentes, S.; Castro-Alvarez, A.; Chavez-Angel, E. Review on Sol-Gel Synthesis of Perovskite and Oxide Nanomaterials. *Gels* **2021**, *7*, 275. [CrossRef] [PubMed]
104. Bokov, D.; Turki Jalil, A.; Chupradit, S.; Suksatan, W.; Javed Ansari, M.; Shewael, I.H.; Valiev, G.H.; Kianfar, E. Nanomaterial by Sol-Gel Method: Synthesis and Application. *Adv. Mater. Sci. Eng.* **2021**, *2021*, 5102014. [CrossRef]
105. Feinle, A.; Elsaesser, M.S.; Hüsing, N. Sol–Gel Synthesis of Monolithic Materials with Hierarchical Porosity. *Chem. Soc. Rev.* **2016**, *45*, 3377–3399. [CrossRef]
106. Livage, J. Sol-Gel Synthesis of Hybrid Materials. *Bull. Mater. Sci.* **1999**, *22*, 201–205. [CrossRef]
107. Cheetham, A.K.; Mellot, C.F. In Situ Studies of the Sol−Gel Synthesis of Materials. *Chem. Mater.* **1997**, *9*, 2269–2279. [CrossRef]
108. Vinogradov, A.V.; Vinogradov, V.V. Low-Temperature Sol–Gel Synthesis of Crystalline Materials. *RSC Adv.* **2014**, *4*, 45903–45919. [CrossRef]
109. Deshmukh, K.; Kovářík, T.; Křenek, T.; Docheva, D.; Stich, T.; Pola, J. Recent Advances and Future Perspectives of Sol–Gel Derived Porous Bioactive Glasses: A Review. *RSC Adv.* **2020**, *10*, 33782–33835. [CrossRef]
110. Sriram, S.R.; Parne, S.; Vaddadi, V.S.C.S.; Edla, D.; Nagaraju, P.; Avala, R.R.; Yelsani, V.; Sontu, U.B. Nanostructured WO_3 Based Gas Sensors: A Short Review. *Sens. Rev.* **2021**, *41*, 406–424. [CrossRef]
111. Dong, C.; Zhao, R.; Yao, L.; Ran, Y.; Zhang, X.; Wang, Y. A Review on WO_3 Based Gas Sensors: Morphology Control and Enhanced Sensing Properties. *J. Alloys Compd.* **2020**, *820*, 153194. [CrossRef]
112. Cristino, V.; Longobucco, G.; Marchetti, N.; Caramori, S.; Bignozzi, C.A.; Martucci, A.; Molinari, A.; Boaretto, R.; Stevanin, C.; Argazzi, R.; et al. Photoelectrochemical Degradation of Pharmaceuticals at B25 Modified WO_3 Interfaces. *Catal. Today* **2020**, *340*, 302–310. [CrossRef]
113. Wang, B.; Zhong, X.; Zhang, Y.; Xu, H.; Zhang, Y. Microspheres Assembled by WO_3-Nanoparticles under Action of Dual Surfactants: Structure and Photoluminescence Properties. *Opt. Mater.* **2022**, *129*, 112550. [CrossRef]
114. Boateng, E.; Thind, S.S.; Chen, S.; Chen, A. Synthesis and Electrochemical Studies of WO_3-Based Nanomaterials for Environmental, Energy and Gas Sensing Applications. *Electrochem. Sci. Adv.* **2022**, *2*, e2100146. [CrossRef]
115. Shabdan, Y.; Markhabayeva, A.; Bakranov, N.; Nuraje, N. Photoactive Tungsten-Oxide Nanomaterials for Water-Splitting. *Nanomaterials* **2020**, *10*, 1871. [CrossRef]
116. Liu, X.; Chen, C.; Chen, X.; Qian, G.; Wang, J.; Wang, C.; Cao, Z.; Liu, Q. WO_3 QDs Enhanced Photocatalytic and Electrochemical Perfomance of GO/TiO_2 Composite. *Catal. Today* **2018**, *315*, 155–161. [CrossRef]
117. Deb, B.; Desai, S.; Sumanasekera, G.U.; Sunkara, M.K. Gas Sensing Behaviour of Mat-like Networked Tungsten Oxide Nanowire Thin Films. *Nanotechnology* **2007**, *18*, 285501. [CrossRef]
118. Song, H.; Li, Y.; Lou, Z.; Xiao, M.; Hu, L.; Ye, Z.; Zhu, L. Synthesis of Fe-Doped WO_3 Nanostructures with High Visible-Light-Driven Photocatalytic Activities. *Appl. Catal. B* **2015**, *166–167*, 112–120. [CrossRef]
119. Zeb, S.; Sun, G.; Nie, Y.; Cui, Y.; Jiang, X. Synthesis of Highly Oriented WO_3 Nanowire Bundles Decorated with Au for Gas Sensing Application. *Sens. Actuators B Chem.* **2020**, *321*, 128439. [CrossRef]
120. Li, W.; Da, P.; Zhang, Y.; Wang, Y.; Lin, X.; Gong, X.; Zheng, G. WO_3 Nanoflakes for Enhanced Photoelectrochemical Conversion. *ACS Nano* **2014**, *8*, 11770–11777. [CrossRef]
121. Wang, Y.; Tian, W.; Chen, L.; Cao, F.; Guo, J.; Li, L. Three-Dimensional WO_3 Nanoplate/Bi_2S_3 Nanorod Heterojunction as a Highly Efficient Photoanode for Improved Photoelectrochemical Water Splitting. *ACS Appl. Mater. Interfaces* **2017**, *9*, 40235–40243. [CrossRef] [PubMed]
122. Aliannezhadi, M.; Abbaspoor, M.; Shariatmadar Tehrani, F.; Jamali, M. High Photocatalytic WO_3 Nanoparticles Synthesized Using Sol-Gel Method at Different Stirring Times. *Opt. Quantum Electron.* **2023**, *55*, 250. [CrossRef]
123. Abbaspoor, M.; Aliannezhadi, M.; Tehrani, F.S. High-Performance Photocatalytic WO_3 Nanoparticles for Treatment of Acidic Wastewater. *J. Solgel Sci. Technol.* **2023**, *105*, 565–576. [CrossRef]
124. Susanti, D.; Stefanus Haryo, N.; Nisfu, H.; Nugroho, E.P.; Purwaningsih, H.; Kusuma, G.E.; Shih, S.-J. Comparison of the Morphology and Structure of WO_3 Nanomaterials Synthesized by a Sol-Gel Method Followed by Calcination or Hydrothermal Treatment. *Front. Chem. Sci. Eng.* **2012**, *6*, 371–380. [CrossRef]
125. Susanti, D.; Diputra, A.A.G.P.; Tananta, L.; Purwaningsih, H.; Kusuma, G.E.; Wang, C.; Shih, S.; Huang, Y. WO_3 Nanomaterials Synthesized via a Sol-Gel Method and Calcination for Use as a CO Gas Sensor. *Front. Chem. Sci. Eng.* **2014**, *8*, 179–187. [CrossRef]
126. Luxmi, V.; Kumar, A. Enhanced Photocatalytic Performance of M-WO_3 and m-Fe-Doped WO_3 Cuboids Synthesized via Sol-Gel Approach Using Egg Albumen as a Solvent. *Mater. Sci. Semicond. Process.* **2019**, *104*, 104690. [CrossRef]
127. Nagarjuna, R.; Challagulla, S.; Sahu, P.; Roy, S.; Ganesan, R. Polymerizable Sol–Gel Synthesis of Nano-Crystalline WO_3 and Its Photocatalytic Cr(VI) Reduction under Visible Light. *Adv. Powder Technol.* **2017**, *28*, 3265–3273. [CrossRef]
128. Hu, D.; Li, R.; Li, M.; Pei, J.; Guo, F.; Zhang, S. Photocatalytic Efficiencies of WO_3/TiO_2 Nanoparticles for Exhaust Decomposition under UV and Visible Light Irradiation. *Mater. Res. Express* **2018**, *5*, 095029. [CrossRef]
129. Abozeid, M.A.; Hassan, H.S.; Morsi, I.; Kashyout, A.B. Development of Nano WO_3 Doped with NiO for Wireless Gas Sensors. *Arab. J. Sci. Eng.* **2019**, *44*, 647–654. [CrossRef]
130. Brahimi, R.; Dib, K.; Trari, M.; Bessekhouad, Y. Effect of S-Doping toward the Optical Properties of WO_3 Nanoparticles. *Mater. Chem. Phys.* **2019**, *223*, 398–403. [CrossRef]

131. Ghasemi, L.; Jafari, H. Morphological Characterization of Tungsten Trioxide Nanopowders Synthesized by Sol-Gel Modified Pechini's Method. *Mater. Res.* **2017**, *20*, 1713–1721. [CrossRef]
132. Ahmed, B.; Kumar, S.; Ojha, A.K.; Donfack, P.; Materny, A. Facile and Controlled Synthesis of Aligned WO_3 Nanorods and Nanosheets as an Efficient Photocatalyst Material. *Spectrochim. Acta A Mol. Biomol. Spectrosc.* **2017**, *175*, 250–261. [CrossRef] [PubMed]
133. Ramanavičius, S.; Petrulevičienė, M.; Juodkazytė, J.; Grigucevičienė, A.; Ramanavičius, A. Selectivity of Tungsten Oxide Synthesized by Sol-Gel Method Towards Some Volatile Organic Compounds and Gaseous Materials in a Broad Range of Temperatures. *Materials* **2020**, *13*, 523. [CrossRef] [PubMed]
134. Zeng, J.; Yan, S.; Bai, J.; Zhang, Y.; Yang, G.; Zhang, D.; Liu, Z.; Liang, X. Amorphous/Ordered Porous Crystalline Stacked WO_3 Films Fabricated by Electrodeposition-Assisted Sol–Gel and Its Application to Electrochromic Devices. *J. Electroanal. Chem.* **2024**, *952*, 117969. [CrossRef]
135. Ge, C.; Wang, M.; Hussain, S.; Xu, Z.; Liu, G.; Qiao, G. Electron Transport and Electrochromic Properties of Sol-Gel WO_3 Thin Films: Effect of Crystallinity. *Thin Solid Film* **2018**, *653*, 119–125. [CrossRef]
136. Han, Z.; Ren, J.; Zhou, J.; Zhang, S.; Zhang, Z.; Yang, L.; Yin, C. Multilayer Porous Pd-WO_3 Composite Thin Films Prepared by Sol-Gel Process for Hydrogen Sensing. *Int. J. Hydrogen Energy* **2020**, *45*, 7223–7233. [CrossRef]
137. Zhi, M.; Huang, W.; Shi, Q.; Wang, M.; Wang, Q. Sol–Gel Fabrication of WO_3 RGO Nanocomposite Film with Enhanced Electrochromic Performance. *RSC Adv.* **2016**, *6*, 67488–67494. [CrossRef]
138. Xu, N.; Shen, X.; Cui, S.; Yi, X. Preparation of PAA/WO_3 Composite Films with Enhanced Electrochromism via Layer-by-Layer Method. *Sci. Eng. Compos. Mater.* **2018**, *25*, 565–569. [CrossRef]
139. Koysuren, O.; Dhoska, K.; Koysuren, H.N.; Markja, I.; Yaglikci, S.; Tuncel, B.; Bebi, E. SiO_2/WO_3/ZnO Based Self-Cleaning Coatings for Solar Cells. *J. Solgel Sci. Technol.* **2024**, *110*, 183–203. [CrossRef]
140. Wu, J.-Y.; Chen, Y.-W. Anticorrosion of WO_3-Modified TiO_2 Thin Film Prepared by Peroxo Sol-Gel Method. *Mod. Res. Catal.* **2020**, *9*, 35–46. [CrossRef]
141. Antoniadou, M.; Arfanis, M.K.; Ibrahim, I.; Falaras, P. Bifunctional G-C3N_4/WO_3 Thin Films for Photocatalytic Water Purification. *Water* **2019**, *11*, 2439. [CrossRef]
142. Zhuiykov, S.; Kats, E. Enhanced Electrical Properties in Sub-10-Nm WO_3 Nanoflakes Prepared via a Two-Step Sol-Gel-Exfoliation Method. *Nanoscale Res. Lett.* **2014**, *9*, 401. [CrossRef] [PubMed]
143. Saasa, V.; Malwela, T.; Lemmer, Y.; Beukes, M.; Mwakikunga, B. The Hierarchical Nanostructured Co-Doped WO_3/Carbon and Their Improved Acetone Sensing Perfomance. *Mater. Sci. Semicond. Process.* **2020**, *117*, 105157. [CrossRef]
144. Mena, E.; Rey, A.; Contreras, S.; Beltrán, F.J. Visible Light Photocatalytic Ozonation of DEET in the Presence of Different Forms of WO_3. *Catal. Today* **2015**, *252*, 100–106. [CrossRef]
145. Won, J.H.; Kim, M.K.; Oh, H.-S.; Jeong, H.M. Scalable Production of Visible Light Photocatalysts with Extended Nanojunctions of WO_3/g-C_3N_4 Using Zeta Potential and Phase Control in Sol-Gel Process. *Appl. Surf. Sci.* **2023**, *612*, 155838. [CrossRef]
146. Xu, T.; Wu, H.; Cui, K.; Zhao, Q.; Huang, J.; Wei, L.; Ma, Z. Hybrid TiO_2/WO_3 Nanoparticles Fabricated via a Sol–Gel Process Using Amphiphlic Poly(ε-Caprolactone)-Block-Poly(Acrylic Acid) Diblock Copolymer as Template and Their High Visible Light Photocatalytic Activity. *SN Appl. Sci.* **2019**, *1*, 866. [CrossRef]
147. Hosseini Ravandi, S.A.; Sadrjahani, M.; Valipouri, A.; Dabirian, F.; Ko, F.K. Recently Developed Electrospinning Methods: A Review. *Text. Res. J.* **2022**, *92*, 5130–5145. [CrossRef]
148. Patel, S.; Vigyan, K.; Saran, K.; Kumari, R.; Kumar, R.; Patel, S.S.; Kumar, D. Nano-Encapsulation of Milk Peptides by Electrospinning Method: A Review. *Int. J. Chem. Stud.* **2019**, *7*, 4924–4931.
149. Senthilkumar, S.H.; Ramasubramanian, B.; Rao, R.P.; Chellappan, V.; Ramakrishna, S. Advances in Electrospun Materials and Methods for Li-Ion Batteries. *Polymers* **2023**, *15*, 1622. [CrossRef]
150. Keirouz, A.; Wang, Z.; Reddy, V.S.; Nagy, Z.K.; Vass, P.; Buzgo, M.; Ramakrishna, S.; Radacsi, N. The History of Electrospinning: Past, Present, and Future Developments. *Adv. Mater. Technol.* **2023**, *8*, 2201723. [CrossRef]
151. Chen, Y.; Shafiq, M.; Liu, M.; Morsi, Y.; Mo, X. Advanced Fabrication for Electrospun Three-Dimensional Nanofiber Aerogels and Scaffolds. *Bioact. Mater.* **2020**, *5*, 963–979. [CrossRef] [PubMed]
152. Abdul Hameed, M.M.; Mohamed Khan, S.A.P.; Thamer, B.M.; Rajkumar, N.; El-Hamshary, H.; El-Newehy, M. Electrospun Nanofibers for Drug Delivery Applications: Methods and Mechanism. *Polym. Adv. Technol.* **2023**, *34*, 6–23. [CrossRef]
153. Al-Hazeem, N.Z.; Ahmed, N.M.; Mat Jafri, M.Z.; Ramizy, A. The Effect of Deposition Angle on Morphology and Diameter of Electrospun TiO_2/PVP Nanofibers. *Nanocomposites* **2021**, *7*, 70–78. [CrossRef]
154. Ezhilan, M.; JBB, A.J.; Babu, K.J.; Rayappan, J.B.B. Hierarchically Connected Electrospun WO_3 Nanowires—An Acetaldehyde Sensor. *J. Alloys Compd.* **2021**, *863*, 158407. [CrossRef]
155. Rong, F.; Lu, Q.; Mai, H.; Chen, D.; Caruso, R.A. Hierarchically Porous WO_3/$CdWO_4$ Fiber-in-Tube Nanostructures Featuring Readily Accessible Active Sites and Enhanced Photocatalytic Effectiveness for Antibiotic Degradation in Water. *ACS Appl. Mater. Interfaces* **2021**, *13*, 21138–21148. [CrossRef]
156. Lee, H.; Kim, Y.; Yu, A.; Jin, D.; Jo, A.; Lee, Y.; Kim, M.H.; Lee, C. An Efficient Electrochemical Sensor Driven by Hierarchical Hetero-Nanostructures Consisting of RuO_2 Nanorods on WO_3 Nanofibers for Detecting Biologically Relevant Molecules. *Sensors* **2019**, *19*, 3295. [CrossRef]

157. Pereira, M.F.G.; Nascimento, M.M.; Cardoso, P.H.N.; Oliveira, C.Y.B.; Tavares, G.F.; Araújo, E.S. Preparation, Microstructural Characterization and Photocatalysis Tests of V^{5+}-Doped TiO_2/WO_3 Nanocomposites Supported on Electrospun Membranes. *Inorganics* **2022**, *10*, 143. [CrossRef]
158. Morais, P.V.; Suman, P.H.; Silva, R.A.; Orlandi, M.O. High Gas Sensor Performance of WO_3 Nanofibers Prepared by Electrospinning. *J. Alloys Compd.* **2021**, *864*, 158745. [CrossRef]
159. Schanche, J.-S. Microwave Synthesis Solutions from Personal Chemistry. *Mol. Divers.* **2003**, *7*, 291–298. [CrossRef]
160. Onwudiwe, D.C. Microwave-Assisted Synthesis of PbS Nanostructures. *Heliyon* **2019**, *5*, e01413. [CrossRef]
161. Jiang, F.Y.; Wang, C.M.; Fu, Y.; Liu, R.C. Synthesis of Iron Oxide Nanocubes via Microwave-Assisted Solvolthermal Method. *J. Alloys Compd.* **2010**, *503*, L31–L33. [CrossRef]
162. Lemos, S.C.S.; de Lima Rezende, T.K.; Assis, M.; da Costa Romeiro, F.; Peixoto, D.A.; de Oliveira Gomes, E.; Jacobsen, G.M.; Teodoro, M.D.; Gracia, L.; Ferrari, J.L.; et al. Efficient Ni and Fe Doping Process in ZnO with Enhanced Photocatalytic Activity: A Theoretical and Experimental Investigation. *Mater. Res. Bull.* **2022**, *152*, 111849. [CrossRef]
163. Manikandan, V.; Anushkkaran, P.; Chae, W.-S.; Chung, H.-S.; Park, J.H.; Jang, J.S. Microwave-Assisted Thermochemical Conversion of Zr–FeOOH Nanorods to Zr–$ZnFe_2O_4$ Nanorods for Bacterial Disinfection and Photo-Fenton Catalytic Degradation of Organic Pollutants. *Chemosphere* **2022**, *299*, 134363. [CrossRef] [PubMed]
164. Ju, Y.; Liu, R.; Ji, G.; Su, L.; Qiao, J.; Xing, W.; Fan, D.; Zhao, K.; Dionysiou, D.D. Novel Strategy for Enhanced Visible Light-Responsive Photoactivity of $ZnFe_2O_4$ with a Single-Mode Microwave Combustion Process: Primary Parameters. *Chem. Eng. J.* **2022**, *440*, 135551. [CrossRef]
165. Xiongjin, Z.; Chenhui, L.; Yongli, W.; Fang, W.; Jiyun, G.; Libo, Z. Reduction Mechanism and Optimization of Prepare Metallic Antimony through Direct Microwave Carbothermal Reduction of Antimony Oxide Concentrate. *J. Mater. Res. Technol.* **2022**, *18*, 882–895. [CrossRef]
166. Kowsalya, M.; Paulraj, S.; Rajagopal, S.; Premchandran, V.; Veluswamy, P.; Kathirvel, V. Effect of Surfactant on the Electrochemical Performance of WO_3 as Supercapacitor Electrode. *J. Mater. Sci. Mater. Electron.* **2022**, *33*, 8833–8843. [CrossRef]
167. Hernandez-Uresti, D.B.; Sánchez-Martínez, D.; Martínez-de la Cruz, A.; Sepúlveda-Guzmán, S.; Torres-Martínez, L.M. Characterization and Photocatalytic Properties of Hexagonal and Monoclinic WO_3 Prepared via Microwave-Assisted Hydrothermal Synthesis. *Ceram. Int.* **2014**, *40*, 4767–4775. [CrossRef]
168. Harini, S.; Arumugam, A.; Kale, S.C.; Narawane, J.; Pawar, J.; Masurkar, S.; Ruikar, S. Microwave-Assisted Solvothermal Synthesis of Tungsten Oxide (WO_3) Nanoparticles for Microbial Inhibition. *Int. J. Curr. Res. Rev.* **2021**, *13*, 76–79. [CrossRef]
169. Vodop'yanov, A.V.; Mansfeld, D.A.; Samokhin, A.V.; Alekseev, N.V.; Tsvetkov, Y.V. Production of Nanopowders by the Evaporation–Condensation Method Using a Focused Microwave Radiation. *Radiophys. Quantum Electron.* **2017**, *59*, 698–705. [CrossRef]
170. Xiao, S.; Zhou, C.; Ye, X.; Lian, Z.; Zhang, N.; Yang, J.; Chen, W.; Li, H. Solid-Phase Microwave Reduction of WO_3 by GO for Enhanced Synergistic Photo-Fenton Catalytic Degradation of Bisphenol A. *ACS Appl. Mater. Interfaces* **2020**, *12*, 32604–32614. [CrossRef]
171. Nayak, A.K.; Pradhan, D. Microwave-Assisted Greener Synthesis of Defect-Rich Tungsten Oxide Nanowires with Enhanced Photocatalytic and Photoelectrochemical Performance. *J. Phys. Chem. C* **2018**, *122*, 3183–3193. [CrossRef]
172. Periasamy, P.; Krishnakumar, T.; Sathish, M.; Devarajan, V.P.; Siril, P.F.; Chavali, M. Investigation of Electrochemical Properties of Microwave Irradiated Tungsten Oxide (WO_3) Nanorod Structures for Supercapacitor Electrode in KOH Electrolyte. *Mater. Res. Express* **2018**, *5*, 085007. [CrossRef]
173. Ryu, S.; Nam, C. Adsorption Characteristics of Methylene Blue on WO_3 Nanorods Prepared by Microwave-Assisted Hydrothermal Methods. *Phys. Status Solidi A* **2018**, *215*, 1700996. [CrossRef]
174. McDonald, K.D.; Bartlett, B.M. Photocatalytic Primary Alcohol Oxidation on WO_3 Nanoplatelets. *RSC Adv.* **2019**, *9*, 28688–28694. [CrossRef] [PubMed]
175. Tu, Y.; Li, Q.; Jiang, D.; Wang, Q.; Feng, T. Microwave Intercalation Synthesis of WO_3 Nanoplates and Their NO-Sensing Properties. *J. Mater. Eng. Perform.* **2015**, *24*, 274–279. [CrossRef]
176. Gui, Y.; Tian, K.; Liu, J.; Yang, L.; Zhang, H.; Wang, Y. Superior Triethylamine Detection at Room Temperature by {-112} Faceted WO_3 Gas Sensor. *J. Hazard. Mater.* **2019**, *380*, 120876. [CrossRef]
177. Wang, Z.; Sun, P.; Yang, T.; Gao, Y.; Li, X.; Lu, G.; Du, Y. Flower-like WO_3 Architectures Synthesized via a Microwave-Assisted Method and Their Gas Sensing Properties. *Sens. Actuators B Chem.* **2013**, *186*, 734–740. [CrossRef]
178. Nunes, D.; Fragoso, A.R.; Freire, T.; Matias, M.; Marques, A.C.; de Paiva Martins, R.F.; Fortunato, E.; Pimentel, A. Ultrafast Microwave Synthesis of WO_3 Nanostructured Films for Solar Photocatalysis. *Phys. Status Solidi RRL—Rapid Res. Lett.* **2021**, *15*, 2100196. [CrossRef]
179. Huo, Y.; Xiu, S.; Meng, L.-Y.; Quan, B. Solvothermal Synthesis and Applications of Micro/Nano Carbons: A Review. *Chem. Eng. J.* **2023**, *451*, 138572. [CrossRef]
180. Dem'yanets, L.N.; Lyutin, V.I. Status of Hydrothermal Growth of Bulk ZnO: Latest Issues and Advantages. *J. Cryst. Growth* **2008**, *310*, 993–999. [CrossRef]
181. Gupta, T.; Samriti; Cho, J.; Prakash, J. Hydrothermal Synthesis of TiO_2 Nanorods: Formation Chemistry, Growth Mechanism, and Tailoring of Surface Properties for Photocatalytic Activities. *Mater. Today Chem.* **2021**, *20*, 100428. [CrossRef]

182. Kim, C.; Kim, S.H.; Lee, S.; Kwon, I.; Kim, S.H.; Kim, S.; Seok, C.; Park, Y.S.; Kim, Y. Boosting Overall Water Splitting by Incorporating Sulfur into NiFe (Oxy)Hydroxide. *J. Energy Chem.* **2022**, *64*, 364–371. [CrossRef]
183. Marciniuk, G.; Ferreira, R.T.; Pedroso, A.V.; Ribas, A.S.; Ribeiro, R.A.P.; de Lázaro, S.R.; de Souza, E.C.F.; Marchesi, L.F.Q.; Garcia, J.R. Enhancing Hydrothermal Formation of α-MnO_2 Nanoneedles over Nanographite Structures Obtained by Electrochemical Exfoliation. *Bull. Mater. Sci.* **2021**, *44*, 62. [CrossRef]
184. Liang, C.; Yang, H.; Yu, K.; Jin, W. Sunflower Seed Husk-Derived Submicron Carbon Spheres and SnO_2 Nanoparticles Composite Used as an Anode for High-Performance Lithium-Ion Batteries. *Diam. Relat. Mater.* **2021**, *116*, 108392. [CrossRef]
185. Liu, P.; Cai, W.; Chen, J.; Yang, Z.; Zhou, J.; Cai, Z.; Fan, J. One-Pot Hydrothermal Preparation of Manganese-Doped Carbon Microspheres for Effective Deep Removal of Hexavalent Chromium from Wastewater. *J. Colloid. Interface Sci.* **2021**, *599*, 427–435. [CrossRef]
186. Sharma, S.K.; Gupta, R.; Sharma, G.; Vemula, K.; Koirala, A.R.; Kaushik, N.K.; Choi, E.H.; Kim, D.Y.; Purohit, L.P.; Singh, B.P. Photocatalytic Performance of Yttrium-Doped CNT-ZnO Nanoflowers Synthesized from Hydrothermal Method. *Mater. Today Chem.* **2021**, *20*, 100452. [CrossRef]
187. Sen, S.K.; Dutta, S.; Paik, L.; Paul, T.C.; Manir, M.S.; Hossain, M.; Hossain, M.N. Dy-Doped MoO_3 Nanobelts Synthesized via Hydrothermal Route: Influence of Dy Contents on the Structural, Morphological and Optical Properties. *J. Alloys Compd.* **2021**, *876*, 160070. [CrossRef]
188. Wang, S.; Li, M.-D.; Qin, G.-X.; Dong, Y.-B. Melamine-Assisted Synthesis of Cobalt–Nickel Coordination Polymers as Electrode Materials for Supercapacitors. *J. Mater. Sci.* **2021**, *56*, 13752–13762. [CrossRef]
189. Dou, L.; Zhong, J.; Li, J.; Pandian, R.; Burda, C. In-Situ Construction of 3D Nanoflower-like BiOI/Bi_2SiO_5 Heterojunctions with Enhanced Photocatalytic Performance for Removal of Decontaminants Originated from a Step-Scheme Mechanism. *Appl. Surf. Sci.* **2021**, *544*, 148883. [CrossRef]
190. Liu, G.; Wang, L.; Hu, Y.; Sun, C.; Leng, H.; Li, Q.; Wu, C. Enhanced Catalytic Effect of TiO_2@rGO Synthesized by One-Pot Ethylene Glycol-Assisted Solvothermal Method for MgH2. *J. Alloys Compd.* **2021**, *881*, 160644. [CrossRef]
191. Zhou, F.; Zhao, Y.; Zhou, W.; Tang, D. Temperature Dependent Raman of BiTe Nanotubes. *AIP Adv.* **2018**, *8*, 125330. [CrossRef]
192. Shen, S.; Zhang, X.; Cheng, X.; Xu, Y.; Gao, S.; Zhao, H.; Zhou, X.; Huo, L. Oxygen-Vacancy-Enriched Porous α-MoO_3 Nanosheets for Trimethylamine Sensing. *ACS Appl. Nano Mater.* **2019**, *2*, 8016–8026. [CrossRef]
193. Bano, K.; Bajwa, S.Z.; Bassous, N.J.; Webster, T.J.; Shaheen, A.; Taj, A.; Hameed, S.; Tehseen, B.; Dai, Z.; Iqbal, M.Z.; et al. Development of Biocompatible 1D CuO Nanoneedles and Their Potential for Sensitive, Mass-Based Detection of Anti-Tuberculosis Drugs. *Appl. Nanosci.* **2019**, *9*, 1341–1351. [CrossRef]
194. Hu, Q.; Wang, Z.; Chang, J.; Wan, P.; Huang, J.; Feng, L. Design and Preparation of Hollow NiO Sphere- Polyaniline Composite for NH_3 Gas Sensing at Room Temperature. *Sens. Actuators B Chem.* **2021**, *344*, 130179. [CrossRef]
195. Zhou, W.; Deng, J.; Qin, Z.; Huang, R.; Wang, Y.; Tong, S. Construction of MoS_2 Nanoarrays and MoO_3 Nanobelts: Two Efficient Adsorbents for Removal of Pb(II), Au(III) and Methylene Blue. *J. Environ. Sci.* **2022**, *111*, 38–50. [CrossRef]
196. Ponnusamy, G.; Farzaneh, H.; Tong, Y.; Lawler, J.; Liu, Z.; Saththasivam, J. Enhanced Catalytic Ozonation of Ibuprofen Using a 3D Structured Catalyst with MnO_2 Nanosheets on Carbon Microfibers. *Sci. Rep.* **2021**, *11*, 6342. [CrossRef]
197. Saadat Niavol, S.; Milani Moghaddam, H. SnO_2 Nanoparticles/Reduced Graphene Oxide Nanocomposite for Fast Ethanol Vapor Sensing at a Low Operating Temperature with an Excellent Long-Term Stability. *J. Mater. Sci. Mater. Electron.* **2021**, *32*, 6550–6569. [CrossRef]
198. Biswal, S.; Bhaskaram, D.S.; Govindaraj, G. Role of Graphene Oxide in Modifying Magnetism in α-Fe_2O_3 Nanoparticles: Raman and Magnetization Studies. *Mater. Chem. Phys.* **2021**, *266*, 124531. [CrossRef]
199. Muqoyyana, M.; Suriani, A.B.; Mohamed, A.; Hashim, N.; Mamat, M.H.; Ahmad, M.K.; Othman, M.H.D.; Mohamed, M.A.; Nurhafizah, M.D.; Birowosuto, M.D.; et al. Effects of TiO_2 Phase and Nanostructures as Photoanode on the Performance of Dye-Sensitized Solar Cells. *Bull. Mater. Sci.* **2021**, *44*, 10. [CrossRef]
200. Yamuna, A.; Hong, C.-Y.; Chen, S.-M.; Chen, T.-W.; Alabdullkarem, E.A.; Soylak, M.; Mana AL-Anazy, M.; Ajmal Ali, M.; Liu, X. Highly Selective Simultaneous Electrochemical Detection of Trace Level of Heavy Metals in Water Samples Based on the Single-Crystalline Co3O4 Nanocubes Modified Electrode. *J. Electroanal. Chem.* **2021**, *887*, 115159. [CrossRef]
201. Sufyan, M.; Mehmood, U.; Qayyum Gill, Y.; Nazar, R.; Ul Haq Khan, A. Hydrothermally Synthesize Zinc Oxide (ZnO) Nanorods as an Effective Photoanode Material for Third-Generation Dye-Sensitized Solar Cells (DSSCs). *Mater. Lett.* **2021**, *297*, 130017. [CrossRef]
202. Zha, R.; Shi, T.; He, L.; Zhang, M. Synergetic Excitonic and Defective Effects in Confined SnO_2/α-Fe_2O_3 Nanoheterojunctions for Efficient Photocatalytic Molecular Oxygen Activation. *Chem. Eng. J.* **2021**, *421*, 129883. [CrossRef]
203. Khurram, R.; Wang, Z.; Ehsan, M.F.; Peng, S.; Shafiq, M.; Khan, B. Synthesis and Characterization of an α-Fe_2O_3 /ZnTe Heterostructure for Photocatalytic Degradation of Congo Red, Methyl Orange and Methylene Blue. *RSC Adv.* **2020**, *10*, 44997–45007. [CrossRef] [PubMed]
204. Haghparas, Z.; Kordrostami, Z.; Sorouri, M.; Rajabzadeh, M.; Khalifeh, R. Highly Sensitive Non-Enzymatic Electrochemical Glucose Sensor Based on Dumbbell-Shaped Double-Shelled Hollow Nanoporous CuO/ZnO Microstructures. *Sci. Rep.* **2021**, *11*, 344. [CrossRef] [PubMed]
205. Chang, P.; Zhang, S.; Xu, X.; Lin, Y.; Chen, X.; Guan, L.; Tao, J. Facile Synthesis of MoS_2/$Ni_2V_3O_8$ Nanosheets for PH-Universal Efficient Hydrogen Evolution Catalysis. *Chem. Eng. J.* **2021**, *423*, 130196. [CrossRef]

206. Bozetine, H.; Meziane, S.; Aziri, S.; Berkane, N.; Allam, D.; Boudinar, S.; Hadjersi, T. Facile and Green Synthesis of a ZnO/CQDs/AgNPs Ternary Heterostructure Photocatalyst: Study of the Methylene Blue Dye Photodegradation. *Bull. Mater. Sci.* **2021**, *44*, 64. [CrossRef]
207. Feng, S.; Xu, R. New Materials in Hydrothermal Synthesis. *Acc. Chem. Res.* **2001**, *34*, 239–247. [CrossRef]
208. Kumar, R.; Aadil, K.R.; Ranjan, S.; Kumar, V.B. Advances in Nanotechnology and Nanomaterials Based Strategies for Neural Tissue Engineering. *J. Drug Deliv. Sci. Technol.* **2020**, *57*, 101617. [CrossRef]
209. Li, J.; Wu, Q.; Wu, J. Synthesis of Nanoparticles via Solvothermal and Hydrothermal Methods. In *Handbook of Nanoparticles*; Springer International Publishing: Cham, Switzerland, 2015; pp. 1–28.
210. Ma, J.; He, Y.-S.; Zhang, W.; Wang, J.; Yang, X.; Liao, X.-Z.; Ma, Z.-F. An Experimental Insight into the Advantages of in Situ Solvothermal Route to Construct 3D Graphene-Based Anode Materials for Lithium-Ion Batteries. *Nano Energy* **2015**, *16*, 235–246. [CrossRef]
211. Walton, R.I. Perovskite Oxides Prepared by Hydrothermal and Solvothermal Synthesis: A Review of Crystallisation, Chemistry, and Compositions. *Chem.—A Eur. J.* **2020**, *26*, 9041–9069. [CrossRef]
212. Liu, D.; Ren, X.; Li, Y.; Tang, Z.; Zhang, Z. Nanowires-Assembled WO_3 Nanomesh for Fast Detection of Ppb-Level NO_2 at Low Temperature. *J. Adv. Ceram.* **2020**, *9*, 17–26. [CrossRef]
213. Hung, C.M.; Dat, D.Q.; Van Duy, N.; Van Quang, V.; Van Toan, N.; Van Hieu, N.; Hoa, N.D. Facile Synthesis of Ultrafine RGO/WO_3 Nanowire Nanocomposites for Highly Sensitive Toxic NH_3 Gas Sensors. *Mater. Res. Bull.* **2020**, *125*, 110810. [CrossRef]
214. Nekita, S.; Nagashima, K.; Zhang, G.; Wang, Q.; Kanai, M.; Takahashi, T.; Hosomi, T.; Nakamura, K.; Okuyama, T.; Yanagida, T. Face-Selective Crystal Growth of Hydrothermal Tungsten Oxide Nanowires for Sensing Volatile Molecules. *ACS Appl. Nano Mater.* **2020**, *3*, 10252–10260. [CrossRef]
215. Tang, K.; Zhang, Y.; Shi, Y.; Cui, J.; Shu, X.; Wang, Y.; Qin, Y.; Liu, J.; Tan, H.H.; Wu, Y. Crystalline WO_3 Nanowires Array Sheathed with Sputtered Amorphous Shells for Enhanced Electrochromic Performance. *Appl. Surf. Sci.* **2019**, *498*, 143796. [CrossRef]
216. Tang, K.; Zhang, Y.; Shi, Y.; Cui, J.; Shu, X.; Wang, Y.; Qin, Y.; Liu, J.; Tan, H.H.; Wu, Y. Fabrication of WO_3/TiO_2 Core-Shell Nanowire Arrays: Structure Design and High Electrochromic Performance. *Electrochim. Acta* **2020**, *330*, 135189. [CrossRef]
217. Wang, N.; Wang, D.; Li, M.; Shi, J.; Li, C. Photoelectrochemical Water Oxidation on Photoanodes Fabricated with Hexagonal Nanoflower and Nanoblock WO_3. *Nanoscale* **2014**, *6*, 2061. [CrossRef]
218. Nayak, A.K.; Sohn, Y.; Pradhan, D. Facile Green Synthesis of $WO_3 \cdot H_2O$ Nanoplates and WO_3 Nanowires with Enhanced Photoelectrochemical Performance. *Cryst. Growth Des.* **2017**, *17*, 4949–4957. [CrossRef]
219. Yao, S.; Qu, F.; Wang, G.; Wu, X. Facile Hydrothermal Synthesis of WO_3 Nanorods for Photocatalysts and Supercapacitors. *J. Alloys Compd.* **2017**, *724*, 695–702. [CrossRef]
220. Lu, N.; Gao, X.; Yang, C.; Xiao, F.; Wang, J.; Su, X. Enhanced Formic Acid Gas-Sensing Property of WO_3 Nanorod Bundles via Hydrothermal Method. *Sens. Actuators B Chem.* **2016**, *223*, 743–749. [CrossRef]
221. Van Tong, P.; Hoa, N.D.; Van Duy, N.; Le, D.T.T.; Van Hieu, N. Enhancement of Gas-Sensing Characteristics of Hydrothermally Synthesized WO_3 Nanorods by Surface Decoration with Pd Nanoparticles. *Sens. Actuators B Chem.* **2016**, *223*, 453–460. [CrossRef]
222. Mohamed, R.M.; Shawky, A. Improved Photocatalytic Oxidation of Ciprofloxacin by NiS-Coupled WO_3 Nanorods Synthesized by Solvothermal Method under Visible Light. *Ceram. Int.* **2023**, *49*, 21855–21863. [CrossRef]
223. Xiao, J.; Che, Y.; Lv, B.; Benedicte, M.-C.; Feng, G.; Sun, T.; Song, C. Synthesis of WO_3 Nanorods and Their Excellent Ethanol Gas-Sensing Performance. *Mater. Res.* **2021**, *24*, e20200434. [CrossRef]
224. Wang, Q.; Fu, H.; Ding, J.; Yang, C.; Wang, S. Sensitivity Enhanced Microfiber Interferometer Ammonia Gas Sensor by Using WO_3 Nanorods Coatings. *Opt. Laser Technol.* **2020**, *125*, 106036. [CrossRef]
225. Zhai, C.; Luo, Z.; Liang, X.; Song, X.; Zhang, M. A Superior Selective and Anti-Jamming Performance Triethylamine Sensing Sensor Based on Hierarchical WO_3 Nanoclusters. *J. Alloys Compd.* **2021**, *857*, 157545. [CrossRef]
226. Tahir, M.B.; Ashraf, M.; Rafique, M.; Ijaz, M.; Firman, S.; Mubeen, I. Activated Carbon Doped WO_3 for Photocatalytic Degradation of Rhodamine-B. *Appl. Nanosci.* **2020**, *10*, 869–877. [CrossRef]
227. Liu, Y.S.; Xi, X.L.; Nie, Z.R.; Zhao, L.Y.; Fan, Y.S. Effect of Hydrothermal Conditions on Crystal Structure, Morphology and Visible-Light Driven Photocatalysis of WO_3 Nanostructures. *Mater. Sci. Forum* **2020**, *993*, 893–898. [CrossRef]
228. Wang, Z.; Wang, D.; Sun, J. Controlled Synthesis of Defect-Rich Ultrathin Two-Dimensional WO_3 Nanosheets for NO_2 Gas Detection. *Sens. Actuators B Chem.* **2017**, *245*, 828–834. [CrossRef]
229. Song, W.; Zhang, R.; Bai, X.; Jia, Q.; Ji, H. Exposed Crystal Facets of WO_3 Nanosheets by Phase Control on NO_2-Sensing Performance. *J. Mater. Sci. Mater. Electron.* **2020**, *31*, 610–620. [CrossRef]
230. Abe, O.O.; Qiu, Z.; Jinschek, J.R.; Gouma, P.-I. Effect of (100) and (001) Hexagonal WO_3 Faceting on Isoprene and Acetone Gas Selectivity. *Sensors* **2021**, *21*, 1690. [CrossRef]
231. Ji, H.; Zeng, W.; Xu, Y.; Li, Y. Nanosheet-Assembled Hierarchical WO_3 Flower-like Nanostructures: Hydrothermal Synthesis and NH3-Sensing Properties. *Mater. Lett.* **2019**, *250*, 155–158. [CrossRef]
232. Wang, B.-R.; Wang, R.-Z.; Liu, L.-Y.; Wang, C.; Zhang, Y.-F.; Sun, J.-B. WO_3 Nanosheet/$W_{18}O_{49}$ Nanowire Composites for NO_2 Sensing. *ACS Appl. Nano Mater.* **2020**, *3*, 5473–5480. [CrossRef]
233. Wang, C.; Zhang, S.; Qiu, L.; Rasaki, S.A.; Qu, F.; Thomas, T.; Liu, Y.; Yang, M. Ru-Decorated WO_3 Nanosheets for Efficient Xylene Gas Sensing Application. *J. Alloys Compd.* **2020**, *826*, 154196. [CrossRef]

234. Zhang, D.; Fan, Y.; Li, G.; Ma, Z.; Wang, X.; Cheng, Z.; Xu, J. Highly Sensitive BTEX Sensors Based on Hexagonal WO_3 Nanosheets. *Sens. Actuators B Chem.* **2019**, *293*, 23–30. [CrossRef]
235. Wei, Z.; Zhou, Q.; Lu, Z.; Xu, L.; Gui, Y.; Tang, C. Morphology Controllable Synthesis of Hierarchical WO_3 Nanostructures and C2H2 Sensing Properties. *Phys. E Low. Dimens. Syst. Nanostruct.* **2019**, *109*, 253–260. [CrossRef]
236. Yang, Z.; Wang, J.; Wang, J.; Li, M.; Cheng, Q.; Wang, Z.; Wang, X.; Li, J.; Li, Y.; Zhang, G. 2D WO_{3-x} Nanosheet with Rich Oxygen Vacancies for Efficient Visible-Light-Driven Photocatalytic Nitrogen Fixation. *Langmuir* **2022**, *38*, 1178–1187. [CrossRef]
237. Wu, X.; Yao, S. Flexible Electrode Materials Based on WO_3 Nanotube Bundles for High Performance Energy Storage Devices. *Nano Energy* **2017**, *42*, 143–150. [CrossRef]
238. Song, C.; Li, C.; Yin, Y.; Xiao, J.; Zhang, X.; Song, M.; Dong, W. Preparation and Gas Sensing Properties of Partially Broken WO_3 Nanotubes. *Vacuum* **2015**, *114*, 13–16. [CrossRef]
239. Shende, P.; Kasture, P.; Gaud, R.S. Nanoflowers: The Future Trend of Nanotechnology for Multi-Applications. *Artif. Cells Nanomed. Biotechnol.* **2018**, *46*, 413–422. [CrossRef]
240. Bhosale, N.Y.; Mali, S.S.; Hong, C.K.; Kadam, A.V. Hydrothermal Synthesis of WO_3 Nanoflowers on Etched ITO and Their Electrochromic Properties. *Electrochim. Acta* **2017**, *246*, 1112–1120. [CrossRef]
241. Fang, W.; Yang, Y.; Yu, H.; Dong, X.; Wang, T.; Wang, J.; Liu, Z.; Zhao, B.; Yang, M. One-Step Synthesis of Flower-Shaped WO_3 Nanostructures for a High-Sensitivity Room-Temperature NOx Gas Sensor. *RSC Adv.* **2016**, *6*, 106880–106886. [CrossRef]
242. Gui, Y.; Liu, Z.; Fang, S.; Tian, J.; Gong, F. Synthesis of Flower-like WO_3/Graphene Nanocomposite by Microwave-Assisted Hydrothermal Method and the Enhanced Gas-Sensing Properties to Aniline. *J. Mater. Sci. Mater. Electron.* **2016**, *27*, 2890–2895. [CrossRef]
243. Li, D.-K.; He, B.-Y.; Chen, K.-Q.; Pi, M.-Y.; Cui, Y.-T.; Zhang, D.-K. Xylene Gas Sensing Performance of Au Nanoparticlesloaded WO_3 Nanoflowers. *Acta Phys. Sin.* **2019**, *68*, 198101. [CrossRef]
244. Gu, Y.; Zheng, W.; Bu, Y. Facile Preparation of Nanoflower Structured WO_3 Thin Film on Etched Titanium Substrate with High Photoelectrochemical Performance. *J. Electroanal. Chem.* **2019**, *833*, 54–62. [CrossRef]
245. Zhi, L.; Zhang, S.; Xu, Y.; Tu, J.; Li, M.; Hu, D.; Liu, J. Controlled Growth of AgI Nanoparticles on Hollow WO_3 Hierarchical Structures to Act as Z-Scheme Photocatalyst for Visible-Light Photocatalysis. *J. Colloid. Interface Sci.* **2020**, *579*, 754–765. [CrossRef] [PubMed]
246. Dutta, P.; Karumuthil, S.C.; Roy, R.; Singh, A.K. Highly Stable Poly(*o*-Methoxyaniline)/WO_3-Nanoflower Composite-Based Electrochromic Supercapacitors with Real-Time Charge Indication. *ACS Appl. Polym. Mater.* **2023**, *5*, 4088–4099. [CrossRef]
247. Santos, L.; Silveira, C.M.; Elangovan, E.; Neto, J.P.; Nunes, D.; Pereira, L.; Martins, R.; Viegas, J.; Moura, J.J.G.; Todorovic, S.; et al. Synthesis of WO_3 Nanoparticles for Biosensing Applications. *Sens. Actuators B Chem.* **2016**, *223*, 186–194. [CrossRef]
248. Santhosh, M.V.; Devaky, K.S.; Jayaraj, M.K. Hydrothermal Synthesis of WO_3 Nanoparticles: Characterization and Sonocatalytic Study. *Mater. Today Proc.* **2020**, *25*, 183–185. [CrossRef]
249. Jeevitha, G.; Mangalaraj, D. Ammonia Sensing at Ambient Temperature Using Tungsten Oxide (WO_3) Nanoparticles. *Mater. Today Proc.* **2019**, *18*, 1602–1609. [CrossRef]
250. Wang, X.; Chen, F.; Yang, M.; Guo, L.; Xie, N.; Kou, X.; Song, Y.; Wang, Q.; Sun, Y.; Lu, G. Dispersed WO_3 Nanoparticles with Porous Nanostructure for Ultrafast Toluene Sensing. *Sens. Actuators B Chem.* **2019**, *289*, 195–206. [CrossRef]
251. Tong, H.; Xu, Y.; Cheng, X.; Zhang, X.; Gao, S.; Zhao, H.; Huo, L. One-Pot Solvothermal Synthesis of Hierarchical WO_3 Hollow Microspheres with Superior Lithium Ion Battery Anode Performance. *Electrochim. Acta* **2016**, *210*, 147–154. [CrossRef]
252. Jin, B.; Wang, J.; Xu, F.; Li, D.; Men, Y. Hierarchical Hollow WO_3 Microspheres with Tailored Surface Oxygen Vacancies for Boosting Photocatalytic Selective Conversion of Biomass-Derived Alcohols. *Appl. Surf. Sci.* **2021**, *547*, 149239. [CrossRef]
253. Wang, Y.; Yao, L.; Xu, L.; Wu, W.; Lin, W.; Zheng, C.; Feng, Y.; Gao, X. One-Step Solvothermal Synthesis of Hierarchical WO_3 Hollow Microspheres with Excellent NO Gas Sensing Properties. *Mater. Lett.* **2021**, *302*, 130460. [CrossRef]
254. Lv, Y.-K.; Yao, B.-H.; Liu, Z.-Q.; Liang, S.; Liu, Q.-C.; Zhai, K.; Li, Z.-J.; Yao, H.-C. Hierarchical Au-Loaded WO_3 Hollow Microspheres With High Sensitive and Selective Properties to Toluene and Xylene. *IEEE Sens. J.* **2019**, *19*, 5413–5420. [CrossRef]
255. Lee, C.-Y.; Kim, S.-J.; Hwang, I.-S.; Lee, J.-H. Glucose-Mediated Hydrothermal Synthesis and Gas Sensing Characteristics of WO_3 Hollow Microspheres. *Sens. Actuators B Chem.* **2009**, *142*, 236–242. [CrossRef]
256. Wang, H.-R.; Zhang, G.-Y.; Xu, Y.-Y.; Wei, X.-M.; Shen, X.-Q.; Sun, Y.-Q. Facile Ethanol/Water Solvothermal Synthesis of {001} Facet Oriented WO_3 Architectures with Superior Simulated Sunlight Photocatalytic Activities. *CrystEngComm* **2016**, *18*, 8089–8100. [CrossRef]
257. Wang, Z.; Hu, M.; Qin, Y. Solvothermal Synthesis of WO_3 Nanocrystals with Nanosheet and Nanorod Morphologies and the Gas-Sensing Properties. *Mater. Lett.* **2016**, *171*, 146–149. [CrossRef]
258. Lim, J.-C.; Jin, C.; Choi, M.S.; Kim, M.Y.; Kim, S.; Choi, S.-M.; Baek, S.-H.; Lee, K.H.; Kim, H.-S. Synthesis, Morphology, Characterisation, and Ethanol Gas Sensing of Hierarchical Flower-like Co-Doped WO_3 Nanoplates by Solvothermal Route. *Ceram. Int.* **2021**, *47*, 20956–20964. [CrossRef]
259. Wang, Q.; Huang, J.; Zhou, J.; Liu, Z.; Geng, Y.; Liang, Z.; Du, Y.; Tian, X. Different Nanostructured Tungsten Oxides Synthesized by Facile Solvothermal Route for Chlorine Gas Sensing. *Sens. Actuators B Chem.* **2018**, *275*, 306–311. [CrossRef]
260. Wang, X.; Han, W.; Yang, J.; Cheng, P.; Wang, Y.; Feng, C.; Wang, C.; Zhang, H.; Sun, Y.; Lu, G. Conductometric Ppb-Level Triethylamine Sensor Based on Macroporous WO_3-$W_{18}O_{49}$ Heterostructures Functionalized with Carbon Layers and PdO Nanoparticles. *Sens. Actuators B Chem.* **2022**, *361*, 131707. [CrossRef]

261. Baek, W.; Chang, H.; Bootharaju, M.S.; Kim, J.H.; Park, S.; Hyeon, T. Recent Advances and Prospects in Colloidal Nanomaterials. *JACS Au* **2021**, *1*, 1849–1859. [CrossRef]
262. Agrawal, A.; Cho, S.H.; Zandi, O.; Ghosh, S.; Johns, R.W.; Milliron, D.J. Localized Surface Plasmon Resonance in Semiconductor Nanocrystals. *Chem. Rev.* **2018**, *118*, 3121–3207. [CrossRef] [PubMed]
263. Jia, C.-J.; Schüth, F. Colloidal Metal Nanoparticles as a Component of Designed Catalyst. *Phys. Chem. Chem. Phys.* **2011**, *13*, 2457. [CrossRef] [PubMed]
264. Salim, E.T.; Saimon, J.A.; Muhsin, M.S.; Fakhri, M.A.; Amin, M.H.; Ibrahim, R.K.; Qaeed, M.A. Synthesis of WO_3 NPs by Pulsed Laser Ablation: Effect of Laser Wavelength. *J. Mater. Sci. Mater. Electron.* **2024**, *35*, 533. [CrossRef]
265. Fakhari, M.; Torkamany, M.J.; Mirnia, S.N.; Elahi, S.M. UV-Visible Light-Induced Antibacterial and Photocatalytic Activity of Half Harmonic Generator WO_3 Nanoparticles Synthesized by Pulsed Laser Ablation in Water. *Opt. Mater.* **2018**, *85*, 491–499. [CrossRef]
266. Salim, E.T.; Saimon, J.A.; Muhsin, M.S.; Fakhri, M.A.; Amin, M.H.; Azzahrani, A.S.; Ibrahim, R.K. Mesoporous Ag@WO_3 Core–Shell, an Investigation at Different Concentrated Environment Employing Laser Ablation in Liquid. *Sci. Rep.* **2024**, *14*, 5473. [CrossRef]
267. Kalhori, H.; Ranjbar, M.; Farrokhpour, H.; Salamati, H. Fabrication of Pd/WO_3 Colloidal Nanoparticles by Laser Ablation in Liquid of Tungsten for Optical Hydrogen Detection. *J. Laser Appl.* **2019**, *31*, 032018. [CrossRef]
268. Ghafouri, M.; Ghahramani Azad, A.; Bidadi, S.; Zeinalvand Farzin, B. Preparation of Redispersed WO_3 Nanoparticles in N-Methyl-2-Pyrrolidone by Ethylene Glycol as a Dispersing Agent. *Inorg. Nano-Met. Chem.* **2022**, 1–6. [CrossRef]
269. Han, B.; Popov, A.L.; Shekunova, T.O.; Kozlov, D.A.; Ivanova, O.S.; Rumyantsev, A.A.; Shcherbakov, A.B.; Popova, N.R.; Baranchikov, A.E.; Ivanov, V.K. Highly Crystalline WO_3 Nanoparticles Are Nontoxic to Stem Cells and Cancer Cells. *J. Nanomater.* **2019**, *2019*, 5384132. [CrossRef]
270. Yamazaki, S.; Isoyama, K. Kinetic Studies of WO_3 -Based Photochromism in Polyvinyl Alcohol Film. *Langmuir* **2023**, *39*, 10240–10248. [CrossRef]
271. Martinez Pancorbo, P.; Thummavichai, K.; Clark, L.; Tabish, T.A.; Mansfield, J.; Gardner, B.; Chang, H.; Stone, N.; Zhu, Y. Novel Au–SiO_2–WO_3 Core–Shell Composite Nanoparticles for Surface-Enhanced Raman Spectroscopy with Potential Application in Cancer Cell Imaging. *Adv. Funct. Mater.* **2019**, *29*, 1903549. [CrossRef]
272. Paik, T.; Cargnello, M.; Gordon, T.R.; Zhang, S.; Yun, H.; Lee, J.D.; Woo, H.Y.; Oh, S.J.; Kagan, C.R.; Fornasiero, P.; et al. Photocatalytic Hydrogen Evolution from Substoichiometric Colloidal WO_{3-x} Nanowires. *ACS Energy Lett.* **2018**, *3*, 1904–1910. [CrossRef]
273. Manthiram, K.; Alivisatos, A.P. Tunable Localized Surface Plasmon Resonances in Tungsten Oxide Nanocrystals. *J. Am. Chem. Soc.* **2012**, *134*, 3995–3998. [CrossRef] [PubMed]
274. Zavaleta, C.; Ho, D.; Chung, E.J. Theranostic Nanoparticles for Tracking and Monitoring Disease State. *SLAS Technol.* **2018**, *23*, 281–293. [CrossRef] [PubMed]
275. Gavrilović, T.V.; Jovanović, D.J.; Dramićanin, M.D. Synthesis of Multifunctional Inorganic Materials. In *Nanomaterials for Green Energy*; Elsevier: Amsterdam, The Netherlands, 2018; pp. 55–81.
276. De Coster, V.; Poelman, H.; Dendooven, J.; Detavernier, C.; Galvita, V.V. Designing Nanoparticles and Nanoalloys for Gas-Phase Catalysis with Controlled Surface Reactivity Using Colloidal Synthesis and Atomic Layer Deposition. *Molecules* **2020**, *25*, 3735. [CrossRef]